CR-164757

Department of Earth and Planetary Sciences

Massachusetts Institute of Technology

Cambridge, Massachusetts 02139

Final Report to: National Aeronautics and Space Administration Geodynamics Program - Global Earth Structure and Dynamics

Title: Geophysical Study of the Structure and Processes of the Continental Convergence Zones - Alpine-Himalayan Belt (NASA Grant NSG 5260)

Principal Investigator: M. Nafi Toksöz

Co-Investigator: Peter Molnar

Period: 1 April 1978 - 31 May 1979

Date: 1 September 1981

TABLE OF CONTENTS

ABSTRACT

This report describes the progress under NASA Cooperative Agreement NCC5-8 during the period from May 1, 1978 to April 30, 1979. The seismic wave velocity structure in the crust and upper mantle region beneath the Tibetan plateau was studied in detail. Also, a preliminary study of the uppermost mantle P wave velicity beneath Iran and Turkey was carried out, and the results are compared with those for the Tibetan plateau. These two studies compose the bulk of our efforts on the observational aspects of continental collision zones in addition to satellite derived data. On the theoretical aspects the thermal evolution of converging plate boundaries was explored using a finite difference scheme. A separate study examined the question of whether continental lithoshpere can be subducted into the asthenosphere by a large amount.

INTRODUCTION

A geophysical study of the structure and processes of the continental convergence zones with special references to the Alpine-Himalayan Belt is carried out under NASA Cooperative Agreement NCC5-8. This report presents the accomplishments made during the period of May 1, 1978 to April 30, 1979.

The bulk of this report consists of three published papers and one paper in press. The first two papers concentrate on obtaining reliable seismic data to complement satellite derived data. In the first paper, a combination of surface wave dispersion, P_L (a leaky mode) propagation, refraction profiles using earthquakes, and teleseismic P and S wave travel time residuals place constraints on the seismic wave velocity structures beneath the Tibetan plateau. The results confirm the idea of a very thick crust ($\sim$70 km) and reveal a shield-like uppermost mantle (with seismic velocities of 8.1 km/s for P wave and 4.8 km/s for S wave) overlying a low velocity mantle. The uppermost mantle P wave velocities beneath Turkey and Iran are investigated in the second paper. These velocities show large regional variations (7.7 km/s for Turkey and 8.0 km/s for Iran) - an indication of possible differences in tectonic processes. These velocity values were further used to estimate the relative temperature near the Moho between these regions and stable shields.

We also finished two theoretically oriented studies. The

evolution of the thermal structure beneath a subduction zone is modeled using numerical methods. This is a starting point of modeling collisional tectonics because, at least along the Alpine-Himalayan belt, subduction of oceanic lithospheres always proceded continental collision. Thus, the thermal regime of a subduction zone serves as the initial condition of the complicated thermal mechanical processes of a collision zone. The problem of whether the continental lithosphere, with its buoyant crust, can be subducted by a large amount into the asthenosphere is investigated in the last study presented in this report. The uncertainties are large so that one can not prove this is definitely not the case. However, the most favorable condition for subducting continental lithosphere would involve detachment of the continental crust from the rest of the lithosphere.

Reprints of the published papers and preprint of the paper in press follow this section. In the end of this report we also include abstracts of two studies presented at professional meetings during this period.

CONSTRAINTS ON THE SEISMIC WAVE VELOCITY STRUCTURE BENEATH THE TIBETAN PLATEAU AND THEIR TECTONIC IMPLICATIONS

Wang-Ping Chen and Peter Molnar
Department of Earth and Planetary Sciences
Massachusetts Institute of Technology
Cambridge, MA 02139

Abstract

We combine observations of group and phase velocity dispersion of Rayleigh waves, of the wave form of a long period P_L phase, of P_n and S_n velocities from unreversed refraction profiles using earthquakes, and of teleseismic S-P travel time residuals to place bounds on the seismic wave velocity structure of the crust and upper mantle under Tibet. From surface wave measurements alone, the Tibetan crustal thickness can be from 55 km to 85 km, with corresponding uppermost mantle shear wave velocities of about 4.4 km/s to 4.9 km/s, respectively. The P_n and S_n velocities were determined to be 8.12 ± 0.06 km/s and 4.8 ± 0.1 km/s respectively using travel time data at Lhasa from earthquakes in and on the margins of Tibet. With these estimates of the uppermost mantle velocity and with the surface wave dispersion, the crustal thickness is most likely to be between 65-80 km with an average shear wave velocity in the crust less than 3.5 km/s. A synthesis of one P_L wave form does not provide an additional constraint on the velocity structure but is compatible with the range of models given above. Measurements of both teleseismic S wave and P wave arrival times for nine earthquakes within Tibet show unusually large intervals between P and S compared with the Jeffreys-Bullen Tables. Yet both S wave and P wave arrival times from eight earthquakes in the

nearby Himalaya agree quite well with these Tables. Thus the P_n and S_n velocities apparently do not reflect high velocities in the mantle to a great depth beneath Tibet. From the dependence of the seismic velocities of olivine on pressure and temperature and from the similarity of the measured P_n and S_n velocities beneath Tibet and beneath shields and platforms, the temperature at the Moho beneath Tibet is compatible with being 250-300° higher than beneath shields and platforms, i.e. 750°C if the temperature beneath the platforms is close to 500°C. Such a temperature could reach or exceed the solidus of the lower crust. Simple one-dimensional heat conduction calculations suggest that the tectonic and volcanic activity could be explained by the recovery of the geotherm maintained by a mantle heat flux of about 0.9 HFU at the base of the crust. If the distribution of radioactive heat production elements were not concentrated at the top of the crust, radioactive heating could also contribute significantly to the recovery of the geotherm and thus lower the required mantle heat flow. Thus the idea of a thickened crust in response to horizontal shortening is compatible both with these data and with these calculations.

INTRODUCTION

With an average elevation of about 5 km above sea level over an area of 7×10^5 km^2, the Tibetan plateau is certainly one of the most conspicuous topographic features on earth. To the south and southwest, it is bounded by the Himalayan convergent zone, where the continental collision between India and Eurasia plates manifests itself predominantly by low angle thrust faulting [e.g. Fitch, 1970; Molnar et al., 1973, 1977]. The Altyn Tagh and the Kun Lun left-lateral strike-slip faults form its northern boundary [e.g. Molnar and Tapponnier, 1975; Tapponnier and Molnar, 1977]. In contrast, recent normal faulting [e.g. Molnar and Tapponnier, 1975, 1978; Ni and York, 1978] and volcanism are widespread over the plateau [Burke et al., 1974]. With its complex variations of active tectonic styles and its massive volume, the evolution of the Tibetan plateau has been recognized as a key to the understanding of continent-continent convergent processes [e.g. Dewey and Burke, 1973; Molnar and Tapponnier, 1975, 1978; Toksöz and Bird, 1977].

Primarily because of its inaccessibility, geological data available about Tibet are very limited. Upper Cretaceous limestones seem to cover much of southern Tibet [Hennig, 1915; Norin, 1946]. This observation places a lower bound on the time of uplift, but we are not aware of evidence that constrains the timing more tightly. Volcanism, which is

apparently quite young is widespread on the plateau [e.g. Burke, et al., 1974; Kidd, 1975]. Recently Deng [1978] reported Quaternary calc-alkaline to alkaline volcanics in northern Tibet at sites close to those of the earlier findings of Norin [1946]. Similar rock types have also been reported along the southern part of Tibet [Chang and Cheng, 1973; Hennig, 1915; Kidd, 1975].

Given the unusual elevation and the limited geologic data, the crustal and upper mantle structures should place important constraints on the geologic evolution of the plateau. Gravity data are too limited to provide a tight constraint. Amboldt [1948] reported one gravity measurement within the plateau that is consistent with isostatic equilibrium. Chang and Cheng [1973] also inferred isostatic equilibrium from more recent, but unpublished gravity data. As pointed out by Bird and Toksöz [1977] the crustal thickness of Tibet is likely to be from 55 to 70 km assuming isostatic compensation with mantle properties varying from a mid-ocean ridge-like conditions to stable shield-like environments. Given the uncertainties in the density of the crustal rocks, an even greater range is possible.

Almost all the previous seismic studies of Tibet are based on group velocity dispersion curves of surface waves [Bird, 1976; Bird and Toksöz, 1977; Chun and Yoshii, 1977;

Patton, 1978; Tung and Teng, 1974; Tseng and Sung, 1963]. In general, these investigators concluded that the crust is about 70 km thick with a relatively low upper mantle shear wave velocity (near 4.5 km/s). The mantle velocities, however, cannot be well constrained with surface wave data alone [Der et al., 1970]. The possible trade-off between upper mantle velocities and crustal thickness was not investigated in most of these studies, and little attention has been given to the uncertainties and bounds of allowable velocity structures. We do not consider the results in the published studies to be conclusive evidence for crustal thicknesses of 70 km, and consequently we have carried out a study of not only surface wave dispersion but also of other seismic phases.

Considering that the crust is thick now, but probably was not thick before the collision between India and Eurasia in the early Tertiary, there have been two extreme mechanisms proposed for the thickening of the crust and the uplift of the plateau. Dewey and Burke [1973], Toksöz and Bird [1977] and probably others suggested that Tibet formed by relatively uniform crustal shortening and thickening (like an accordion) in response to horizontal compression. Others [e.g., Argand, 1924; Powell and Conaghan, 1973, 1975] inferred that low angle underthrusting of one crustal block (India) beneath another (Tibet) is the dominant mechanism for creating the

high plateau. Both models require a decrease, if only temporary, in the crustal temperature gradient due to the crustal thickening. Therefore a more quantitative treatment of either situation is required to explain how volcanism could occur on the plateau.

The existence of the volcanoes and the inference of relatively low seismic wave velocities led logically to the suggestion that the upper mantle beneath Tibet is relatively hot and light. Part of the high elevation but not the crustal thickening could then be a consequence of thermal expansion of the underlying mantle. Although these various opinions diverge considerably and the specific physical processes are vaguely described at best, the ultimate cause of Tibet's elevation, thick crust and volcanism is virtually unanimously attributed to the India-Eurasia collision.

The existing data for Tibet are too scarce to discriminate among the various proposed evolutionary mechanisms, but tectonic models of the evolution of the India-Eurasia continental collision must provide satisfactory explanations for the structure of the plateau. Furthermore, studying the geophysical characteristics of the Tibetan plateau and the active Himalaya probably provides basic information that constrain the processes of large scale continental tectonics in general.

The purpose of this study is to present a comprehensive

seismological data set that places improved constraints on the seismic velocity structure of the crust and upper mantle beneath the Tibetan plateau. We discuss separately the four relatively independent seismic methods employed: surface wave dispersion for paths crossing the plateau, synthesis of a P_L phase crossing the plateau, P_n and S_n refraction profiles using earthquakes in Tibet and the Himalaya, and teleseismic S wave travel time residuals from earthquakes in and near Tibet. In each section describing the individual seismic phases, a brief introduction is given, followed by the results of observations. Constraints on possible models and discussions of them are then presented. At the end, we present an interpretation of all the observations and discuss their tectonic implications.

None of the studies of individual seismic phases requires a unique velocity structure, but a consistent model of the crustal thickness and uppermost mantle velocities can be obtained from the combined observations. In particular, the non-uniqueness of the velocity structure has been reduced considerably by the determination of the uppermost mantle velocities from refraction profiles.

SURFACE WAVE DISPERSION

a) Dispersion Curves

We analyzed long-period seismograms for nine earthquakes in and near Tibet recorded at one or more of the four stations of the World Wide Standardized Seismograph Network (WWSSN) just south of the Himalaya (Table I). More than 80% of each of the great circle paths is within the plateau. We chose not to use longer paths that cross much of Asia because of the difficulties in deciding how to regionalize them and because of the likelihood of marked lateral refraction at the boundaries of Tibet and elsewhere. We trust more the results obtained from paths confined as much as possible to Tibet. Thus, the range of epicentral distances is limited to about 20° (Fig. 1). The multi-filtering technique [Dziewonski et al., 1969] was used to obtain the group velocity dispersion curves. We analyzed only seismograms that have high signal-to-noise ratios and for which a minimum amount of multi-pathing was apparent (Fig. 2). For only two paths were clear long-period ($\geq$60 sec) Rayleigh waves recorded with large amplitudes (Fig. 2a). Unfortunately Rayleigh waves with periods near 30 sec were so large on these two records that it was impossible to study the dispersion curves for periods less than 60 sec.

We analyzed only fundamental modes of both Love and Rayleigh waves with periods from 10 to 90 sec. Group

velocity dispersion curves for Rayleigh waves differ from one another by about 3% (Fig. 3a), which is comparable with that in some previous studies [e.g., Chun and Yoshii, 1977]. The dispersion curves between 30s and 60s are poorly defined because of a low signal-to-noise ratio, which is apparent from visual inspection of the seismograms. The amplitudes on the seismograms are reduced, at least in part, because the group velocity dispersion curve is very steep in this particular frequency band, but Bird and Toksöz [1977] inferred an extremely high attenuation in this band as well. Since the uncertainty of this part of the dispersion curve is large, we consider that this part is essentially undetermined. Compared with the previous studies mentioned above [e.g., Chun and Yoshii, 1977; Bird and Toksöz, 1977] our long-period Rayleigh wave group velocities are about 2 to 3% faster at 70 to 80 sec but slower at longer periods by about the same amount. This difference contributes partly to the differences in preferred mantle velocity models. Love wave group velocities observed here also differ from one another by 5 to 10% (Fig. 3b). No clear Love wave with period longer than 70 sec was observed.

We also used phase velocities to aid in the discussion of these observations. Phase velocity dispersion curves (Fig. 4) are calculated using the standard single station method [e.g., Weidner and Aki, 1973].

A combination of a mislocation of 10 km and a 2 sec error in origin time can cause an error of 0.8% in determinations of both group and phase velocities at a distance of 20°. An uncertainty in the group arrival time or phase delay of one-eighth of the period at periods near 80 sec leads to an uncertainty of 1.6% in group or phase velocity at this distance. We assume a total combined maximum error of up to 3% in both is possible for the long period end of the dispersion curves. The uncertainty in the group velocity at short-periods should be less. However, lateral heterogeneity will have a much larger effect on relatively shorter wavelength components than on the longer wavelength components. This might be part of the reason why there is a fairly large scatter in the data at short periods.

For shallow events, the source depth is not important at long periods. Because both events I and II have nearly vertical strike-slip fault plane solutions, obtained primarily from P wave first-motion polarities, [Molnar et al., 1973; Tapponnier and Molnar, 1977] the uncertainty in the calculated phase delay is small. At extreme conditions, assuming an error of 0.2 cycles in various phase delays, an error of 3.4% in phase velocity is possible if all the errors conspired together for periods near 80 sec and a distance of 20%. The relatively large error in the phase delay assumed here takes into account the effect of a possible non-step-like source time function.

Note that the two Rayleigh wave seismograms with large signal-to-noise ratios at long periods (1-NDI and II-SHL) involve different paths (Fig. 1). The I-NDI path is almost entirely within Tibet except at the southwestern end where it crosses the Himalaya at a high angle. The II-SHL path crosses part of the Pamir before it enters Tibet and then meets the Himalaya at a low angle. The difference between the two observations at periods longer than 60 sec could be simply due to observational errors, but it might actually reflect real differences in average velocity structures for different paths.

b) Velocity Models

Resolving power of data and assumptions in models:

Before interpreting the data, we briefly review the resolution of surface wave observations on velocity structures. Assuming a laterally homogeneous earth structure, Der et al., [1970] investigated effects of observational errors on the resolving power of surface waves using synthetic data with periods and distances comparable to those used here.

They found that for similar period ranges the fundamental Rayleigh mode yields considerably better resolution of the upper mantle velocity than the fundamental Love mode. If observations are restricted to fundamental modes only, crustal models with no more than 3 layers are justified. With both fundamental mode Rayleigh and Love waves and their first higher modes, the shear-wave velocity (V_s) resolution

in the upper crust, lower crust, and uppermost mantle are about 0.05, 0.08, and 0.1 km/sec, respectively. In particular, the shear wave velocity resolution is only 0.1 km/sec for a layer 100 km thick centered at a depth of 125 km. Unless the period range of group velocity observations for Rayleigh and Love wave fundamental modes exceeds 80 sec, the upper mantle velocity resolution is poor. The above summary is appropriate for group velocities. Phase velocity observations provide somewhat less resolution than group velocity observations with the same observational errors.

Der et al. [1970] assumed standard deviations of group velocities of approximately 0.3% near 15 sec and 1.5% at 80 sec; these errors are probably smaller than ours. With reliable group velocity observations of fundamental Rayleigh and Love waves at limited frequency band and with fairly large scatter (Fig. 3), and phase velocity measurements of fundamental Rayleigh mode between 60 to 90 sec only (Fig. 4), we did not perform a formal inversion. Instead, we examined a range of plausible models; and then from a comparison with the observation, we assigned bounds to the range of possible structures.

In constructing these models, we further assumed that:

1. The velocity structure below 90 km for most models and density structure for all models are the same as Gutenberg's continental model [Dorman et al., 1960].

2. The ratio of P wave velocity to S wave velocity is fixed at 1.73 in the crust and 1.80 in the uppermost mantle.

3. The shear wave velocity of the top 3.75 km is fixed at 2.55 km/sec [Chen and Molnar, 1975]. We did not consider the period range 5 to 10 sec here.

4. No more than 3 layers in the crust, excluding the top sedimentary layer, are included and the mantle between the Moho and a depth of 90 km is assumed to be homogeneous.

Since the resolution of P wave velocities is very poor compared with the resolution of S wave velocities, we examined dependencies of the dispersion curves only on V_s in the mantle, the crustal thickness, and the shear wave velocity structure in the crust. Theoretical dispersion curves were compared primarily with Rayleigh wave group velocity observations, but for selected structures comparison was also made with Rayleigh wave phase velocity observations. Love wave group velocity observations served only as a loose constraint. As long as theoretical values fall within the scatter of these data, no further comparison with them was made. Surface wave dispersion at the short period range (<30 sec) does not constrain the crustal thickness or the upper mantle shear wave velocity much. Little attention will be paid to these short period range observations in the following discussion of these two subjects.

Crustal thickness and upper mantle S wave velocities.

Rayleigh wave dispersion curves for three different crustal thicknesses (55, 70, and 85 km) were calculated for a range of uppermost mantle shear wave velocities (β_m) from 4.4 to 4.9 km/s (Figs. 5-7). At long periods, higher values of β_m cause higher Rayleigh wave group velocities, and greater crustal thicknesses cause lower group velocities (Figs. 5-7). For a crustal thickness of 55 km, only the model with the lowest value of β_m (4.4 km/s, model F4) fits the upper curve of the Rayleigh wave group velocity observations (Fig. 5). A lower value of β_m would be required to fit the lower curve, and if the assumed thickness of the crust is less than 55 km, β_m must be lower than 4.4 km/s. For a 70 km thick crust (Fig. 6), however, the β_m seems to be constrained to be near 4.7 km/s (Model S7) or higher in order to be consistent with observed group velocity dispersion curves. Values of β_m as small as 4.4 km/s seem to be incompatible with a 70 km crust (Fig. 6). If we further increase the crustal thickness to 85 km (Fig. 7), the observations constrain β_m to be 4.8 km/s or even 4.9 km/s, (Fig. 7), but the fit between the observed and theoretical curves appears to us to be worse than for the previous cases of 55 km and 70 km thick crust. These results confirm Der et al.'s [1970] numerical experiments that show that surface wave dispersion alone is inadequate to constrain both the crustal thickness and the upper mantle shear wave velocity tightly.

Phase velocity dispersion curves for four velocity models are plotted with the two observed dispersion curves in Fig. 4. The curve for model F4 (55 km thick crust, β_m = 4.4 km/s) lies within the scatter of the observations. Both model S7 (70 km thick crust, β_m = 4.7) and model SE (70 km thick crust, β_m = 4.8, with the lowermost crustal velocity lower than that of model S7) fit the observed phase velocities for the I-NDI path well and were within the uncertainties of the observations for the II-SHL path. Model S4 (70 km thick crust, β_m = 4.4 km/s) does not fit the II-SHL observed phase velocities and is systematically lower than the data for I-NDI. It turns out that if $\beta_m \geq 4.8$ km/s, however, the phase velocity data cannot rule out a crustal thickness of 85 km.

Velocity structure of the crust: The crustal structure is constrained primarily by the shorter period portion of the dispersion curves. This portion of the dispersion curve depends primarily on the mean shear wave velocity in the crust and on its gradient. Fig. 8 shows the theoretical Rayleigh wave group velocity dispersion curves for 7 different models with a fixed crustal thickness of 55 km and β_m = 4.4 km/s. If the acceptable values of the calculated Rayleigh wave group velocities are those that lie within the scatter of our data, then for such a crustal thickness, an average crustal shear wave velocity ($\bar{\beta}$) of

3.5 km/s seems to be too high (Fig. 8a). A single layer between the top low velocity surface layer and the Moho clearly will not fit the data unless $\bar{\beta}$ is much less than 3.5 km/s (Fig. 8b). By adding a higher velocity layer at the base of the crust so as to cause a velocity gradient in the crust and maintaining a constant $\bar{\beta}$, dispersion curves can be constructed that agree well with the data (Fig. 8b). To obtain such a fit, however, requires a relatively low velocity upper crust so that $\bar{\beta}_m$ is still less than 3.5 km/s.

Calculated Rayleigh wave group velocity dispersion curves for 5 different crustal structures with a 70 km thick crust and β_m = 4.7 km/s, also are consistent with $\bar{\beta}$ being less than 3.5 km/s (Fig. 9). The long-period end of the dispersion curve however, is sensitive to the shear wave velocity in the lower crust. For instance, the addition of a relatively high velocity layer (such as V_s = 3.9 km/s) between 60 and 70 km depth has the same effect on the long period portion of the dispersion curve that an increase of β_m (such as from 4.7 to 4.8 km/sec) below 70 km has (Fig. 9b,c). These variations are, of course, only examples of many other possibilities. Thus there are trade-offs between the lower crustal shear wave velocity and β_m which is in turn coupled with the crustal thickness.

For a crustal thickness of 85 km, the constraints on the crustal structure placed by surface waves will be even looser than the previous discussions for 55 and 70 km thick crust cases. We did not investigate any detailed models for this crustal thickness.

The most important constraint that surface wave dispersion places on the crustal structure is that the average crustal shear wave velocity is low. Clearly for the upper 40-50 km, $\bar{\beta} < 3.5$ km/s. Since the data seem to be better fit by a series of layers of increasing velocity than by a single layer of uniform velocity in the crust below sediments, the lower crust could have a shear wave velocity greater than 3.5 km/s, but it appears that even with this increase, $\bar{\beta}$ is less than 3.5 km/s for the entire crust. Our data do not require a low velocity zone in the crust [cf. Chun and Yoshii, 1977]. The crustal thickness and uppermost mantle shear wave velocity combinations obtained earlier are not very sensitive to the possible variations in the crustal structure.

c) Synthesis of Rayleigh wave signals

The group and phase velocity dispersion curves contain very little information about the amplitude of the surface waves other than the fact that there must exist a substantial amount of Fourier amplitude (spectral density) at a particular frequency in order to obtain a reliable determination of the group arrival time. As a further check on the velocity

structure, we have used the summation of normal modes to generate synthetic seismograms of vertical components of Rayleigh waves to investigate the possibility of detecting structural differences from these synthetic seismograms. The generation of synthetic seismograms requires a knowledge of the source depth, the fault plane solution, the source time function, the seismic moment, and parameters describing attenuation and a velocity structure. Usually, one assumes a knowledge of several of the factors and tries to deduce the others from the agreement of the synthetic seismogram with the observed one. The method was originally designed by Kanamori [1970] to investigate the long-period source characteristics of earthquakes at large distances.

We summed fundamental Rayleigh modes with periods between about 20 to 120s and generated synthetic seismograms for I-NDI and II-SHL observations (Fig. 1 and 2). Both the synthetic seismograms and the observed seismograms (paths I-NDI and II-SHL, Fig. 2) were low-pass filtered with a cut-off frequency at 0.04 Hz (25 sec) to eliminate excess high frequency oscillations that are superimposed on the long period signals of interest. The finite filter length tends to introduce different effects on the ends of the synthetic seismograms from those of the observations and is a shortcoming for relatively short distances as in our cases. The abrupt

beginnings of the synthetic seismograms results from truncating the earlier part of the time series which is not of interest here. The following discussion deals with simple experiments of the effects of the different parameters on the time domain observations.

Fault plane solutions for both events are held fixed and the uncertainties associated with them have small effects on the calculated wave form. A point source time history is assumed to be a step for simplicity. The severe attenuation for this region, proposed by Bird and Toksöz [1977] was applied to generate the theoretical seismogram marked with 'low Q' in Fig. 10a. The one marked 'normal Q' was generated with the observed attenuation for Rayleigh waves in an average earth structure [summarized in Kovach, 1978]. Although the amplitude for the 'normal Q' synthetic seismogram is 35% larger than that of the 'low Q' synthetic seismogram, the wave forms are quite similar in the bandwidth of interest here, 60 to 90 sec (Fig. 10a). For both synthetic seismograms the same velocity model S7 (70 km thick crust, β_m = 4.7 km/s, Fig. 6) and a source depth of 5 km were used.

Although the observed wave form of the II-SHL path is also shown in Fig. 10a, the purpose of this figure is to illustrate the effects of a very low Q. Part of the mismatch between the synthetic and observed signals arises from the end effects due to a finite filter length. The coda of the S wave

and the 20 sec period Rayleigh wave are the most noticeable sources of noise (Fig. 2a). The calculated Rayleigh waves are delayed in time with respect to the observed ones in Fig. 10a. The maximum mismatch in group arrival time corresponds to 2.7% difference in group velocity, which agrees with the dispersion curves in Fig. 6 and is within the observational errors.

Fig. 10b shows three synthetic seismograms, with their peak-to-peak maximum amplitude normalized to a common size, assuming model S7 with different source depths of 5, 10 and 30 km (the actual amplitude ratio is about 3:2:1 respectively). The difference in wave forms for sources at 5 km and 10 km is small. There is a slight difference in wave form for a source at 30 km depth. This can be attributed to the interference of the short period (<40 s) Rayleigh waves, which have a phase shift of π with respect to the longer periods and much weaker amplitudes than for a depth of 10 km [Tsai and Aki, 1970].

Synthetic seismograms were generated for three different velocity models: β_m = 4.4 km/s and 4.7 km/s for a crustal thickness of 70 km (S4 and S7) and β_m = 4.7 km/s for a crustal thickness of 55 km (F7) (Fig. 10c). A 5 km source depth and 'average-earth' Q structure were used. With a constant β_m (4.7 km/s), models with 55 km and 70 km thick crusts

(model F7 and S7) gave quite different synthetic seismograms (Fig. 10c). We consider Model F7 to be inadequate to explain the observation but that Model S7 is satisfactory in matching the observed wave form of the I-NDI path (Fig. 10c).

d) Summary of surface wave results

1. From group velocity dispersion curves in the period range of 10 to 30 sec, the average shear wave velocity in the upper crust is lower than 3.5 km/s.

2. From observed and calculated Rayleigh wave group and phase velocity dispersion curves and from synthesized Rayleigh waves with periods between about 60 to 90 sec, the uppermost mantle shear velocity cannot be constrained well even with an assumed crustal thickness. If we assume a β_m of 4.4 km/s, the crustal thickness is probably no more than 55 km. If β_m is about 4.7 km/s, the crustal thickness is likely to be greater than 65 km. A crustal thickness of 85 km is not impossible if β_m = 4.8 km/s and would be required if β_m were yet larger.

P_L PHASE SYNTHESIS

We observed one very clear P_L phase that crossed Tibet (Fig. 2a). P_L propagates as a leaky mode in the crust and travels with velocity higher than the shear wave velocity of the underlying mantle [Gilbert, 1964; Oliver and Major, 1961]. The P_L wave train arrives between the P and S phases and is normally dispersed. P_L can be viewed as the result of

multiple reflected and refracted P and SV waves, each of which is, at least once, an SV wave along the ray path [Helmberger, 1972].

Despite the energy leakage, the form of the P_L wave train can be used to infer the crustal structure. Both the phase and group velocity dispersion curves are fairly steep and the P_L wave train is generally short. This makes accurate measurements of dispersion difficult [e.g., Roupinet, 1972]. Instead, we have synthesized seismograms of P_L using different velocity structures in order to constrain the structure. Helmberger [1972] generated synthetic seismograms for P_L at distances between 4° to 13° from explosions using generalized ray theory, which employs a Cagniard-DeHoop algorithm. He assumed a layer over half-space. We followed his approach and used a double-couple earthquake source [Langston and Helmberger, 1975].

We calculated synthetic seismograms by summing generalized rays of up to suite order number 7 (7 segments in a ray) with a double-couple source at 5 km depth. The fault plane solution is the same as that used in the surface wave calculations before. No attenuation operator is applied to the synthetic seismograms. When we applied Futterman's [1962] constant Q operator with $t/Q \sim 1$ sec (where t is the travel time) the difference in the waveforms

was barely discernible. (This corresponds to an average $Q \sim 300$ for our case). The assumed far-field source time history is given by t exp[-t/10 (sec)], which would correspond to a fault length of about 30 km in Brune's [1970] formulation.

At first, synthetic seismograms were generated for models with a layer over half-space, each of which represented an average of the velocities in models obtained from surface wave dispersion. Figures 11a and 11b show the synthetic seismograms for two models with 70 km and 85 km thick crusts respectively, together with the observed signal. The first large peak in the synthetic seismograms results from S to P and P to S reflections off the Moho. The large amplitudes at the beginning of the observed seismogram are the direct, P, pP and sP, which penetrated into the upper mantle to 400-600 km and were not synthesized here. Numerical experiments showed that variations in the mantle velocities between 8.2 to 8.5 km/s have a negligible effect on the large amplitude pulse in the synthetic seismograms. Note that two quite different models (with a difference of 15 km in crustal thickness) gave similar wave forms in the synthetic seismograms (Fig. 11b). Moreover the maximum difference in group velocity between the two synthetic seismograms is only about 2%. This suggests poor resolution of velocity structures with P_L observations alone.

Next, we examined a series of multi-layered models similar to those based on surface wave dispersion in the last section. Helmberger [1972] concluded that for a layer over half-space, the source depth is not crucial, as long as the source is in that layer. Also an additional top low velocity layer has a small effect on the long period character of the synthetic seismograms. From a series of numerical experiments with model SE (Fig. 9b) we found that the effect of source depth and that of a low velocity layer are insignificant as long as the source is in the layer next to the low velocity surface layer. We tried several models derived from the surface wave dispersion curves that included crustal reflectors. Only rays reflected between the free surface and the interfaces including and above the Moho were used. Fig. 11c shows one example of such a synthesis. This particular model SEM1 has the same shear wave velocity structure as model SE (Fig. 9b), except the upper crustal layer has a P wave velocity 7% less than that of model SE. The large Moho reflections seen in Fig. 11b are suppressed. In addition, the late large arrivals, which resulted from the mid-crustal reflector, have a significant effect on the long-period wave form (compare Figs. 11c and 11b). The synthetic seismogram from this three-layered crustal model fits the long period characteristics of the P_L observation much better than the single layered crust cases. Other models were tested and

both velocities and layer thicknesses were modified in a trial and error process. No significant improvement was found with models of different crustal thicknesses and structures from that of model SE, and with a modified model S7 with a linear crustal-mantle transition. The model 'TP-2', with a low velocity zone in the crust preferred by Chun and Yoshii [1977], does not provide a better fit either, even after some variations in its crustal and mantle structures. Presumably, with more layers in the velocity models we might achieve a better match to the observed P_L signal. Yet considering the poor resolving power on the structure, further tiral seems fruitless. It is likely that the gross form of P_L can be matched with crustal thickness of 55 to 85 km if there is a velocity gradient in the crust, but that the observations do not constrain the structure very much.

REFRACTION PROFILES

It is well-known in classical seismology that the P_n and S_n velocities can be estimated from the travel time vs. distance plot using close earthquakes [e.g. Bullen, 1963, p. 194]. This involves using many stations for each event. Although, to our knowledge, Lhasa (LHA), has been the only permanent seismograph station in Tibet, the usual method can be modified using travel times from many earthquakes at a single station.

In practice, different earthquakes are reported with different focal depths. Moreover, the focal depths can easily be in error causing a corresponding error in the origin time. In either case, it is necessary to normalize the focal depth to a common depth in order to avoid introducing artificially large residuals due to different focal depths and therefore different path lengths. This can be done by adjusting the origin time with a depth correction calculated from equation (3) in Bullen [1963, p. 194], assuming an approximate velocity structure. The difference between the assumed and actual origin time is assumed to be absorbed by this depth correction completely. Any incomplete trade-off between the focal depth and the origin time, together with a small error induced by an error in the assumed velocity structure will cause a possible systematic error in the measured travel time. Because this error is presumably independent of distance in the normalized travel times, it should introduce only random errors in the evaluation of the velocity and therefore only affect the variance associated with the velocity determination, not the estimate of the velocity.

P_n and S_n arrival times were taken from the Lhasa station reports available between 1960 and 1965 and again between 1971 and 1973 [Institute of Geophysics, 1966, 1974].

We selected well-located events, for which more than 35 readings from teleseismic stations were used in the location. We used the epicenters, origin times, and depths given in the Bulletins of the International Seismological Summary (ISS) and the International Seismological Center (ISC).

P_n across Tibet: All 61 reported P_n arrival times between 3° to 17° from Lhasa are plotted in Fig. 12. A model with a crustal layer with P wave velocity (V_p) of 6.1 km/s over a half-space with v_p = 8.0 km/s was assumed to normalize the focal depth to 33 km, which is near the mean reported depth. For all cases, we took the radius of the interface to be 6306.2 km. For a Moho at 35 km depth, instead of 70 km, the estimated velocity should be increased by 0.5%. The P_n velocity is determined to be 8.15 $\pm$ 0.04 km/s, compared with 8.27 $\pm$ 0.07 km/s if no focal depth correction is applied (Table II). If the apparent velocity were in fact 7.9 km/sec, then the data should be more nearly parallel to the dashed line in Fig. 12. Such a low P_n velocity will not fit the data well unless there is some special distance dependent systematic error in locations, depths or origin times. If we limit ourselves to sharp P_n arrivals (excluding those reported as eP or eP_n in the station reports), we obtain a P_n velocity of 8.20 $\pm$ 0.04 km/s from 42 arrivals. Without the focal depth correction, we obtain 8.24 $\pm$ 0.09 km/s (Table II).

If we consider only the 39 sharp arrivals between 3° to 10° (Fig. 13), the P_n velocity is estimated to be 8.12 ± 0.06 km/s for the depth corrected case (Fig. 13b). This is the only case in all the profiles discussed in this section for which the P_n velocity determined without a depth correction, 8.0 ± 0.1 km/s (Fig. 13a) is the smaller. A total of 19 emergent arrivals between 3° to 17° gave an estimate of the velocity of 8.18 ± 0.13 km/s. Thus the entire data set is very consistent (Table II).

P_n across the Himalaya: The data discussed above includes only events north of the Indus Tsang-Po suture because of the possibility of a different structure beneath the Himalaya. However, recordings at Lhasa for 24 events south of the suture, for nearly all of which sharp readings were reported, yields a P_n velocity of 8.11 ± 0.07 km/s. The epicentral distances range from 3° to 17°. Among these, 21 events occurred within 10° of Lhasa (Fig. 14). Despite the scatter, the same estimate for P_n velocity is obtained. Thus no significant difference in the P_n velocity is observed for regions north and south of the suture zone.

S_n across the Tibet and the Himalaya: There are also 23 sharp S_n arrivals reported at Lhasa from events north of the suture in the distance range 3° to 10°. (Only three such arrivals were reported for distances greater than 10°). After the depth normalization, the S_n velocity is estimated to be 4.8 ± 0.1 km/s

(Fig. 15). There is a much larger scatter in the S_n residuals than the P_n residuals probably because of the slower S_n velocity and because of difficulties in identifying the arrival on the seismograms. A low S_n velocity of 4.5 km/s would not fit the data well (Fig. 15). The 11 sharp arrivals for events south of the suture, reported at Lhasa within 3° to 10° gave the same S_n velocity (Table II).

Intercept times and crustal thicknesses: Despite the large uncertainties, the intercept times for P_n all suggest the depth of the interface (the Moho) to be 65 $\pm$ 30 km. S_n intercept times have even larger uncertainties, but the depth of the interface calculated from them fall within the range (Table II) of 80 $\pm$ 50 km. The epicenters of all the events used in this refraction study show a broad azimuthal coverage and distribution of epicentral distances with respect to Lhasa (Fig. 16). Nevertheless, because purely reversed profile cannot be made, it is remotely conceivable that a dipping Moho or a systematic horizontal variation in the velocity structure centered around Lhasa might render the real mantle velocities different from the measured apparent velocity. For models with a crustal layer with v_p ranging from 5.9 to 6.5 km/s overlying a mantle half-space with v_p ranging from 7.9 to 8.4 km/s, a uniform dip of about 0.8° of the Moho could add an uncertainty of $\pm$0.1 km/s to the estimated P_n velocity. Such a dip would correspond to a difference in crustal

thicknesses of 15 km over 10° distance. Therefore, if Lhasa were to overlie a maximum depth to the Moho beneath Tibet, such that the crustal thickness decreased by 15 km, 10° to both the north and west, then the P_n velocity could be overestimated by 0.1 km/s. We think that because the average elevation of Tibet is so uniform, a drastic variation in crustal thickness is unlikely, and it would be fortuitous if Lhasa were to overlie the deepest crust or the center of a systematic horizontal variation of the velocity structure.

Summary of refraction results: High values of the P_n and S_n velocity beneath Tibet are obtained from refraction profiles using earthquakes in Tibet and arrival times at Lhasa. Assuming a Moho at 70 km depth, the P_n velocity is estimated to be 8.12 km/s with a minimum formal standard deviation of 0.06 km/s covering the region north of the suture from 3° to 10° from Lhasa. No significant difference in P_n velocity was found for the regions north and south of the suture. With a somewhat larger uncertainty, the velocity of S_n is similarly determined to be 4.8 $\pm$ 0.1 km/s. Both P_n and S_n velocities are about the same as those of the shields and stable platforms. All the intercept times have large uncertainties and they indicate a depth of the Moho of 65 $\pm$ 30 km.

TELESEISMIC S-P TRAVEL TIME RESIDUALS

To our knowledge, the high velocities for the uppermost mantle under Tibet discussed in the last section have not been proposed before. The vertical extent of the high velocity zone is of great importance in the interpretation of the tectonics. The refraction profiles require a layer beneath the Moho with a thickness of only about 10 km. P_L is relatively insensitive to mantle properties [Poupinet, 1972] and the surface wave dispersion curves are not very sensitive to the velocity structure below about 100 km. The teleseismic travel time measurements discussed in this section are intended to serve as a crude estimate of the vertically averaged velocity structure to a greater depth ($\sim$300 km).

Teleseismic P and S wave arrival times were measured from the records of the WWSSN stations for 9 earthquakes in Tibet and 8 earthquakes in the Himalaya (Fig. 17, Table III). Arrival times were measured only for S wave signals that are clear on the long-period records (Fig. 18). Uncertainties are about one second. To avoid inclusion of converted phases (e.g., Sp), we tried to measure only the transverse components of the S waves. S-wave polarization angles were checked with known P wave fault plane solutions [Molnar and Tapponnier, 1978; Molnar et al., 1973, 1977; Ni and York, 1978]. We considered only the distance range between 30° and 80° to avoid triplication in the S wave travel time curve, and possible misidentification of SKS for S.

Both P and S wave travel time residuals, with respect to the Jeffreys-Bullen [1940] (J-B) travel time tables, were plotted as a function of epicentral distance using locations and origin times given by the ISC. Since the hypocenters and origin times reported by ISC were calculated primarily using the J-B P wave travel times, the P wave residuals were automatically minimized. Because late (or early) S waves are likely to be associated with late (or early) P waves, the S-P residuals measured here probably give lower bounds to the S wave residuals.

For 9 earthquakes in Tibet, P wave residuals scatter around the mean as expected from the hypocenter location procedure, whereas S wave travel times show large delays (Fig. 19). The S-P travel time residuals have correspondingly large delays (Table III, Figs. 19 and 21). Applying station corrections [Sengupta, 1975; Sengupta and Julian, 1976] to these data does not significantly reduce the scatter, but increases the S-P travel time residuals by about 1 sec (Table III, Figs. 19 and 21).

With the same procedure, we studied 8 earthquakes in the Himalaya (Fig. 20) and observed smaller S-P travel time residuals than for earthquakes in Tibet (Table III, Figs. 20 and 21). The rays from earthquakes in Tibet and the Himalaya to a given station more than 30° from the epicenters will have nearly identical paths except near the source region. Thus we infer that the large S-P travel time

delays for earthquakes in Tibet are due to the medium properties of the region beneath Tibet and not to systematic errors in the travel time tables or to the medium along the rest of the ray paths.

In general, there is a strong trade-off between the focal depth and the origin time for events located teleseismically. Erroneous depths could also, at least partially, be responsible for the large S-P travel time delays for earthquakes in Tibet, if these earthquakes actually occurred at a shallower depth than was obtained in the location procedure. The S-P travel time residuals were calculated for each event assuming three possible depths: their depths given by the ISC, 5 km, and 33 km (Fig. 21). To make an extreme comparison, assume all earthquakes in Tibet occurred at 5 km depth, but all earthquakes in the Himalaya occurred at 33 km depth. On the average, there is still a difference of approximately 2 sec between the S-P residuals from earthquakes in these two regions (Fig. 21, Table III).

Thus the average S-P travel times are late for events in Tibet not only with respect to the J-B tables which represent an averaged earth model but also with respect to those for events in the Himalaya. Because low P wave velocities probably cannot be detected through routine location procedures using the P wave arrival times alone, a delay of 1s in P wave travel times from the average earth

could easily exist. This would lead to another second in delay in the S wave travel time.

The measured S-P travel time residuals, rounded to the smaller nearest integer, are given in 1 sec intervals in Figure 17 together with the locations of the 17 earthquakes. For this figure, the focal depths for Tibetan events are normalized to 5 km and for Himalayan events, at 33 km. Although our data points certainly do not allow a meaningful contouring of these residuals in Tibet, the two earthquakes in the center of Tibet have especially large S-P travel time residuals (>5 sec), and the distribution of S-P travel time residuals in the Himalaya is relatively uniform. The immediate inference from the late S-P travel times in Tibet is that the relatively high P_n and S_n velocities obtained from the refraction profiles discussed in the last section are not likely to extend to a great depth beneath Tibet.

SEISMIC WAVE VELOCITY STRUCTURE

Observed group and phase velocity dispersion curves of Rayleigh waves provide constraints on crustal thickness and the uppermost mantle shear wave velocity. For possible thicknesses of 55 km to 70 km, or even 85 km, the corresponding uppermost mantle shear wave velocities of 4.4 km/s or less to 4.7 $\sim$ 4.8 km/s, or even as large as 4.9 km/s, are required respectively. We consider an S_n velocity of 4.9 km/sec to be unlikely and therefore conclude that the crust probably is not as thick as 85 km.

The paths for the observations of surface waves and the P_L phase all cross the Himalayas. This apparent lateral inhomogeneity introduces an additional uncertainty that is difficult to quantify. The two clear long-period Rayleigh wave signals studied here cross the Himalaya at very different angles (Fig. 1), and the 3% difference in the group velocities could be a consequence of lateral heterogeneity. Nonetheless, we cannot confidently attribute this difference solely to real structural differences because of the uncertainties in the group velocity determinations.

Since both the P_n and S_n velocities were estimated to be relatively high from the refraction profiles, P_n velocity 8.12 $\pm$ 0.06 km/s, S_n velocity 4.8 $\pm$ 0.1 km/s, the crustal thickness is apparently about 70 km. It is difficult to attach a formal uncertainty to this thickness, but from the comparison between the observed and theoretical dispersion curves, we estimate that the crustal thickness is between 65 km and 80 km (Figs. 5, 6, and 7). These models seem to be compatible with the P_L wave form, but it does not provide a strong constraint on the velocity structures by itself.

Travel time measurements for earthquakes in Tibet to stations at distances of 30° to 80° indicate late S waves and long delays between P and S. Since the Tibetan earthquakes have late S-P travel times compared with earthquakes in the Himalaya, the average velocity beneath Tibet must be lower

than that of the Himalaya. The relatively high velocity zone beneath the Moho of Tibet, estimated from the refraction profiles therefore probably is not thick.

The S-P travel time residuals can be used to estimate differences in average upper mantle velocities beneath Tibet and stable platforms or shields with some additional assumptions. Suppose all such differences were confined to the upper 240 km as inferred for shields and ocean basins [Dziewonski, 1971; Okal, 1977]. Also assume that the measured S-P travel time residuals are estimates of S wave travel time residuals. Let us compare the Tibetan models with model S2 of Dziewonski [1971] for the shield regions, but modified to include 70 km thick crust. As an extreme let us assume that the earthquakes in Tibet occurred at a depth of only 5 km. Then if one increases the velocities of model S2 (with a 70 km thick crust) by about 1% to correct for the effect of velocity dispersion due to attenuation [Hart et al., 1977], the vertical one way S wave travel time between the depths of 0 and 240 km for modified model S2 is 53.8 sec. This is about 1.1 sec faster than that for the Jeffreys-Bullen model. Therefore the observed average S-P travel time delay of 3.6 sec with respect to the J-B tables for earthquakes in Tibet corresponds to an average difference of 4.7 sec in S wave travel time from the modified model S2. Of this 4.7 sec, 2 sec can be attributed

to the effect of a thick crust. The resulting S wave travel time difference of 2.7 sec corresponds to a reduction of the shear wave velocity of 6% between 70 to 240 km from that of model S2. If we assume that models S7, SE (70 km thick crust, β_m = 4.7-4.8 km/s, Figs. 6 and 9) or F4 (55 km thick crust, β_m = 4.4 km/s, Fig. 5) were appropriate for Tibet in the depth range from 0 to 100 km instead of S2, then the average shear wave velocity beneath Tibet must still be about 4 to 5% lower than that of model S2 for shields between the depths of 100 km and 240 km. Insofar as Dziewonski's [1971] model S2 is appropriate for the shields, this would correspond to the average shear wave velocity of about 4.3 km/s between 100 and 240 km depth beneath Tibet. Because of S-P residuals are lower bounds to the S wave delays and because we assumed extreme for the depths of the events in Tibet, the average shear wave velocity beneath Tibet could be still lower.

The effect of velocity dispersion due to attenuation has been neglected in the above discussions of crustal thickness. It is difficult to estimate the contribution from such velocity dispersion without sufficient data on both attenuation and phase velocity [e.g., Lee and Solomon, 1978]. Qualitatively, if strong attenuation exists, the estimate of shear wave velocities deduced from surface waves should be increased by a small amount (~1%) above those considered here before comparing them with body wave

observations [Hart et al., 1977]. Thus there might be a small systematic overestimate of a few km of the crustal thickness, but this overestimate is probably much less than the uncertainty quoted above.

TECTONIC IMPLICATIONS

A. The Thick Crust

The apparently very thick crust (~70 km) beneath Tibet implies that the crust has been thickened approximately by a factor of 2 since the collision between India and Eurasia. This is consistent with the idea of horizontal compression and shortening [Dewey and Burke, 1973]. The hypothesis of underthrusting the Indian plate beneath the Eurasian plate can be argued as still possible if somehow either the crust of Tibet were detached from its underlying mantle while the Indian plate was subducted along the base of the crust or if the Indian crust plunged into the mantle and then migrated, probably as a melt, up to the base of Tibet's crust. In other words, continental crust of the order of 100 to 1000 km length would have been consumed and recycled back near the surface in a time span of about 40 m.y. The current seismic data cannot discriminate between these two extremes but the relatively low average velocity of the crust implies that the crust is relatively hot. If cold Indian lithosphere were thrust under Tibet, it would have to have been heated since then.

B. Uppermost Mantle Seismic Velocities

Both P_n and S_n velocities indicate a high velocity uppermost mantle under Tibet. The late S-P travel time residuals for earthquakes in Tibet indicate that these high velocities do not reflect the properties of the deeper part of the upper mantle. Although the interpretation of the travel time residuals are highly non-unique, this high velocity layer extending no deeper than about 100 km under Tibet is consistent with the observations.

Implications for the temperature in the mantle: The apparently high uppermost mantle velocities under Tibet are not directly comparable to those under the stable platforms and shields because the extremely thick crust in Tibet will create about 10 to 12 kb of additional lithostatic pressure at the base of the thickened Tibetan crust. Assuming that the pressure and temperature dependence of seismic wave velocities for olivine are representative of the mantle [e.g. Anderson et al., 1968; Birch, 1969], 10 kb of pressure causes an increase in V_p of about 0.1 km/s and a temperature increase of about 250°C causes a similar decrease. V_s has very similar pressure-temperature dependence to that of the V_p for most olivine group minerals. Exceptions are the forsterite samples measured by Anderson et al. [1968], which have been questioned by Birch [1969]. Thus, if the P_n and S_n

velocities were the same beneath stable platforms and Tibet and if the temperature and pressure dependencies of the seismic velocities were those appropriate for olivine, then the temperature of the Moho beneath Tibet would be about 250°C hotter than that of the platform. This estimate of relative temperature would have an uncertainty as large as 120°C, even if the resolution of the difference in P_n velocity for Tibet and shields were only $\pm$0.05 km/sec. Thus this suggested difference in temperature is only a crude estimate, not a precise measurement.

The temperature under platforms and shields are difficult to estimate. From heat flow measurements, Sclater et al. [1980] estimated a lower bound on the temperature for the Canadian shield to be less than 400°C at the base of the crust. On the other hand, if we take the measured reduced heat flow as an upper bound of the mantle heat flow for Eastern U.S. (0.80 $\pm$ 0.05 HFU, [Lachenbruch and Sass, 1976]) and the Indian shield (0.93 HFU, [Rao et al., 1976]), the mantle heat flow alone gives 470°C and 540°C at the base of the crust respectively, without considering the effect of radioactivity and assuming a crustal thickness of 35 km and thermal conductivity of 6×10^{-3} cal/cm°C-sec. Uncertainties in conductivity and heat flow measurements alone will probably add 20% uncertainties to those estimates. In any case, if the temperature at the base of the crust beneath platforms

and shields were about 500°C, then at the Moho beneath Tibet it could be about 750°C. Although the uncertainty in this number is very large, our point is that the high P_n and S_n velocities do not require an unusually cold upper mantle.

Implications for the strength of the mantle: At first glance, the relatively high P_n and S_n velocities are likely to be taken as evidence for a cold and therefore strong upper mantle. Because crustal shortening requires strong deformation of the underlying mantle, the inference of high strength might be taken as evidence contradictory to crustal shortening. In this section we contend that the current uppermost mantle is not very strong.

The temperature at the Moho strongly affects on the mechanical behavior of the lower crust and upper mantle. One can estimate the mechanical strength of the uppermost mantle beneath Tibet assuming that the flow laws for steady state creep of olivine are representative of the uppermost mantle rheology [Goetze and Evans, 1979; Kirby, 1977; Tapponnier and Francheteau, 1978]. For differential stress $(\sigma_1-\sigma_3)$ less than 2 kb, the flow law can be written in the form:

$$\dot{\varepsilon} = A(\sigma_1-\sigma_3)^n \exp(-Q/RT) \qquad (1)$$

where $\dot{\varepsilon}$ is the strain rate, A and n are constants, Q is the activation energy, R is the gas constant and T is the absolute temperature. For dislocation creep of olivine, Goetze [1978] reported n = 3, A = 70 (bar^{-3} sec^{-1}), and Q = 122 (kcal/mole). Note that the uncertainties in the estimate of activation energy and temperature will dominate the uncertainty of the estimate of the differential stress or strain rate. Assuming a strain rate corresponding to 100% strain for the past 40 m.y., since the collision, the calculated differential stress is 1.1 kb at 750°C or 430 bars at 800°C. If the temperature were as low as 700°C, the calculated differential stress would be larger than 2 kb. Post [1977] obtained a quite different olivine flow laws for Mt. Burnet dunite. Using his 'dry' flow low under the same assumptions, differential stress is estimated to be 3.7 kbars at 800°C while the 'wet' flow law requires only 30 bars of differential stress under these conditions. If Coble creep (syntectonic recrystallization), instead of dislocation creep, however, is the predominant deformation mechanism, the calculated differential stress is only 210 bars at 800°C and 430 bars at 700°C at the given strain rate [Goetze, 1978]. Thus the lower bound of the differential stress required to deform the uppermost mantle under Tibet at the given strain rate through steady state ductile flow of olivine is only about 0.4 kb. Although the estimate of temperature beneath Tibet is too uncertain to

prove that the uppermost mantle is not strong, the apparently high P_n and S_n velocities beneath Tibet do not require high mechanical strength for the uppermost mantle.

Implications on volcanism in Tibet: It is interesting to note that at temperatures of about 800°C and 20 kb pressure, incipient melting of crustal material (but not the uppermost mantle) is possible in the presence of a small amount of water. Fig. 22 shows solidi for some likely crustal and upper mantle materials based on data from experimental petrology [Lambert and Wyllie, 1970; Merrill et al., 1970; Merrill and Wyllie, 1975]. None of the data have error bars and therefore they can only be used qualitatively. Nevertheless, the solidus for water saturated peridotite is over 1000°C despite the pressure [Merrill et al., 1970]. With only 0.1 weight% of water, partial melting of gabbroic material is possible at 20-25 kb pressure and between 700 to 800°C [Lambert and Wyllie, 1970]. The solidus for peridotite with 0.1 weight% water at this pressure range is over 1250°C. Thus for Tibet, there could be a geotherm such that a partially molten crust overlies a subsolidus uppermost mantle. The inference of a high velocity mantle lid on the low velocity zone, then, is not incompatible with the widespread volcanism over Tibet unless the volcanic activity is predominantly of uppermost mantle origin or unless the lower crust of Tibet consists of only anhydrous minerals. The geochemical evidence gathered so far is not sufficient

to reach any conclusion on whether the lower crust of Tibet is hydrous or not. Simply based on the fact that no tholeiitic basalt has been reported [Hennig, 1915, Deng, 1978], it is believed that the volcanic activity involved mostly melting of crustal materials [e.g. Dewey and Burke, 1973]. However, the unusually low average crustal velocity for Tibet is also consistent with high temperatures and melting.

C. A Discussion of the Thermal Evolution of the Plateau

The presence of widespread volcanic activity and diffuse seismicity with prominent normal faulting in Tibet (Molnar and Tapponnier, 1978) all indicate that Tibet is tectonically active at present. Yet the geothermal gradient in the crust should have been decreased by crustal thickening. Thus the source of heat deserves some consideration. There are three apparent heat sources that contribute to Tibet's crustal geotherm: strain heating from the thickening of the crust, radioactive heat production in the crust and the mantle heat flux from below the crust.

Since the crust of Tibet seems to be twice as thick as normal continental crust, the average strain rate in the crust is likely to be of the order of 1/40 m.y. Assuming an averaged differential stress of 1 kb throughout Tibet, the stress heating rate per unit volume (stress x strain rate) is only about 8×10^{-7} erg/cm^3-sec or 0.2×10^{-13} cal/cm^3-sec (0.2 HGU). This is considerably smaller than the presumed

radioactive heat production rate of about 1 HGU for lower crustal materials [e.g. Tilling et al., 1970] and can be neglected.

We investigate the effects of the mantle heat flux and radioactive heating in the crust by considering the simple one-dimensional heat conduction problem with the following assumptions:

1. A constant mantle heat flux (Q_h) is held at the base of the crust.

2. The thickening of the crust is instantaneous and the original geotherm is stretched accordingly. This serves as the initial condition.

3. Tibet defines a heat flow province such that the empirical relationship

$$Q_s = Q_h + D\,A_o, \qquad (2)$$

between surface heat flow (Q_s) and surface heat production rate (A_o) is valid.

4. There has been no erosion. This assumption is justified by the facts that the Cretaceous limestone is still widespread in southern Tibet [Hennig, 1915, Norin, 1946], and that the present-day drainage system in Tibet is internal.

We separate the temperature T in the crust into the contributions from the mantle heat flux T_m and from radioactive heat production T_R. Three possible distributions of radioactive heat producing elements in the crust are considered separately: (a) a uniform distribution with depth, (b) an exponentially decaying distribution as a function of depth with the surface heat production rate unchanged by crustal thickening, i.e., with no migration of heat producing elements after crustal thickening, and (c) an exponentially decaying distribution with depth but with the thickness of the layer of the variable heat producing elements unchanged by crustal thickening (i.e., the migration of radioactive heat producing elements is much faster than heat conduction). The detailed derivations are given in Chen [1979]. We will only summarize the most important results here. Throughout this discussion, the crustal thickness is taken to be thickened by a factor of two to a value of 70 km. We also assumed that the thermal conductivity (k) = 6×10^{-3} cal/cm-°C-sec and the thermal diffusivity (κ) = 0.01 cm^2/sec., and we shall concentrate our discussions only on the temperature at the base of the crust where it will be highest in the crust.

First, consider only T_m with two starting temperatures (T_m°) 500°C and 600°C, corresponding to mantle heat flow (Q_h) of 0.86 cal/cm^2-sec (HFU) and 1.03 HFU, respectively, at steady state. T_m will reach 800°C in about 45 and 14 m.y., respectively.

The contribution from radioactive heat production strongly depends on the distribution of those elements, parameterized by the constant D, in equation (2). The steady state temperature due to radioactive heat production (T_R^{∞}) is approximately proportional to D^2. For an exponential distribution of radioactivity, D must be much smaller than the crustal thickness to satisfy equation (2) [Lachenbruch, 1970]. If the differentiation of the radioactive heat producing elements is much faster than heat conduction so that D does not change during crustal thickening, then T_R contributes little to the crustal geotherm. This occurs because in most models, and probably in the earth also, the source of heat is far from the base of the crust.

For cases (a) and (b), $T_R^{\infty} \tilde{\sim} 4T_R^{\circ}$ and after 40 m.y., $T_R \tilde{\sim} 2T_R^{\circ}$, where T_R° is the contribution to the initial geotherm due to radioactivity. For instance, at 70 km depth, for case a, with Q_h = 0.75 HFU, D = 25 km and $A(z) = A_o$ = 1 HGU (T° = 490°C), in 40 m.y. T = 801°C. The steady state final heat flow at the surface would be only 1.25 HFU for this case. Since heat flow measurements are not available for Tibet, these hypothetical values are only meaningful as plausibility arguments, and they should not be taken as fact. Nonetheless, the above calculations suggest that it is possible that the lower crust of Tibet could reach 700-800°C in 40 m.y., simply from the recovery of the geotherm provided that the

heat flux from the mantle is greater than about 0.9 HFU regardless of the heat production in the crust. The starting temperature at the base of the crust is crucial in determining whether the temperature in the lower crust reaches 700 to 800°C in 40 m.y. With a reasonably warm starting temperature of 490°C at the Moho, and if there is sufficient radiogenic heat production in the crust to produce about 0.5 HFU after the crustal thickening, then, for a mantle heat flux of only 0.75 HFU, the calculated temperature at the Moho could reach 801°C after 40 m.y. Thus radioactive heat production could be important for the recovery of crustal geotherm in 40 m.y., especially if radioactive heating also makes a significant contribution to the original geotherm [Bird et al., 1975]. Similar conclusions on the importance of ratioactive heating are reached by England [1979] for the thickened Archaean crust.

Crustal shortening beneath Tibet by horizontal shortening [Dewey and Burke, 1973] seems to be compatible with both the seismic observations and these thermal calculations. Yet the behavior of the lithosphere as a whole during the continental collision is not clear. In fact, the assumptions in these calculations are directly related to this question. If we assume that at 70 km depth the mantle heat flux is about 0.9 HFU and that the temperature at the Moho is about 800°C, then for a coefficient of thermal conductivity (k) of 7.5×10^{-3} cal/cm/sec°C in the mantle, the 1300°C isotherm

will be reached at about 112 km. If indeed the lithosphere were maintained at an approximately constant thickness by a heat flux of about 0.9 HFU at the base of the non-convecting layer, then the estimated temperature at the base of the Tibetan crust could be explained simply in terms of the recovery of the geotherm with little contribution by radioactivity. The volcanic activity, at least in part, could be explained by the depression of the lower crust to depths where the temperature is high enough for it to melt. No anomalous heat flow from the asthenosphere would be required.

Presumably small scale convection maintains an essentially constant heat flux at the base of the plate. Parsons and McKenzie [1978] describe this in terms of the stability of a thermal boundary layer above the viscous asthenosphere and with a thickness δ between two isotherms. If a critical Rayleigh number $Ra_c = \frac{g\alpha\Delta T\delta^3}{\kappa\nu}$ is exceeded, the boundary layer becomes unstable so that small scale convection occurs and provides convective heat transport. In Ra_c, g is the gravitational acceleration, α the coefficient of volumetric thermal expansion and ν is the kinematic viscosity. If the whole lithosphere with the thermal boundary layer were thickened by horizontal shortening, δ would increase and Ra_c would increase as δ^3. Therefore crustal shortening and thickening would be a very effective way of enhancing the instability of the boundary layer and causin small scale convection. Effectively there would be a detachment of the bottom of the thickening

lithosphere that might tend to keep the lithosphere from continuing to thicken while the crust does.

CONCLUSIONS

1. The crust beneath Tibet is about 65 to 80 km thick with an average shear wave velocity of less than 3.5 km/s from surface wave dispersion, refraction profiles and P_L-phase synthesis.

2. P_n and S_n velocities were estimated to be 8.12 ± 0.06 km/sec and 4.8 ± 0.1 km/sec respectively.

3. The averaged vertical shear wave velocity between 70 to 240 km depth is about 6% lower than that of the shield model S2 [Dziewonski, 1970] and this average velocity beneath Tibet is also lower than that below the Himalaya by about the same amount.

4. From the P_n and S_n velocities and the pressure-temperature dependence of the seismic velocities for olivine, the temperatures at the base of the Tibetan crust could be about 250°C hotter than that beneath shields or stable platforms. Since the temperature at the Moho beneath platforms is about 500°C, the base of the crust beneath Tibet could be near 750°-800°C.

5. At this temperature, and depending on the deformation mechanism, the uppermost mantle is likely to have a maximum mechanical strength of less than about 1 kb. This value decreases rapidly with depth in the uppermost mantle.

6. Partial melting of the lower crustal materials but not the uppermost mantle is likely with these estimated temperatures. The low crustal velocities are consistent with a hot or partially molten lower crust.

7. Simple one-dimensional heat conduction calculations suggest that no anomalous mantle heat source is needed to explain the volcanic and tectonic activity provided that a heat flux of about 0.75 to 0.9 HFU (depending on the amount and distribution of crustal heat production) is available from the asthenosphere and that the chickness of the lithosphere does not increase drastically during crustal shortening.

Acknowledgements

We are grateful to A. Dainty who did much work in implementing a double-couple source to the generalized ray program STPSYN-3 by D.V. Helmberger and R.A. Wiggins. M. Bouchon, A. Dziewonski, and H. Kanamori kindly made their programs available to us. J. Ni provided several fault plane solutions in Tibet prior to their publication. K. Anderson, T.A. Chou, W.Y. Chung, W. Ellsworth, H. Patton and G. Stewart helped us in computations. We also benefitted from discussions with K. Burke, P. England, B. Parsons, and P. Tapponnier.

This research was supported by the National Science Foundation Grant No. 77-23017 EAR and by NASA Grant No. NCC5-8 (NSG 5260).

References

Amboldt, N., Relative Schwekraftbestimmungen mit Pendeln in Zentralasien, Reports from the Scientific Expedition to the Northwestern Provinces of China under the Leadership of Dr. Sven Hedin, Publ. 30 (II), Geodesy 2, Tryckeri, Aktiebolaget Thule, Stockholm, 1948.

Anderson, O.L., E. Schreiber, R.C. Liebermann, and N. Soga, Some elastic constant data on minerals relevant to geophysics, Rev. Geophys., 6, 481-524, 1968.

Argand, E., La tectonique de l'Asie, 13th International Geological Congress, Brussels, 1922, Comptes rendu, I, Pt. 5, 171-372, 1924.

Birch, F., Density and composition of the upper mantle: First approximation as an olivine layer, in The Earth's Crust and Upper Mantle, P.J. Hart (ed.), Geophys. Monograph, 13, Amer. Geophys. Un., Washington, DC, 1969.

Bird, P., Thermal and mechanical evolution of continental convergence zones: Zagros and Himalayas, Ph.D. Thesis, M.I.T., Cambridge, Mass., 1976.

Bird, P., and M.N. Toksöz, Strong attenuation of Rayleigh waves in Tibet, Nature, 266, 161-163, 1977.

Bird, P., M.N. Toksöz, and N.H. Sleep, Thermal and mechanical models of continent-continent convergent zones, J. Geophys. Res., 80, 4405-4416, 1975.

Brune, J.N., Tectonic stress and the spectra of seismic shear waves from earthquakes, J. Geophys. Res., 75, 4997-5009, 1970.

Bullen, K.E., An Introduction to the Theory of Seismology, 3rd ed., Chapt. 12, Cambridge University Press, Cambridge, 1963.

Burke, K.C.A., J.F. Dewey, and W.S.F. Kidd, The Tibetan plateau, its significance for tectonics and petrology, Geol. Soc. Amer. Abstr. Programs, 6, 1027-1028, 1974.

Chang, Cheng-fa and Hsi-lan Cheng, Some tectonic features of the Mt. Jolmo Lungma area, southern Tibet, China, Sci. Sinica, 16, 257-265, 1973.

Chen, W.P., Seismic studies of central Asia: some characteristics of earthquake mechanism and seismic wave velocity structure beneath the Tibetan plateau, Ph.D. Thesis, M.I.T., Cambridge, Mass., 251 pp., 1979.

Chen, W.P. and P. Molnar, Short-period Rayleigh wave dispersion across the Tibetan plateau, Bull. Seism. Soc. Amer., 65, 1051-1057, 1975.

Chun, K.Y., and T. Yoshii, Crustal structure of the Tibetan plateau: a surface wave study by a moving window analysis, Bull. Seism. Soc. Amer., 67, 735-750, 1977.

Deng, Wanming, A preliminary study on the petrology and petrochemistry of the Quaternary volcanic rocks of northern Tibet autonomous region, Acta Geol. Sinica, 52, 148-162, 1978.

Der, Z., R. Massé, and M. Landisman, Effects of observational errors on the resolution of surface waves at intermediate distances, J. Geophys. Res., 75, 3399-3409, 1970.

Dewey, J.F., and K.C.A. Burke, Tibetan, Variscan, and Pre-Cambrian basement reactivation: Products of a continental collision, J. Geol., 81, 683-692, 1973.

Dorman, J., M. Ewing, and J. Oliver, Study of shear-velocity distribution in the upper mantle by mantle Rayleigh waves, Bull. Seis. Soc. Amer., 50, 87-115, 1960.

Dziewonski, A.M., Upper mantle models from 'pure path' dispersion data, J. Geophys. Res., 76, 2587-2601, 1971.

Dziewonski, A., S. Bloch, and M. Landisman, A technique for the analysis of transient seismic signals, Bull. Seism. Soc. Amer., 59, 427-444, 1969.

England, P.C., Continental geotherms during the Archaean, Nature, 277, 556-558, 1979.

Fitch, T.J., Earthquake mechanism in the Himalaya, Burmese, and Andaman regions and continental tectonics in central Asia, J. Geophys. Res., 75, 2699-2709, 1970.

Futterman, W.I., Dispersive body waves, J. Geophys. Res., 67, 5279-5291, 1962.

Gilbert, F., Propagation of transient leaking modes in a stratified elastic waveguide, Rev. Geophys., 2, 123-153, 1964.

Goetze, C., The mechanism of creep in olivine, Phil. Trans. Roy. Soc. Lond., 288, 99-119, 1978.

Goetze, C., and B. Evans, Stress and temperature in the bending lithosphere as constrained by experimental rock mechanics, Geophys. J. Roy. astr. Soc., 59, 463-478, 1979.

Hart, R.S., D.L. Anderson, and H. Kanamori, The effect of attenuation on gross earth models, J. Geophys. Res., 82, 1647-1654, 1977.

Helmberger, D.V., Long-period body-wave propagation from 4° to 13°, Bull. Seism. Soc. Amer., 62, 325-341, 1972.

Hennig, A., Zur Petrographie und Geologie von Sudwestibet, in Southern Tibet, Vol. V., Kung, Boktryekeriet, P.A. Norstedt, Stockholm, 1915.

Institute of Geophysics, Preliminary Seismological Report of Central Station Peking and Auxiliary Stations, (1960-1965), (in Chinese), Academia Sinica, Peking, 1966.

Institute of Geophysics, Chinese Seismological Station Reports (1971-1973), (in Chinese), Academia Sinica, Peking, 1974.

Jeffreys, H., and K.E. Bullen, Seismological Tables, Brit. Assoc. Advancement of Sci., Gray-Milne Trust, London, 65 pp., 1940.

Kanamori, H., Synthesis of long-period surface waves and its application to earthquake source studies - Kurile Islands earthquake of October 13, 1963, J. Geophys. Res., 75, 5011-5027, 1970.

Kidd, W.S.F., Widespread late Neogene and Quaternary alkaline volcanism on the Tibetan plateau (abstract), EOS Trans., AGU, 56, 453, 1975.

Kirby, S.H., State of stress in the lithosphere: inferences from the flow laws of olivine, Pure Applied Geophys., 115, 245-258, 1977.

Kovach, R.L., Seismic surface waves and crustal and upper mantle structure, Rev. Geophys. Space Phys., 16, 1-13, 1978.

Lachenbruch, A.H., Crustal temperature and heat production: implications of the linear heat flow relation, J. Geophys. Res., 75, 3291-3300, 1970.

Lachenbruch, A.H. and J.H. Sass, Heat flow in the United States and the thermal regime of the crust, in: The Earth's Crust, J.G. Heacock (ed.), Geophys. Monograph, 20, Amer. Geophys. Un., Washington, DC, 1976.

Lambert, I.B., and P.J. Wyllie, Low-velocity zone of the earth's mantle: incipient melting caused by water, Science, 169, 764-766, 1970.

Langston, C.A., and D.V. Helmberger, A procedure for modeling shallow dislocation sources, Geophys. J. Roy. astr. Soc., 42, 117-130, 1975.

Lee, W.B., and S.C. Solomon, Simultaneous inversion of surface wave phase velocity and attenuation: Love waves in western North America, J. Geophys. Res., 83, 3389-3400, 1978.

Merrill, R.B., J.K. Robertson, and P.J. Wyllie, Melting reactions in the system $NaAlSi_3O_8$ - $KAlSi_3O_8$-SiO_2-H_2O to 20 kilobars compared with results for other feldspar-quartz-H_2O and rock - H_2O systems, J. Geol., 78, 558-569, 1970.

Merrill, R.B., and P.J. Wyllie, Kaersutite and kaersutite eclogite from Kakanui, New Zealand - Water excess and water-deficient melting to 30 kilobars, Geol. Soc. Amer. Bull., 86, 555-570, 1975.

Molnar, P., W.P. Chen, T.J. Fitch, P. Tapponnier, W.E.K. Warsi, and F.T. Wu, Structure and tectonics of the Himalaya: A brief summary of relevant geophysical observation, in Himalaya: Sciences de la Terre, pp. 269-294, Centre National de la Recherche Scientifique, Paris, 1977.

Molnar, P., T.J. Fitch, and F.T. Wu, Fault plane solutions of shallow earthquakes and contemporary tectonics in Asia, Earth Planet. Sci. Lett., 16, 101-112, 1973.

Molnar, P., and P. Tapponnier, Cenozoic tectonics of Asia: effects of a continental collision, Science, 189, 419-426, 1975.

Molnar, P., and P. Tapponnier, Active tectonics of Tibet, J. Geophys. Res., 83, 5361-5375, 1978.

Ni, J., and J.E. York, Late Cenozoic extensional tectonics of the Tibetan Plateau, J. Geophys. Res., 83, 5377-5387, 1978.

Norin, E., Geological explorations in Western Tibet, Reports from the Scientific Expedition to the Northwestern Provinces of China under the leadership of Dr. Sven Hedin, Publ. 29, (III), Geology 7, Tryckeri Aktiebolaget, Thule, Stockholm, 1946.

Okal, E.A., The effect of intrinsic oceanic upper-mantle heterogeneity on regionalization of long-period Rayleigh wave phase velocities, Geophys. J. Roy. astr. Soc., 49, 357-370, 1977.

Oliver, J., and M. Major, Leaking mode and the P_L phase, Bull. Seism. Soc. Am., 50, 165-180, 1960.

Parsons, B., and D. McKenzie, Mantle convection and the thermal structure of the plates, J. Geophys. Res., 83, 4485-4496, 1978.

Patton, H.J., Source and propagation effects of Rayleigh waves from central Asian earthquakes, Ph.D. Thesis, M.I.T., Cambridge, Mass., 1978.

Post, R.L., Jr., High-temperature creep of Mt. Burnet dunite, Tectonophysics, 42, 75-110, 1977.

Poupinet, G., P_L waves and crustal structure in Canada, Canad. J. Earth Sci., 9, 1014-1029, 1972.

Powell, C.M., and P.J. Conaghan, Plate tectonics and the Himalayas, Earth Planet. Sci. Lett., 20, 1-12, 1973.

Powell, C.M., and P.J. Conaghan, Tectonic models of the Tibetan Plateau, Geology, 3, 727-731, 1975.

Rao, R.U.M., G.V. Rao, and H. Narain, Radioactive heat generation and heat flow in the Indian Shield, Earth Planet. Sci. Lett., 30, 57-64, 1976.

Sclater, J.G., C. Jaupart, and D. Galson, The heat flow through oceans and continents, Rev. Geophys. Space Phys., (in press), 1980.

Sengupta, M.K., The structure of the earth's mantle from body-wave observations, Sc.D., Thesis, M.I.T., Cambridge, Mass., 1975.

Sengupta, M.K., and B.R. Julian, P-wave travel times from deep earthquakes, Bull. Seism. Soc. Amer., 66, 1555-1579, 1976.

Tapponnier, P., and J. Francheteau, Necking of the lithosphere and the mechanics of slowly accreting plate boundaries, J. Geophys. Res., 83, 3955-3970, 1978.

Tapponnier, P. and P. Molnar, Active faulting and tectonics in China, J. Geophys. Res., 82, 2905-2930, 1977.

Tilling, R.I., D. Gottfried, and F.C.W. Dodge, Radiogenic heat production of contrasting magma series: bearing on interpretation of heat flow, Geol. Soc. Amer. Bull., 81, 1447-1462, 1970.

Toksöz, M.N., and P. Bird, Formation and evolution of marginal basins and continental plateaus, in Island Arcs, Deep-Sea Trenches, and Back-Arc Basins, pp. 379-394, AGU, Washington, DC, 1977.

Tsai Y.B., and K. Aki, Precise focal depth determination from amplitude spectra of surface waves, J. Geophys. Res., 75, 5729-5743, 1970.

Tseng, Jung-shen, and Zi-an Sung, Phase velocities of Rayleigh waves in China, Acta Geophys. Sinica, 12, 148-165, 1963.

Tung, J.P., and T.L. Teng, Surface wave study of crustal structure of southern China, EOS Trans. AGU, 55, 359, 1974.

Weidner, D.J., and K. Aki, Focal depth and mechanism of mid-ocean ridge earthquakes, J. Geophys. Res., 78, 1818-1831, 1973.

Table I

Earthquakes used for surface wave dispersions and P_L phase observation

Date	Number	Epicenter Location Lat.(°N)	Longt.(°E)	Origin Time	Stations	Seismic phases
Apr. 19, '63	I	35.7	96.9	07:35:22.7	NDI	LR, P_L
Oct. 16, '63	II	38.6	73.4	15:43:00.8	SHL	LR
Mar. 16, '64	III	36.95	95.50	01:05:19.8	NDI	LR, LG
Oct. 14, '66	IV	36.45	87.43	01:04:42.9	NDI LAH	LR, LG LG
Aug. 30, '67	V	31.57	100.31	11:08:50.0	LAH	LG
Mar. 24, '71	VI	35.46	98.04	13:54:21.0	NDI	LR
Aug. 30, '72	VII	36.65	96.35	15:14:07.5	NDL NIL	LR, LG LG
Aug. 30, '72	VIII	36.56	96.35	18:47:40.3	NDI NIL	LR, LG LG
Feb. 7, '73	IX	31.50	100.33	16:06:25.8	NDI	LG

Hypocenters and origin times as reported by ISC after 1964, by the Coastal and Geodetic Survey before 1964.

Table II

Pn and Sn velocity estimates for Tibet (north of the suture) and regions south of the suture

	Epicentral Distance (deg.) Range	Arrivals	No. of Observations	Travel time (sec) = Distance (km)/velocity (km/s) + Intercept time (sec)
Tibet, north of the suture	3 - 17	all Pn	61	$x/(8.27\pm0.07) + (12.4\pm7.0)$ $x/(8.15\pm0.04) + (10.3\pm4.1)$
		sharp Pn	42	$x/(8.24\pm0.09) + (12.0\pm5.4)$ $x/(8.20\pm0.04) + (10.6\pm2.6)$
		emergent Pn	19	$x/(8.38\pm0.21) + (14.5\pm15.0)$ $x/(8.18\pm0.13) + (11.2\pm9.8)$
	3 - 10	sharp Pn	39	$x/(7.97\pm0.12) + (9.7\pm6.9)$ $x/(8.12\pm0.06) + (10.0\pm3.6)$
		sharp Sn	23	$x/(4.77\pm0.09) + (25.4\pm11.4)$ $x/(4.77\pm0.08) + (23.5\pm9.5)$
Regions south of the suture	3 - 17	all Pn (mostly sharp)	24	$x/(8.20\pm0.11) + (10.4\pm5.2)$ $x/(8.11\pm0.07) + (9.1\pm3.6)$
	3 - 10	all Pn (mostly sharp)	21	$x/(8.29\pm0.15) + (11.0\pm5.8)$ $x/(8.13\pm0.10) + (9.3\pm4.0)$
		sharp Sn	11	$x/(4.94\pm0.11) + (28.3\pm8.8)$ $x/(4.75\pm0.10) + (23.2\pm8.6)$

Results after the depth correction are given on the second line.
All velocities are calculated for a Moho at 70 km depth.

Table III

S-P travel time residuals with respect to the Jeffreys-Bullen Table for earthquakes in Tibet (T) and the Himalaya (H)

Date	Location Lat.(°N)	Long.(°E)	Depth Reported by ISC(km)	No. of Observations	δTs-p (sec) ISC depth	33km Normalized	5km Depth
Mar. 6, '66	31.49	80.50(T)	50	19	11.4±2.4	10.0	7.1
				16	12.1±3.3	10.7	7.8
Oct. 14, '66	36.45	87.43(T)	14	11	6.6±2.2	8.5	5.7
				9	7.9±1.5	9.8	7.0
Jul. 22, '72	31.38	91.41(T)	17	15	4.4±2.9	6.0	3.2
				14	5.3±3.7	6.9	4.1
Jul. 14, '73	35.16	86.40(T)	22	20	7.3±2.7	8.4	5.6
				16	7.8±3.2	8.9	6.1
Jul. 19, '75	32.39	78.50(T)	1	15	1.4±2.4	4.6	1.8
				12	2.9±1.5	6.1	3.3
Apr. 28, '75	35.80	79.86(T)	33	18	3.7±2.2	3.7	0.9
				13	4.1±2.4	4.1	1.3
May 5, '75	33.09	92.92(T)	33	22	5.8±2.3	5.8	2.9
				20	6.7±2.6	6.7	3.8
May 19, '75	35.16	80.80(T)	26	10	4.4±2.8	5.1	3.3
				8	5.3±1.7	6.0	4.2
Jun. 4, '75	35.87	79.85(T)	33	15	4.7±2.7	4.7	1.9
				12	5.6±1.0	5.6	2.8
						Ave.	3.6
							4.5

Table III (cont'd)

Sep. 26, '64	29.96	80.46(H)	50	10	2.7±1.7	1.3	-1.6
				7	3.5±2.2	2.1	-0.8
Oct. 21, '64	28.04	93.75(H)	37	19	2.5±1.8	2.2	-0.8
				18	2.9±2.4	2.6	-0.4
Jun. 27, '66	29.62	80.83(H)	33	15	3.1±1.9	3.1	0.2
				12	2.9±2.8	2.9	0.0
Dec. 16, '66	29.62	80.79(H)	19	14	2.0±2.7	2.3	0.6
				13	1.8±4.0	2.1	0.4
Mar. 14, '67	28.41	94.29(H)	20	19	1.2±2.2	2.3	-0.1
				17	2.4±1.8	3.5	1.1
Feb. 19, '70	27.40	93.96(H)	12	14	-0.5±3.2	1.6	-1.2
				12	1.2±3.1	3.3	0.5
Sep. 3, '72	35.94	73.33(H)	45	16	1.7±1.7	0.7	-2.2
				13	2.3±2.0	1.3	-1.6
Mar. 24, '74	27.66	86.00(H)	20	26	1.3±2.1	2.4	0.0
				21	1.6±2.6	2.7	0.3
						Ave.	
						2.0	
						2.6	

Results after applying the station corrections are given on the second line for each event.

Figure Captions

Fig. 1. Map of Tibet showing earthquake (dots) - station (triangles) combinations used for surface wave dispersion and the P_L phase observation. Events I and II generated large long-period Rayleigh waves. Note the difference in the paths to stations from these two events. Event I was used for the P_L phase observation also. Major strike-slip and thrust faults (see legend) were also plotted following Molnar and Tapponnier [1975].

Fig. 2. (a) Seismograms of clear long period Rayleigh waves and P_L-phase. These are the only Rayleigh wave observations found with a large signal to noise ratio at low frequencies. (b) Representative seismograms observed at stations south of the Himalaya for earthquakes in Tibet. Note that no clear Rayleigh wave signals with period beyond about 30 sec were apparent. Love waves vary from pulse-like signals to dispersed wave trains up to about 60 sec period.

Fig. 3. (a) Group velocity dispersion curves of Rayleigh waves. No clear signal was observed between 30 to 60 sec periods. A 3% maximum error in group velocities would be about 0.1 km/s. (b) Group velocity dispersion curves of Love waves.

Fig. 4. Phase velocity dispersion curves for Rayleigh waves. Observed values for I-NDI path (crosses) and II-SHL path (dots) were plotted together with three theoretical curves calculated for models F4, S7, and S4. Model SE generates nearly identical phase velocity dispersion curve as that of the model S7 at the period range shown. Error bar shown is approximately $\pm$2.4% maximum error in phase velocity. See Figs. 5, 6, and 9 for model parameters.

Fig. 5. Theoretical Rayleigh wave group velocity dispersion curves (top) for three models (bottom) with a crustal thickness of 55 km for different uppermost mantle shear wave velocities (β_m). The two long-period observations are shown as solid triangles for comparison. Also shown is the theoretical Love wave dispersion curve for model F4.

Fig. 6. Theoretical Rayleigh wave group velocity dispersion curves (top) for 3 models (bottom) with a crustal thickness of 70 km for different β_m. Layout sams as in Fig. 5.

Fig. 7. Theoretical Rayleigh wave group velocity dispersion curves (top) for 3 models (bottom) with a crustal thickness of 85 km for different β_m. Model E4 is not refered to. Layout same as in Fig. 5.

Fig. 8. (a) Theoretical Rayleigh wave group velocity dispersion curves (top) for 3 models (bottom) with β_m = 4.4 km/s and a crust of 55 km thick but with different velocity structures in the crust. The average crustal shear velocity ($\bar{\beta}$) ranges from 3.49 km/s to 3.44 km/s. The model FF3 which fits the observations is the same as model F4 (Fig. 5). The upper and lower bound of our observations are shown in reversed solid triangles and solid triangles respectively. (b) Theoretical Rayleigh wave group velocity dispersion curves (top) for 4 models (bottom) with a fixed crustal thickness (55 km), β_m (4.4 km/s) and $\bar{\beta}$ (3.44 km/s). Note that a uniform crust between the Moho and the sediments with this low $\bar{\beta}$ does not fit the observations.

Fig. 9. (a) Theoretical Rayleigh wave group velocity dispersion curves (top) for 3 models (bottom) with fixed crustal thickness (70 km), and β_m (4.7 km/s). $\bar{\beta}$ ranges from 3.53 to 3.45 km/s. For all cases the velocities are too high. Layout same as Fig. 8. (b) Theoretical Rayleigh wave group velocity dispersion curves (top) for 3 models (bottom). Model SS3 in (a) is plotted for comparison. The addition of a relatively high velocity layer (β = 3.9 km/s) makes model SS5 (= model S7, Fig. 6) fit the data at both long period and short period ends. Model SE is described in (c). (c) Theoretical Rayleigh wave group velocity dispersion curves for models SE and

SS5. The slight increase in β_m in SE has the same effect as the introduction of a layer at the base of the crust with β = 3.9 km/s in SS5 (see (b)). Also note that model S7 (SS5) and SE have nearly identical phase velocity dispersion curves (Fig. 4).

Fig. 10. (a) Two synthetic seismograms for different Q structures together with low-pass filtered vertical component Rayleigh wave of the II-SHL path observation. Both synthetics employ model S7 (Fig. 6) with source depth 5 km and an arbitrary seismic moment. All the seismograms have been normalized to have the same maximum peak-to-peak amplitude, emphasizing their similarity in wave forms, and for each the portion earlier than 590 sec has been truncated. (b) Three low-pass filtered synthetic seismograms of the vertical component of Rayleigh waves for model S7 with different source depths of 5, 10 and 30 km. Amplitude scales have been normalized as in (a). (c) Low-pass filtered vertical component of the Rayleigh wave signal from the I-NDI path together with three synthetic seismograms for different velocity structures: models F7, S4, S7 (Figs. 5 and 6). Amplitude scales have been normalized as in (a). Note the particularly poor fit of model F7.

Fig. 11. (a) Vertical component of the long-period P_L phase for the I-NDI path (solid trace) and one synthetic seismogram (dashed trace) for a 70 km thick crust (single layer over a half-space) model, with an arbitrary seismic moment. The large amplitude P wave at the beginning of the observation results from deep mantle reflections and refractions that were not synthesized. (b) Two synthesized vertical components of P_L phases for layer-over-half space models with different crustal thicknesses of 70 and 85 km. P and S wave velocities for crust and mantle are shown in the lower-right corner. Note the similarity between the two waveforms. (c) Synthesized vertical component of a P_L phase for model SEM1 (dashed trace) together with the observed signal. The inclusion of a crustal reflector alters the long-period waveform considerably from the pulse like character in (b).

Fig. 12. Plots of P_n travel times normalized for a focal depth of 33 km (top) and travel time residuals (bottom) vs. distance to LHA for earthquakes north of the Indus-Tsang Po suture. The distance range is about 3°-17°. The P_n velocity (8.15$\pm$0.04 km/s) and travel time residuals were obtained by a least-square fitting of the 61 observations assuming a Moho depth of 70 km. Most of the residuals fall within $\pm$1 sec of the mean.

The dashed line shows the slope of a curve to which the data would be parallel if the P_n velocity were 7.9 km/s. Travel time residuals can be viewed as reduced travel times in conventional refraction analysis.

Fig. 13. (a) Plots of P_n travel time residuals without depth normalization vs. distance to LHA for earthquakes north of the Indus-Tsang Po suture. Distance range is 3°-10°. (b) The same dataset as in (a) but with a normalization for a focal depth of 33 km. Note the reduction of residuals compared with (a). Layout as in Fig. 12.

Fig. 14. Plots of P_n travel time residuals normalized for a focal depth of 33 km vs. distance to LHA for earthquakes south of the Indus-Tsang Po suture. Distances range from 3° to 10°. Layout same as in Fig. 12.

Fig. 15. Plots of S_n travel time residuals normalized for focal depths of 33 km vs. distance to LHA for earthquakes north of the Indus-Tsang Po suture. Distances range 3° to 10°. Layout as in Fig. 12.

Fig. 16. Map of Tibet showing the location of LHA and the epicenters used for the refraction profiles. Tectonic features are the same as in Fig. 1.

Fig. 17. Map of Tibet and the Himalaya showing the locations of 17 earthquakes (circles) used in teleseismic travel time measurements. Roman numerals inside the circles are the S-P travel time residuals with respect to the J-B tables. All the values are rounded to the smaller nearest integer and are given at 1 sec intervals. Source depths have been normalized to 5 km for earthquakes in Tibet and to 33 km for those in the Himalaya. Tectonic features are the same as in Fig. 1.

Fig. 18. Examples of seismograms used in the teleseismic travel time measurements for earthquakes in Tibet and the Himalaya. Arrows indicate the onset of S wave arrivals. Numbers in the parentheses are S wave travel time residuals in sec with respect to the J-B table for the source depths given by the ISC.

Fig. 19. (a) Plots of teleseismic P and S wave travel time residuals with respect to the J-B tables vs. distance for earthquakes in Tibet (b) S-P travel time residuals (circles). The crosses are the results after station corrections have been added. Dashed line shows the zero-residual level for a focal depth normalized to 5 km. The averaged S-P delays are given in Table III with estimated standard errors.

Fig. 20. (a) Plots of teleseismic P and S wave travel time residuals with respect to the J-B tables vs. distance for earthquakes in the Himalaya. (b) S-P travel time residuals. Symbols are the same as in Fig. 19.

Fig. 21. Average S-P travel time residuals for earthquakes in Tibet (left) and the Himalaya (right). Hatched and open columns are average residuals without and with the station corrections, respectively. The residuals are given for three different focal depths: 5 km (top), 33 km (middle) and the depth reported by the ISC (bottom).

Fig. 22. Solidi of selected possible crustal and upper mantle materials of different water content from data obtained from experimental petrology [Lambert and Wyllie, 1970, Merrill et al., 1970, Merrill and Wyllie, 1975]. Dashed lines indicate areas of large uncertainty cited in the original literature.

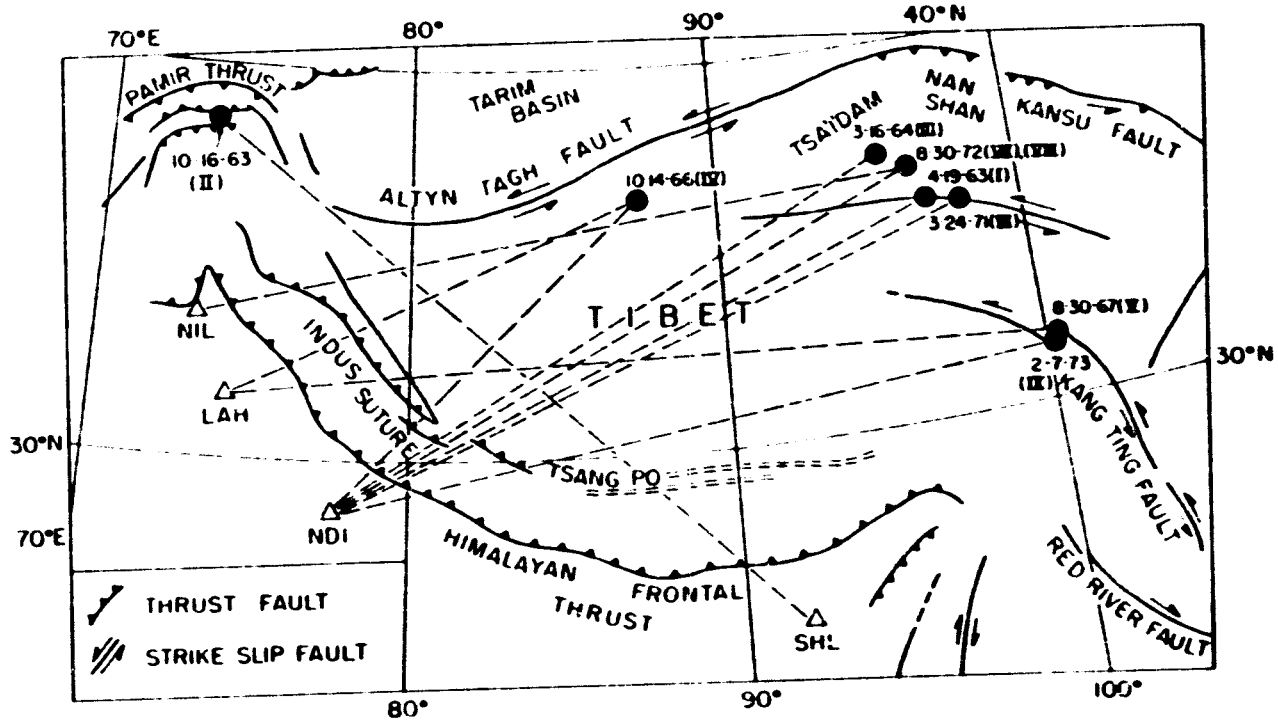
70°E
80°
90°
40°N
PAMIR THRUST
TARIM BASIN
ALTYN TAGH FAULT
TSAIDAM
NAN SHAN
KANSU FAULT
10 16-63 (II)
10 14-66 (IX)
3-15-64 (IX)
8 30-72 (IX) (IX)
4-19-63 (II)
3 24-74 (IX)
8 30-67 (IX)
2-7-73 (IX)
T I B E T
NIL
LAH
INDUS SUTURE
30°N
TSANG PO
NDI
HIMALAYAN FRONTAL THRUST
SHL
RED RIVER FAULT
ANG TING FAULT
THRUST FAULT
STRIKE SLIP FAULT
80°
90°
100°

fig. 1

Mar 16, 64 NDI

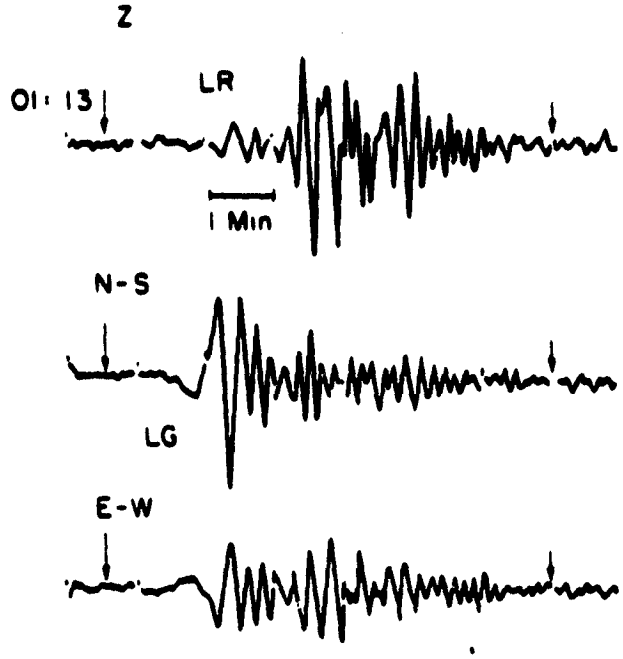

Aug. 30, 67 LAH Z

Aug. 30, 72 NDI

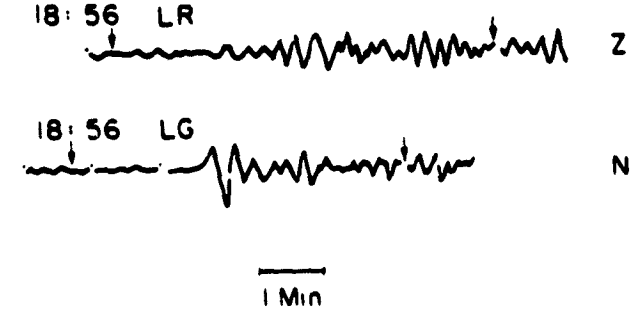

fig 2(b)

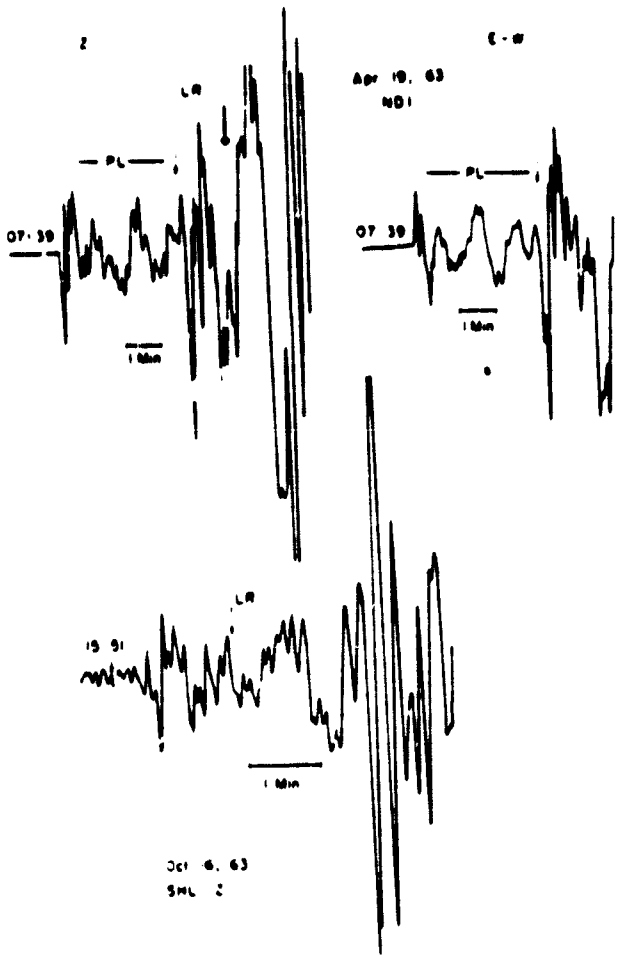
Z
LR
PL
07 39
1 Min
E - W
Apr 19, 63
MDI
PL
07 39
1 Min
LR
15 91
1 Min
Oct 16, 63
SHL Z

fig 2a)

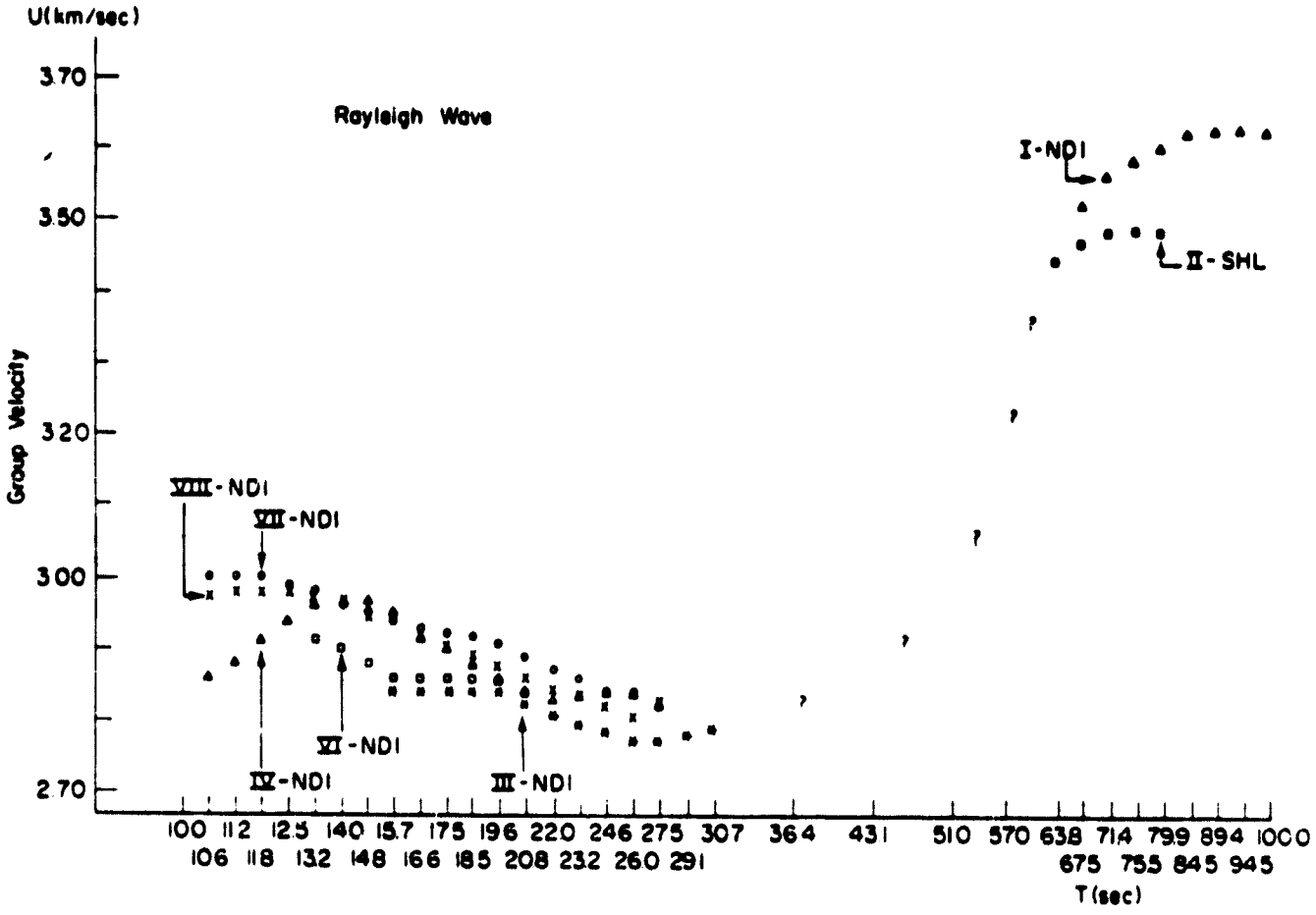
U(km/sec)
3.70
3.50
3.20
3.00
2.70
Group Velocity
Rayleigh Wave
I-NDI
II-SHL
VIII-NDI
VII-NDI
VI-NDI
IV-NDI
III-NDI
100 112 125 140 157 175 196 220 246 275 307 364 431 510 570 638 714 799 894 1000
106 118 132 148 166 185 208 232 260 291 675 755 845 945
T(sec)

fig. 3(a)

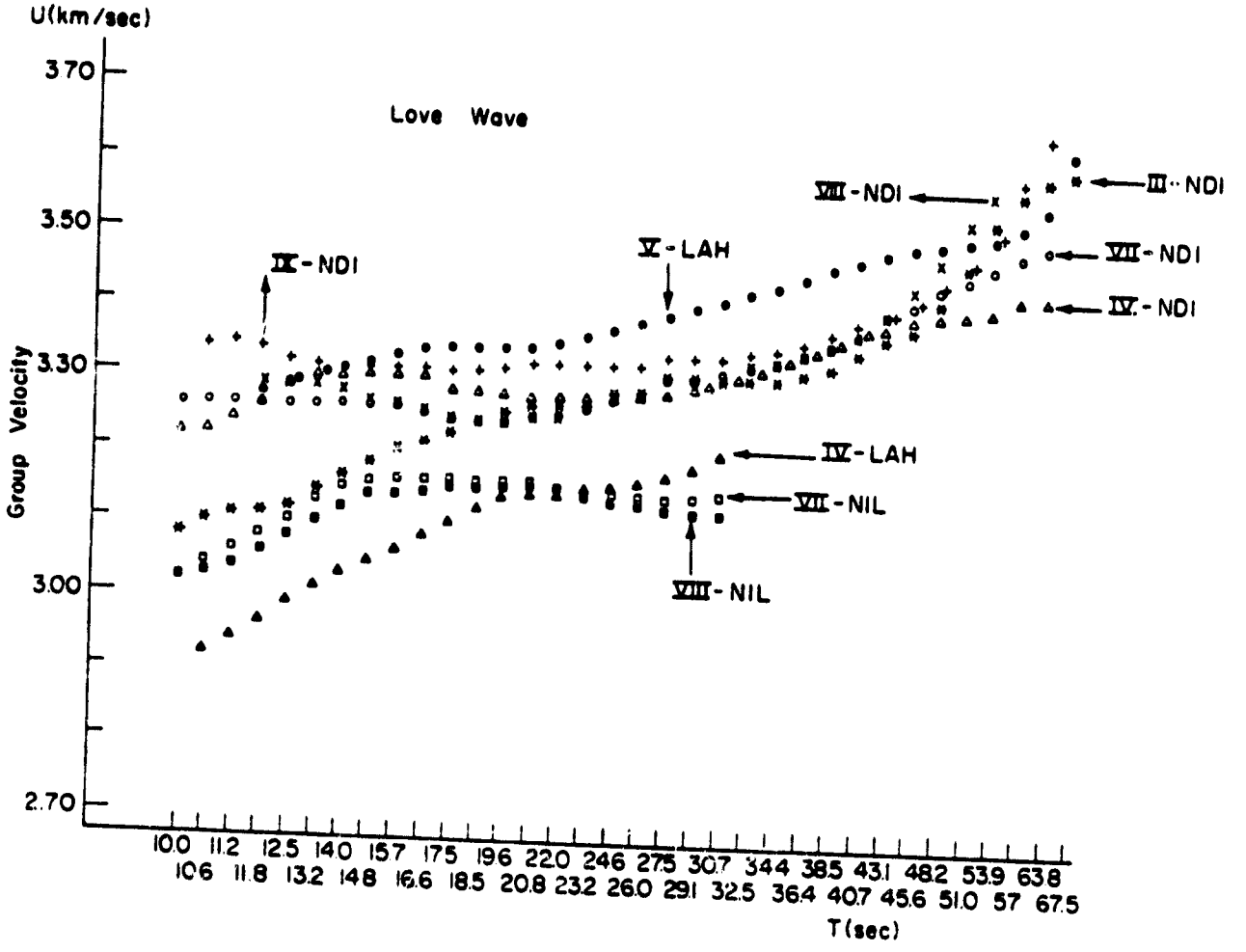
U(km/sec)
3.70
3.50
3.30
3.00
2.70
Group Velocity
Love Wave
IX - NDI
V - LAH
VIII - NDI
III - NDI
VII - NDI
IV - NDI
IV - LAH
VII - NIL
VIII - NIL
10.0 11.2 12.5 14.0 15.7 17.5 19.6 22.0 24.6 27.5 30.7 34.4 38.5 43.1 48.2 53.9 63.8
10.6 11.8 13.2 14.8 16.6 18.5 20.8 23.2 26.0 29.1 32.5 36.4 40.7 45.6 51.0 57 67.5
T(sec)

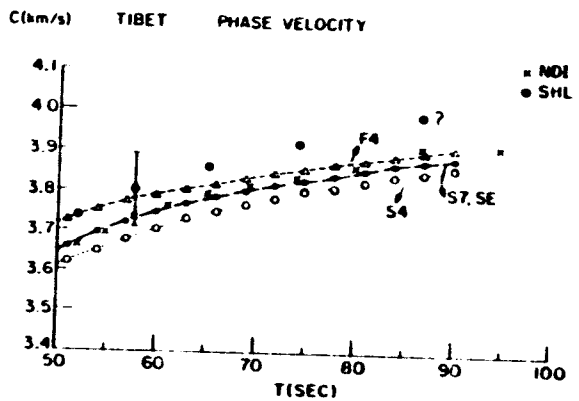
C(km/s)
TIBET
PHASE VELOCITY
× NDI
● SHL
4.1
4.0
3.9
3.8
3.7
3.6
3.5
3.4
50
60
70
80
90
100
T(SEC)
● ?
F4
S4
S7, SE

fig. 4

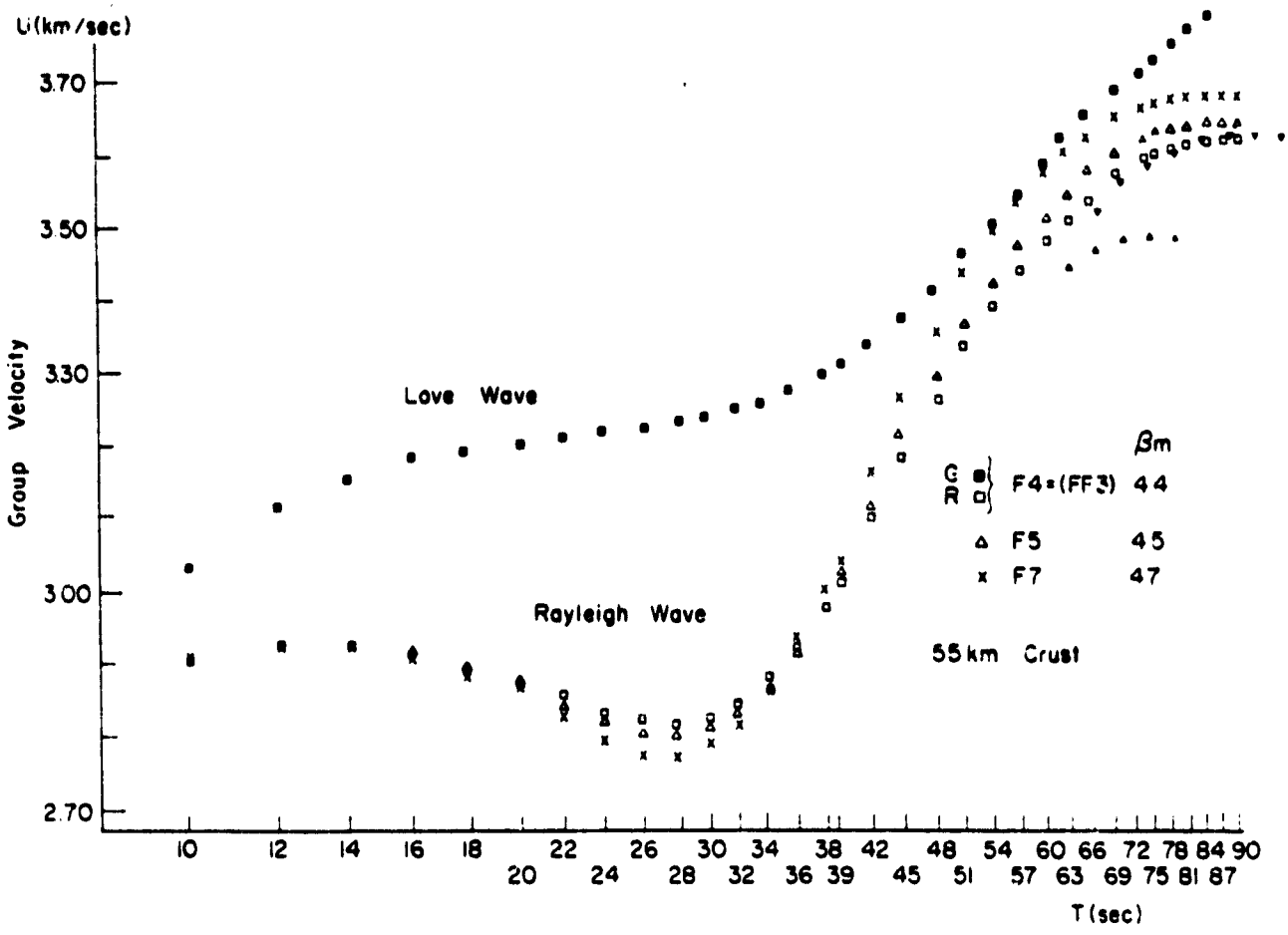
U(km/sec)
3.70
3.50
3.30
3.00
2.70
Group Velocity
Love Wave
Rayleigh Wave
55km Crust
βm
G
R
F4=(FF3) 44
F5 45
F7 47
10 12 14 16 18 20 22 24 26 28 30 32 34 36 39 42 45 48 51 54 57 60 63 66 69 72 75 78 81 84 87 90
T(sec)

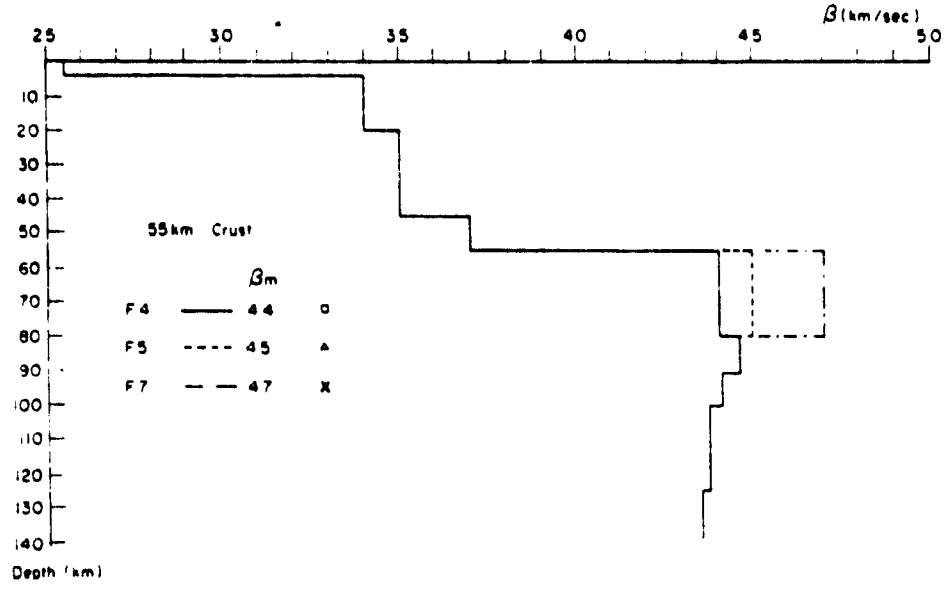
β(km/sec)
25 30 35 40 45 50
10 20 30 40 50 60 70 80 90 100 110 120 130 140
Depth (km)
55km Crust
βm
F4 44
F5 45
F7 47

Fig 1-

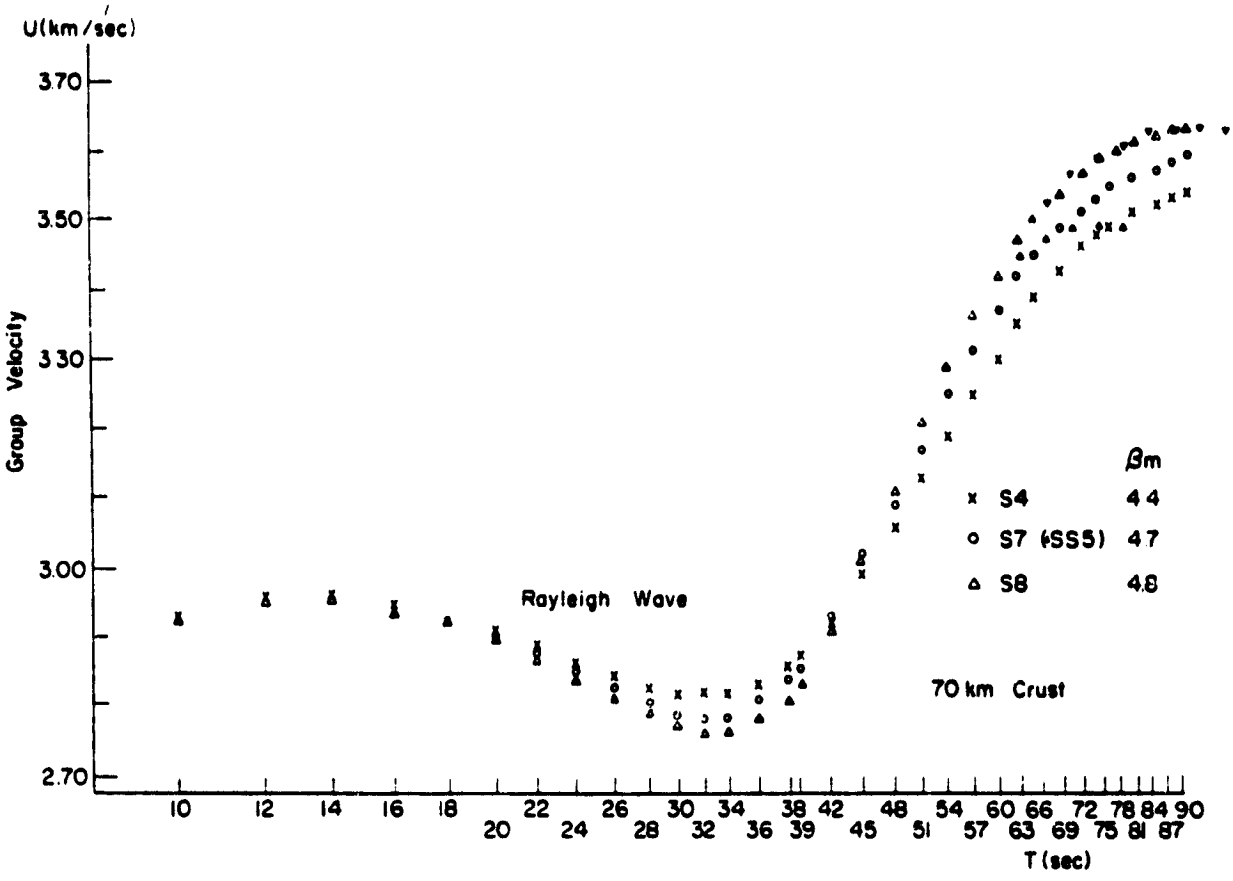
U(km/sec)
3.70
3.50
3.30
3.00
2.70
Group Velocity
Rayleigh Wave
70 km Crust
βm
S4 4.4
S7 (SS5) 4.7
S8 4.8
10 12 14 16 18 20 22 24 26 28 30 32 34 36 38 39 42 45 48 51 54 57 60 63 66 69 72 75 78 81 84 87 90
T (sec)

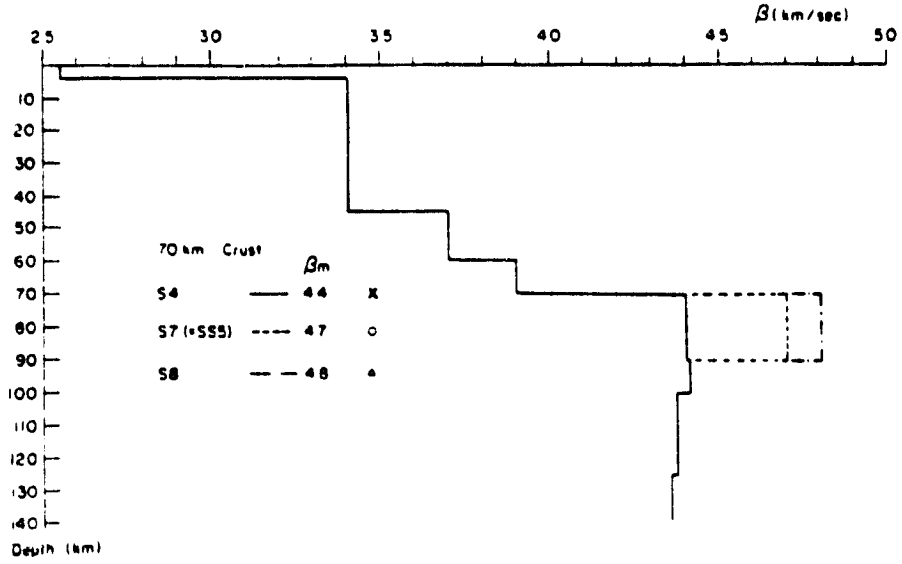
β(km/sec)
25 30 35 40 45 50
10 20 30 40 50 60 70 80 90 100 110 120 130 140
Depth (km)
70 km Crust
βm
S4 — 4.4 x
S7 (+SS5) ---- 4.7 o
S8 — — 4.8 Δ

fig. 6

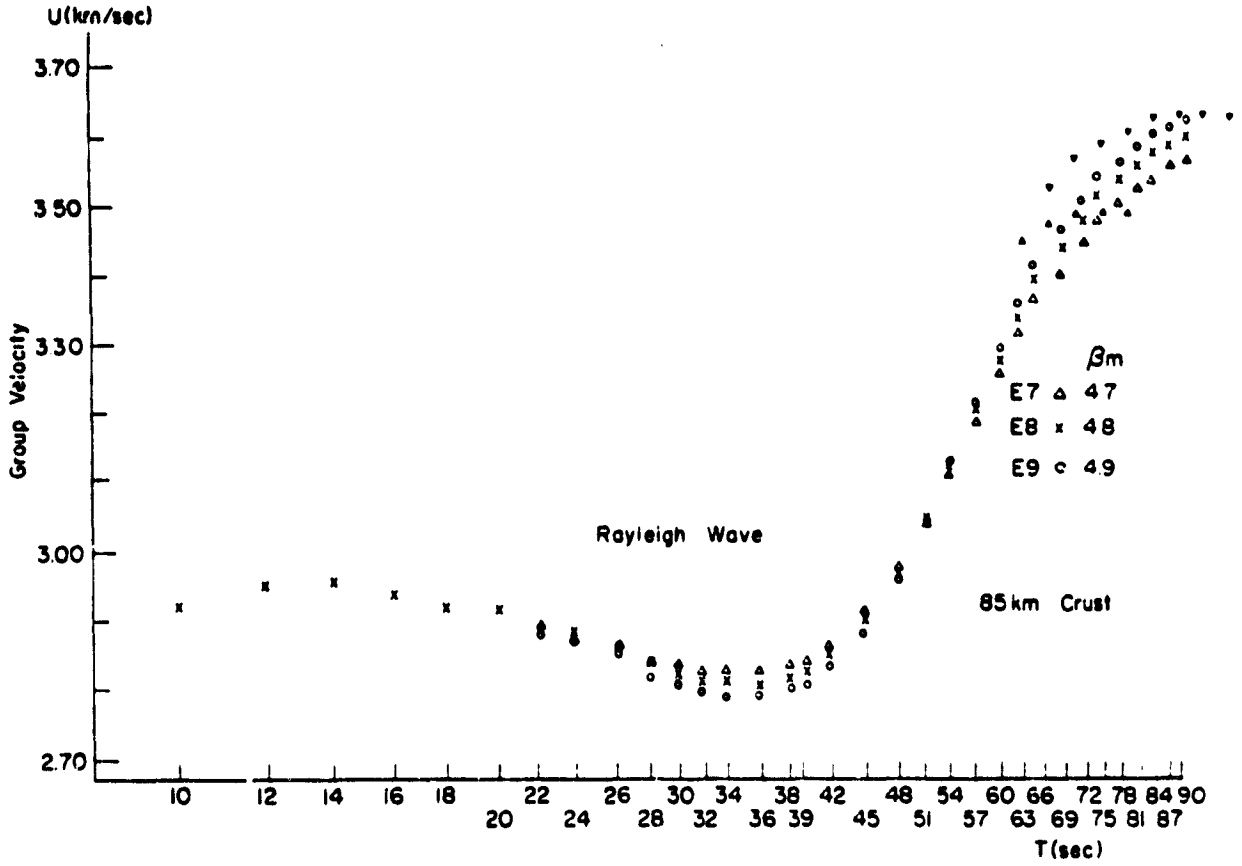
U(km/sec)
3.70
3.50
3.30
3.00
2.70
Group Velocity
Rayleigh Wave
85 km Crust
βm
E7 △ 4.7
E8 × 4.8
E9 ○ 4.9
10 12 14 16 18 20 22 24 26 28 30 32 34 36 39 42 45 48 51 54 57 60 63 66 69 72 75 78 81 84 87 90
T(sec)

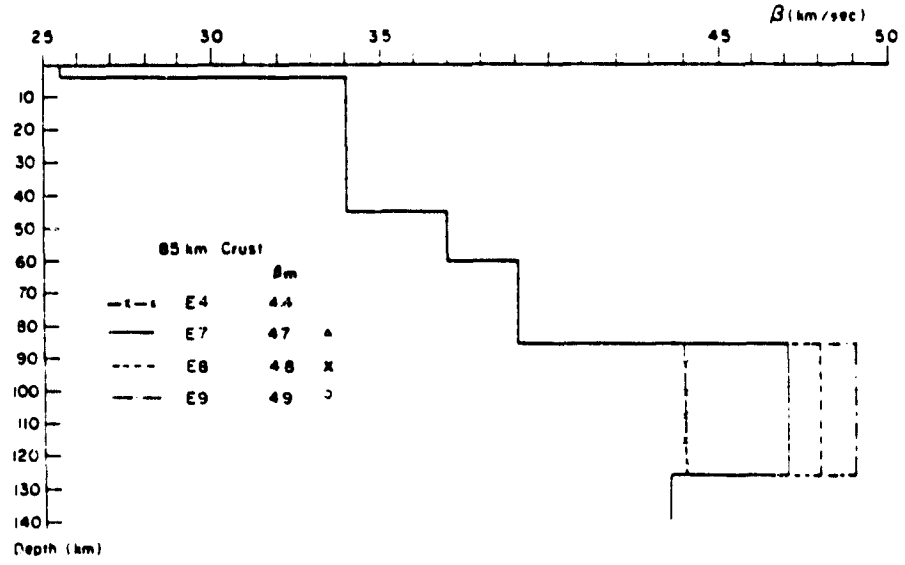
β(km/sec)
25 30 35 45 50
10 20 30 40 50 60 70 80 90 100 110 120 130 140
Depth (km)
85 km Crust
βm
E4 4.4
E7 4.7 △
E8 4.8 ×
E9 4.9 ○

fig. 7

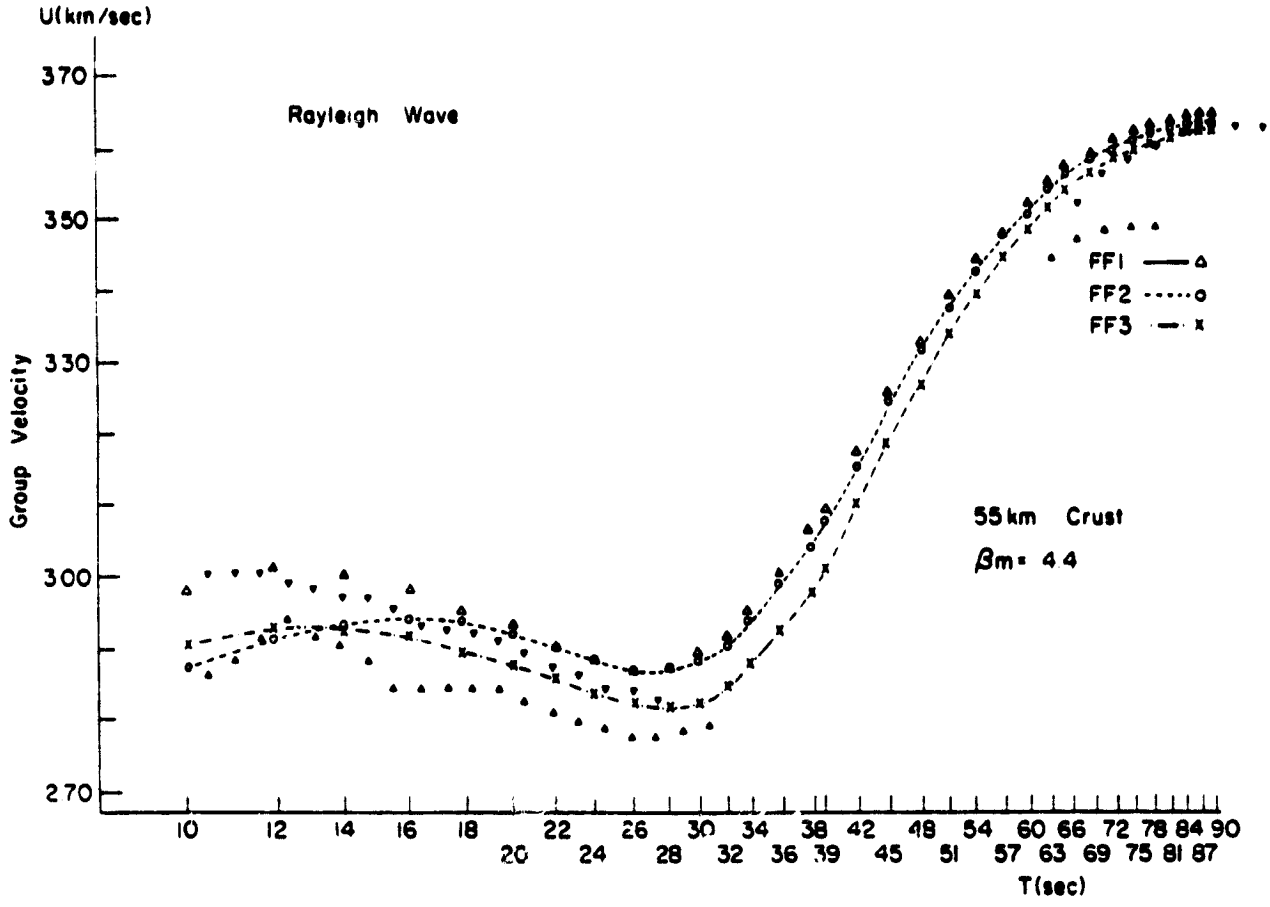
U(km/sec)
370
350
330
300
270
Group Velocity
Rayleigh Wave
FF1
FF2
FF3
55km Crust
βm= 4.4
10 12 14 16 18 20 22 24 26 28 30 32 34 36 38 39 42 45 48 51 54 57 60 63 66 69 72 75 78 81 84 87 90
T(sec)

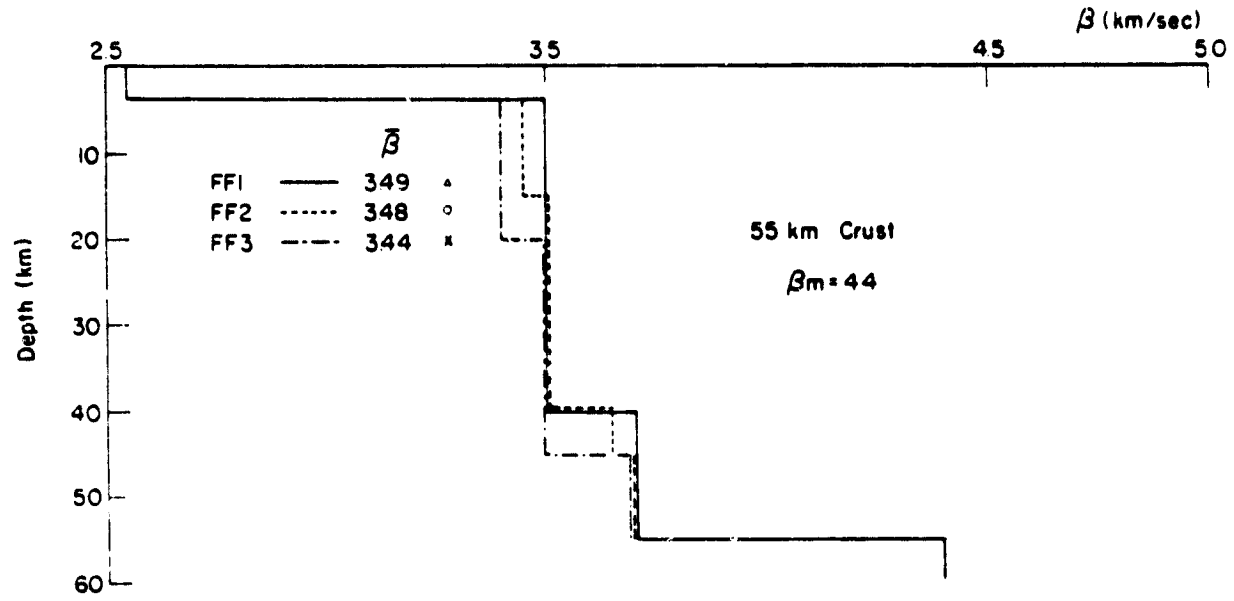
β (km/sec)
2.5
3.5
4.5
5.0
Depth (km)
10
20
30
40
50
60
β̄
FF1 349
FF2 348
FF3 344
55 km Crust
βm=4.4

fig. 8(a)

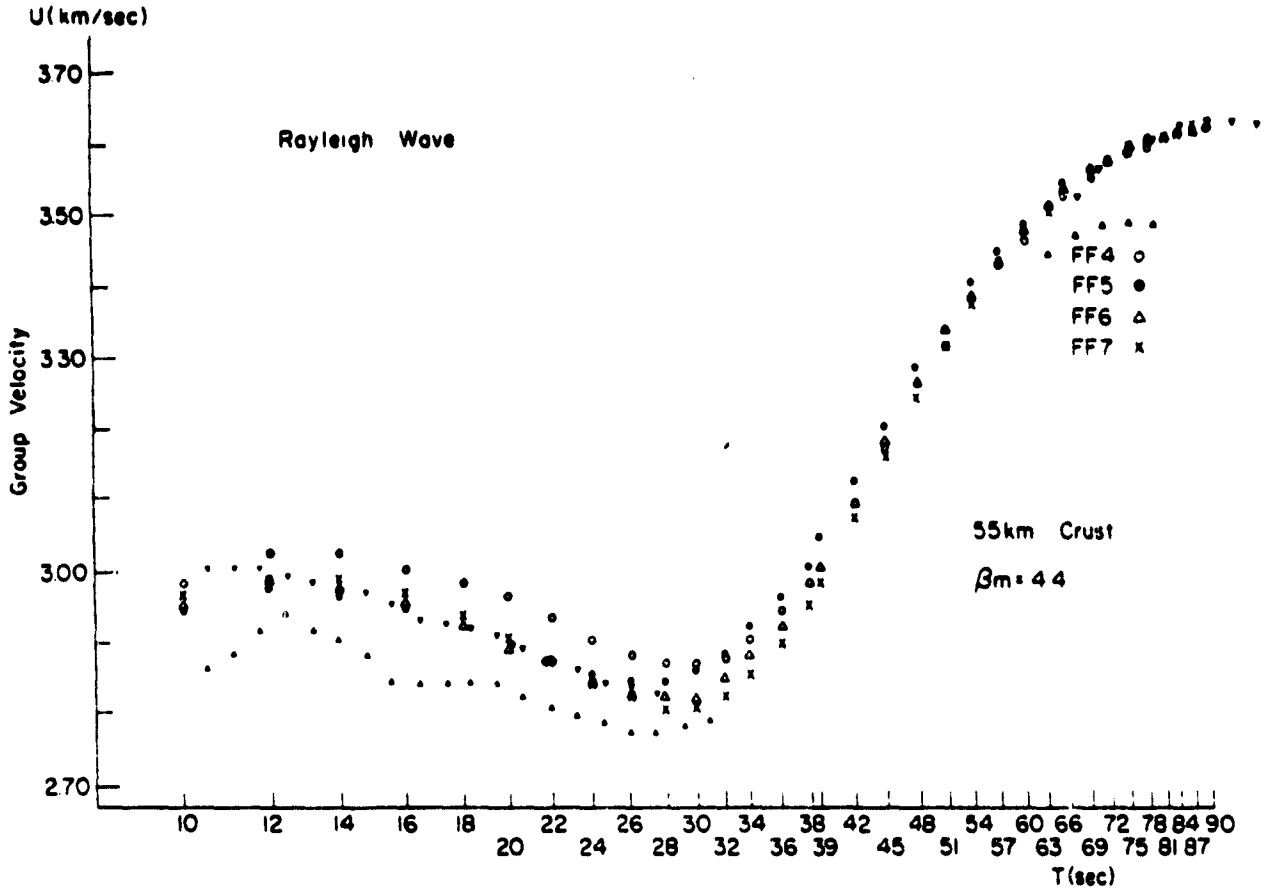
U(km/sec)
3.70
3.50
3.30
3.00
2.70
Group Velocity
Rayleigh Wave
FF4
FF5
FF6
FF7
55km Crust
βm=4.4
10 12 14 16 18 20 22 24 26 28 30 32 34 36 38 39 42 45 48 51 54 57 60 63 66 69 72 75 78 81 84 87 90
T(sec)

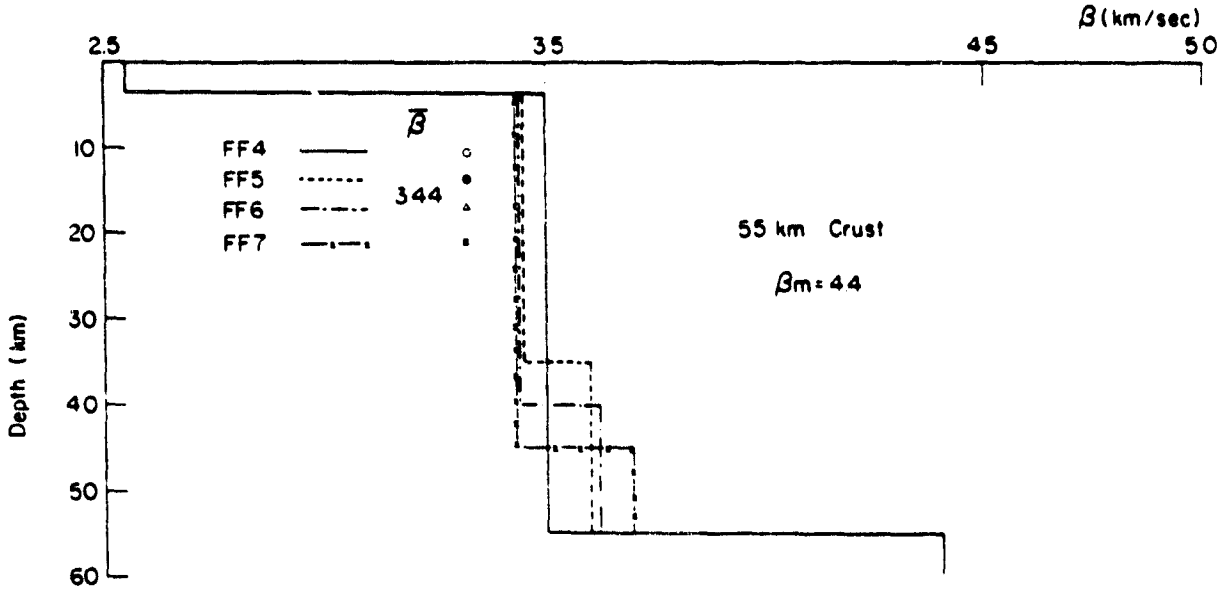
β(km/sec)
2.5
3.5
4.5
5.0
β̄
FF4
FF5
FF6
FF7
3.44
55 km Crust
βm=4.4
10
20
30
40
50
60
Depth (km)

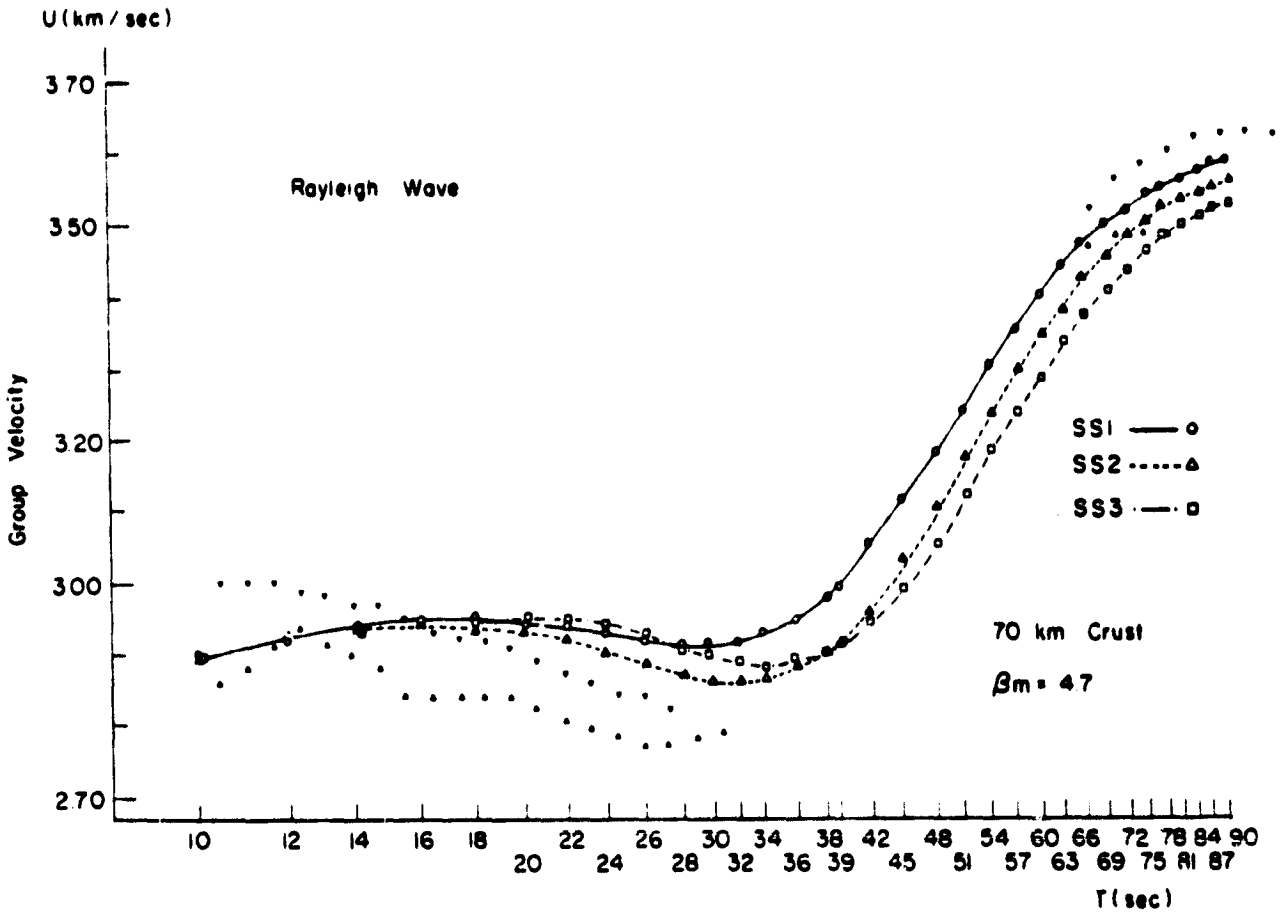
U(km/sec)
3.70
3.50
3.20
3.00
2.70
Group Velocity
Rayleigh Wave
SS1
SS2
SS3
70 km Crust
βm = 4.7
10 12 14 16 18 20 22 24 26 28 30 32 34 36 38 39 42 45 48 51 54 57 60 63 66 69 72 75 78 81 84 87 90
T(sec)

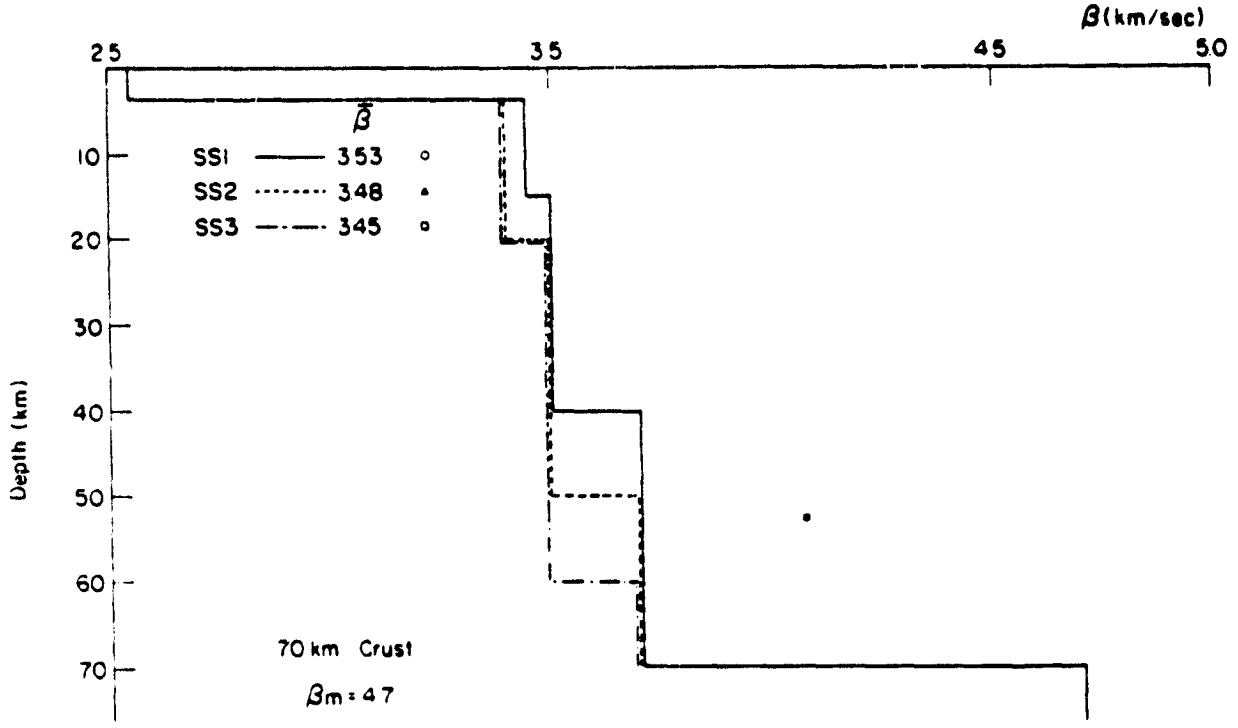
β(km/sec)
2.5
3.5
4.5
5.0
β̄
SS1 3.53
SS2 3.48
SS3 3.45
10
20
30
40
50
60
70
Depth (km)
70 km Crust
βm = 4.7

Fig. 9(a)

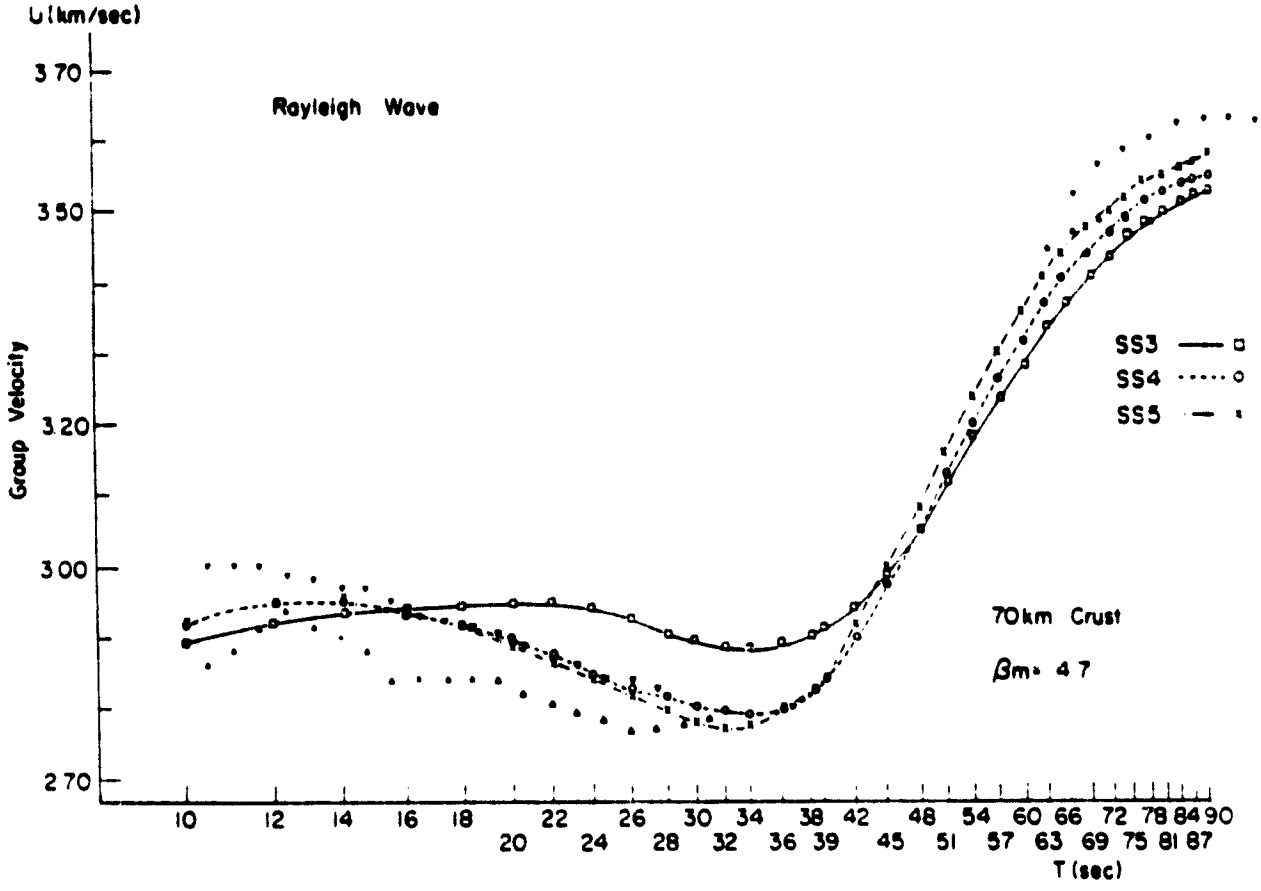
U(km/sec)
3.70
3.50
3.20
3.00
2.70
Group Velocity
Rayleigh Wave
SS3
SS4
SS5
70km Crust
βm= 4.7
10 12 14 16 18 20 22 24 26 28 30 32 34 36 38 39 42 45 48 51 54 57 60 63 66 69 72 75 78 81 84 87 90
T (sec)

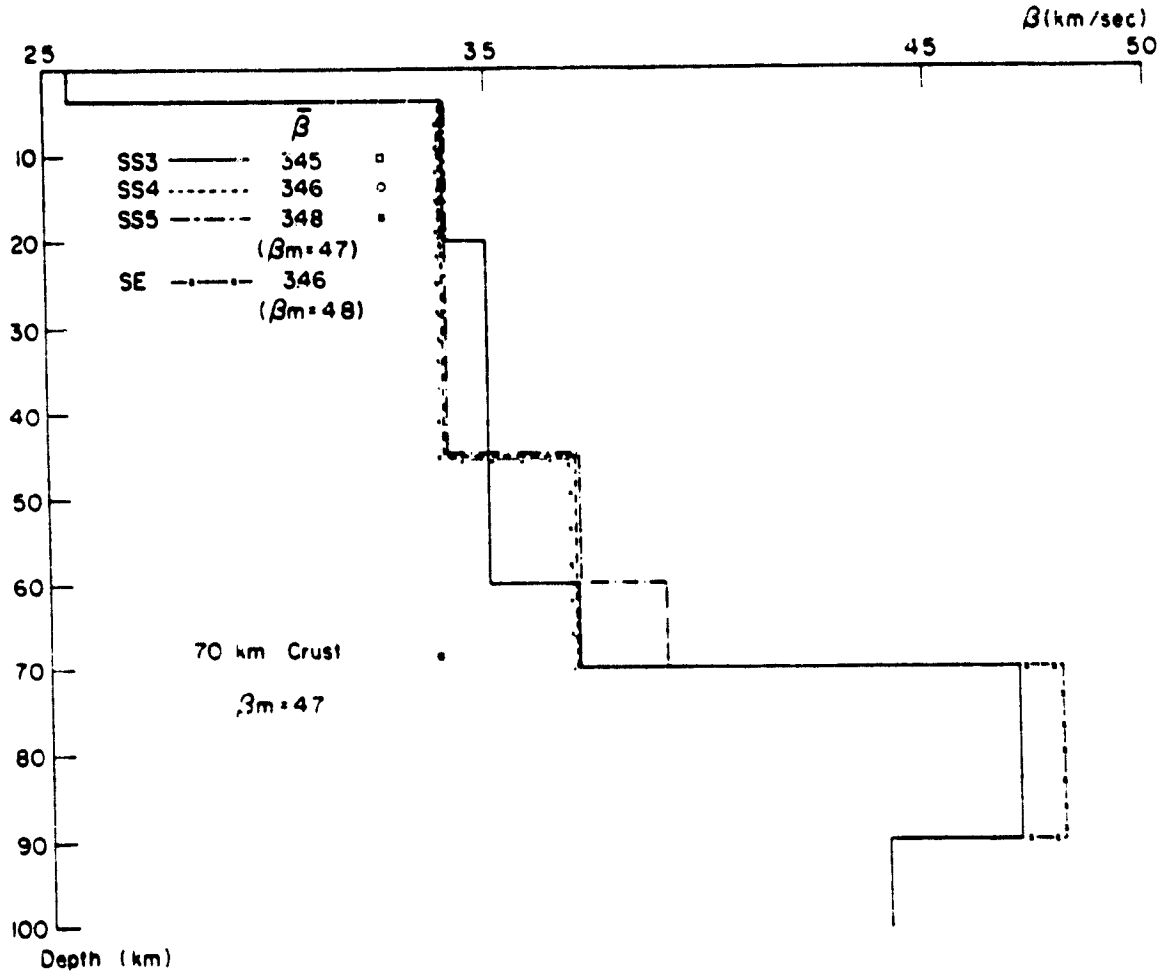
β(km/sec)
2.5
3.5
4.5
5.0
β̄
SS3 3.45
SS4 3.46
SS5 3.48
(βm=4.7)
SE 3.46
(βm=4.8)
10
20
30
40
50
60
70
80
90
100
70 km Crust
βm=4.7
Depth (km)

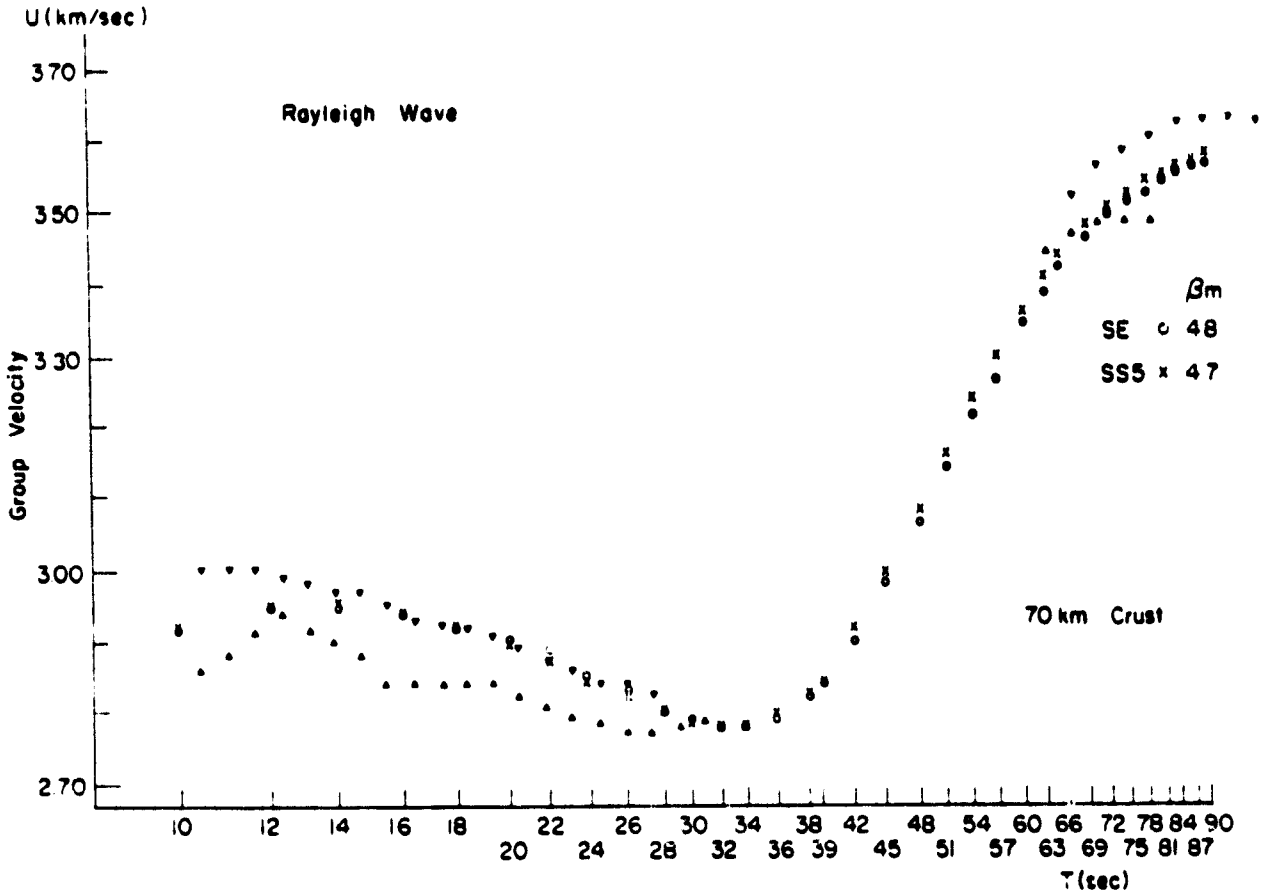
U(km/sec)
3.70
3.50
3.30
3.00
2.70
Group Velocity
Rayleigh Wave
βm
SE ○ 4.8
SS5 × 4.7
70 km Crust
10 12 14 16 18 20 22 24 26 28 30 32 34 36 38 39 42 45 48 51 54 57 60 63 66 69 72 75 78 81 84 87 90
T(sec)

Fig. 8(c)

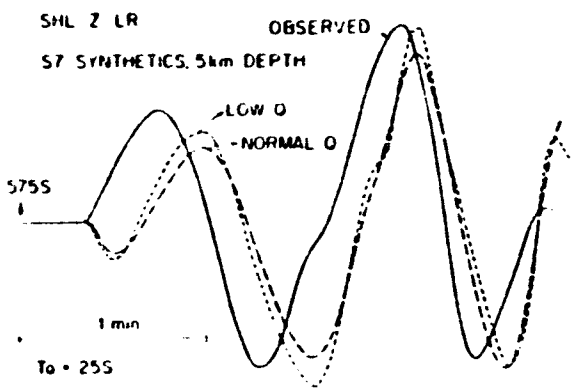

fig. 10(a)

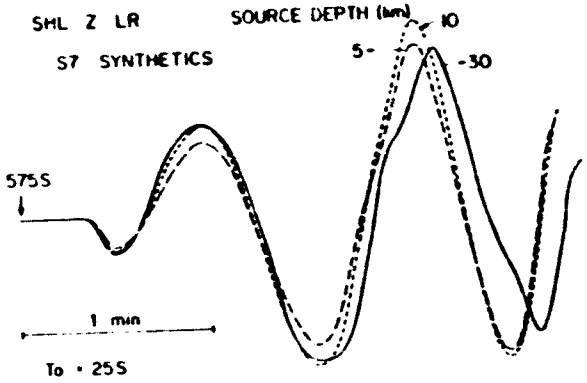

fig. 10(b)

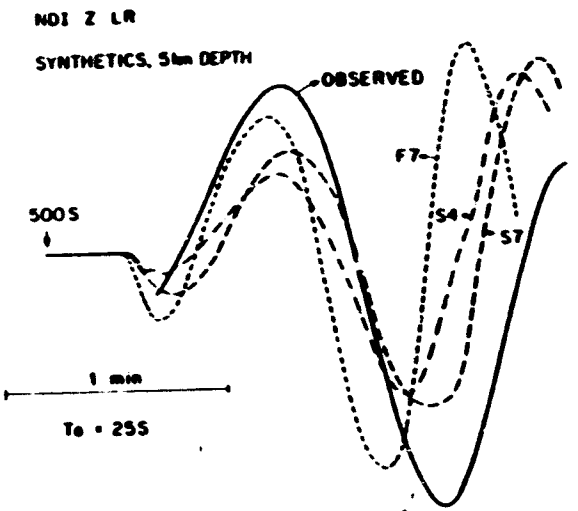

fig. 10(c)

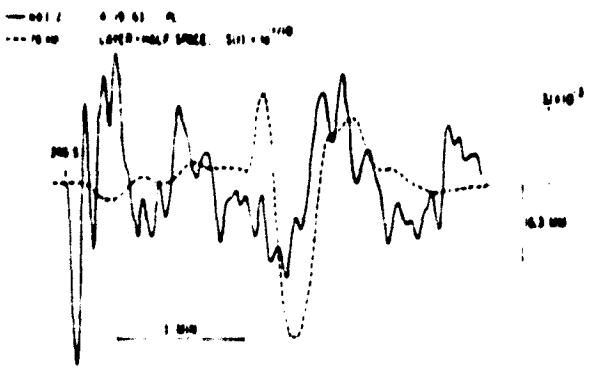

Fig. 11 (a)

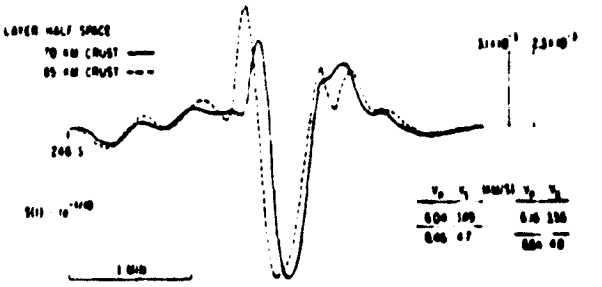

Fig. 11 (b)

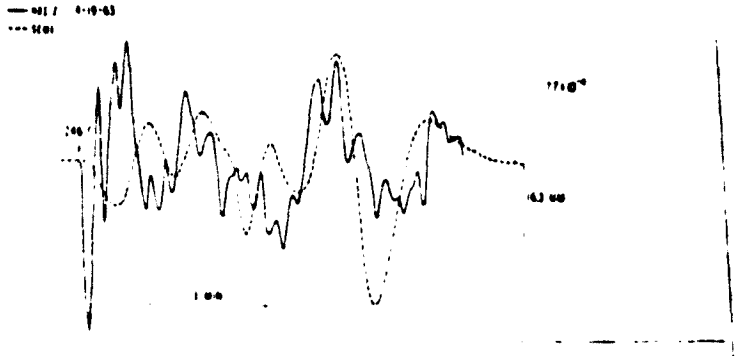

Fig. 11 (c)

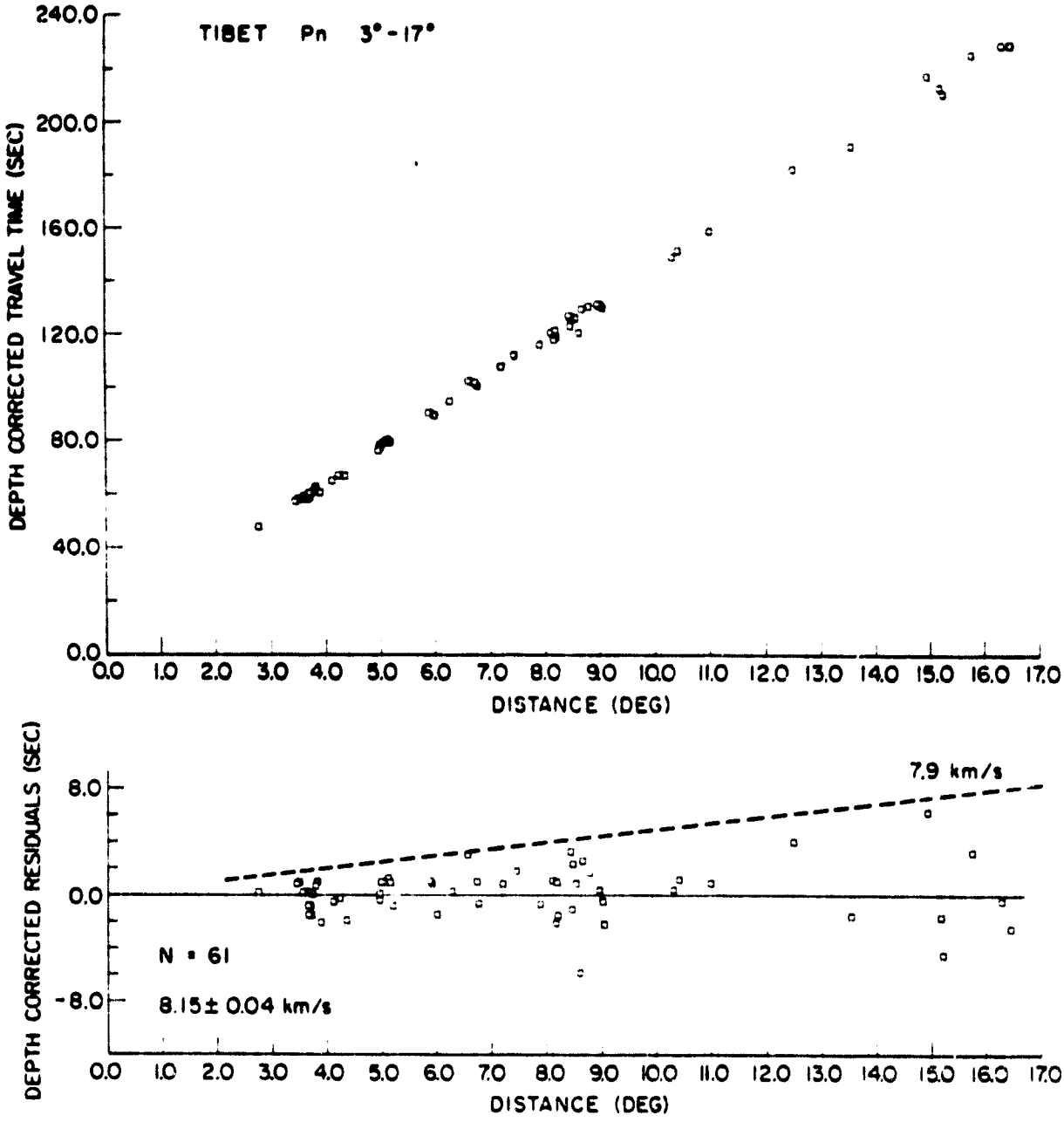
TIBET Pn 3°-17°
DEPTH CORRECTED TRAVEL TIME (SEC)
240.0
200.0
160.0
120.0
80.0
40.0
0.0
0.0 1.0 2.0 3.0 4.0 5.0 6.0 7.0 8.0 9.0 10.0 11.0 12.0 13.0 14.0 15.0 16.0 17.0
DISTANCE (DEG)
DEPTH CORRECTED RESIDUALS (SEC)
8.0
0.0
-8.0
7.9 km/s
N = 61
8.15± 0.04 km/s
0.0 1.0 2.0 3.0 4.0 5.0 6.0 7.0 8.0 9.0 10.0 11.0 12.0 13.0 14.0 15.0 16.0 17.0
DISTANCE (DEG)

Fig. 12

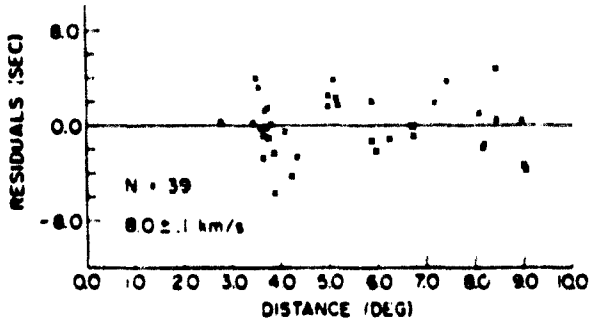

fig. 13 (a)

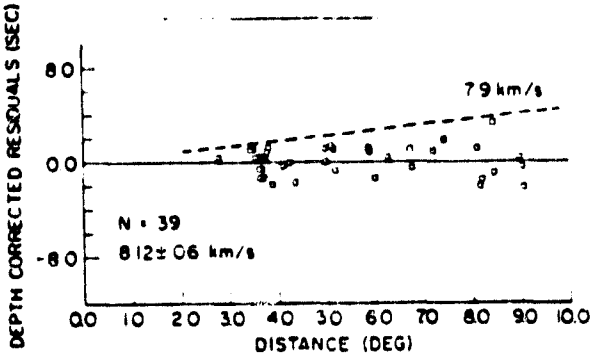

fig 13(b)

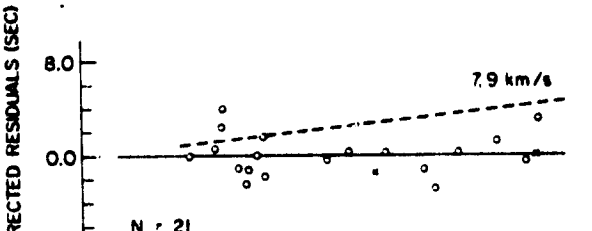

fig. 14

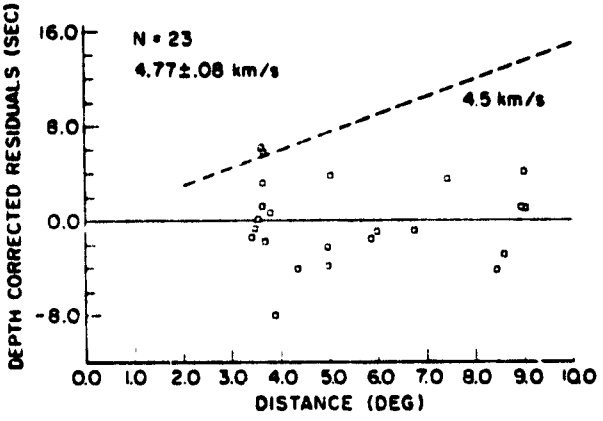
N = 23
4.77±.08 km/s
4.5 km/s
DEPTH CORRECTED RESIDUALS (SEC)
16.0
8.0
0.0
-8.0
0.0 1.0 2.0 3.0 4.0 5.0 6.0 7.0 8.0 9.0 10.0
DISTANCE (DEG)

fig. 15

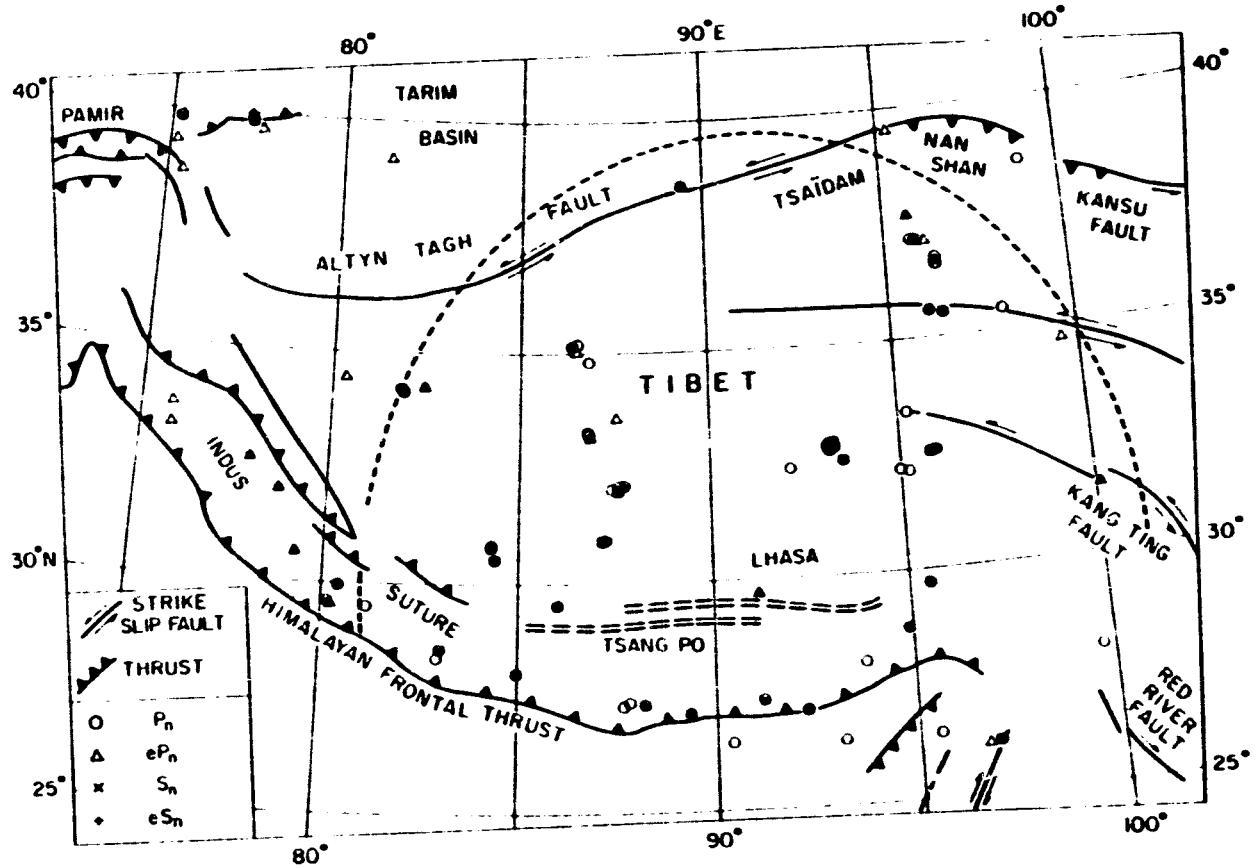
80°
90°E
100°
40°
35°
30°N
25°
PAMIR
TARIM
BASIN
ALTYN TAGH
FAULT
TSAÏDAM
NAN
SHAN
KANSU
FAULT
TIBET
INDUS
SUTURE
LHASA
KANG TING
FAULT
TSANG PO
HIMALAYAN FRONTAL THRUST
RED
RIVER
FAULT
STRIKE
SLIP FAULT
THRUST
Pn
ePn
Sn
eSn

Fig 16

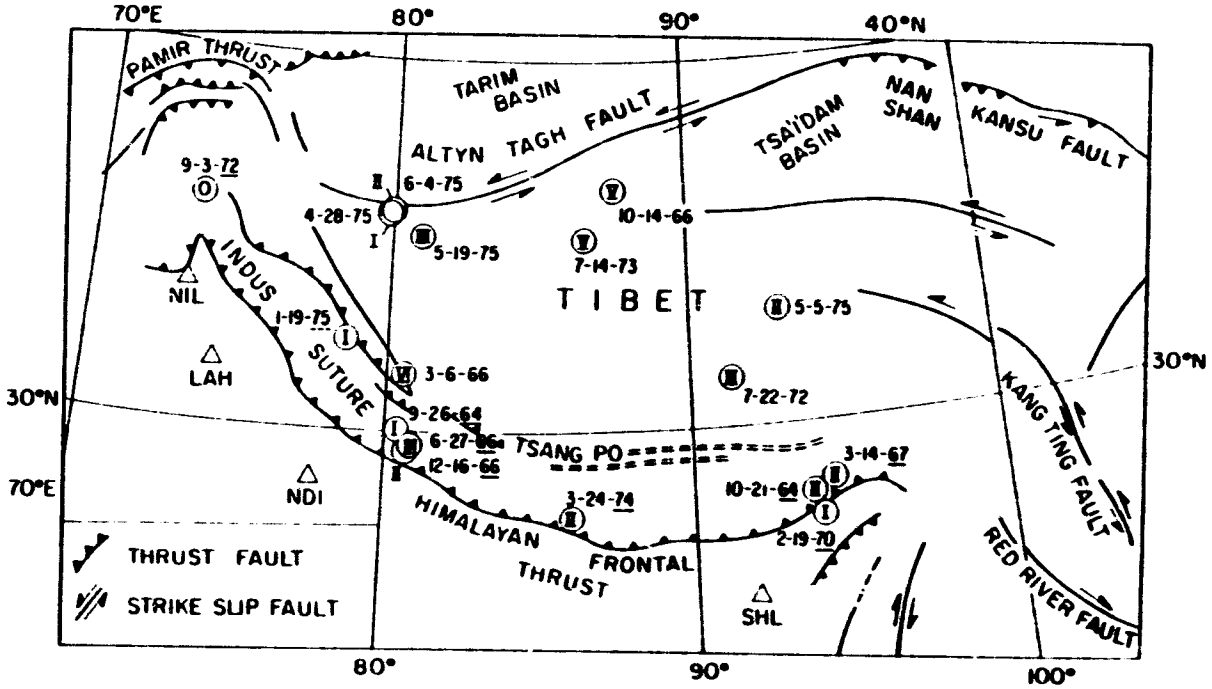
70°E
80°
90°
40°N
30°N
70°E
80°
90°
100°
PAMIR THRUST
TARIM BASIN
ALTYN TAGH FAULT
TSA'IDAM BASIN
NAN SHAN
KANSU FAULT
TIBET
INDUS SUTURE
NIL
LAH
NDI
SHL
TSANG PO
KANG TING FAULT
RED RIVER FAULT
HIMALAYAN FRONTAL THRUST
9-3-72
6-4-75
4-28-75
5-19-75
10-14-66
7-14-73
5-5-75
1-19-75
3-6-66
9-26-64
6-27-66
12-16-66
7-22-72
3-14-67
10-21-64
3-24-74
2-19-70
THRUST FAULT
STRIKE SLIP FAULT

fig 1a

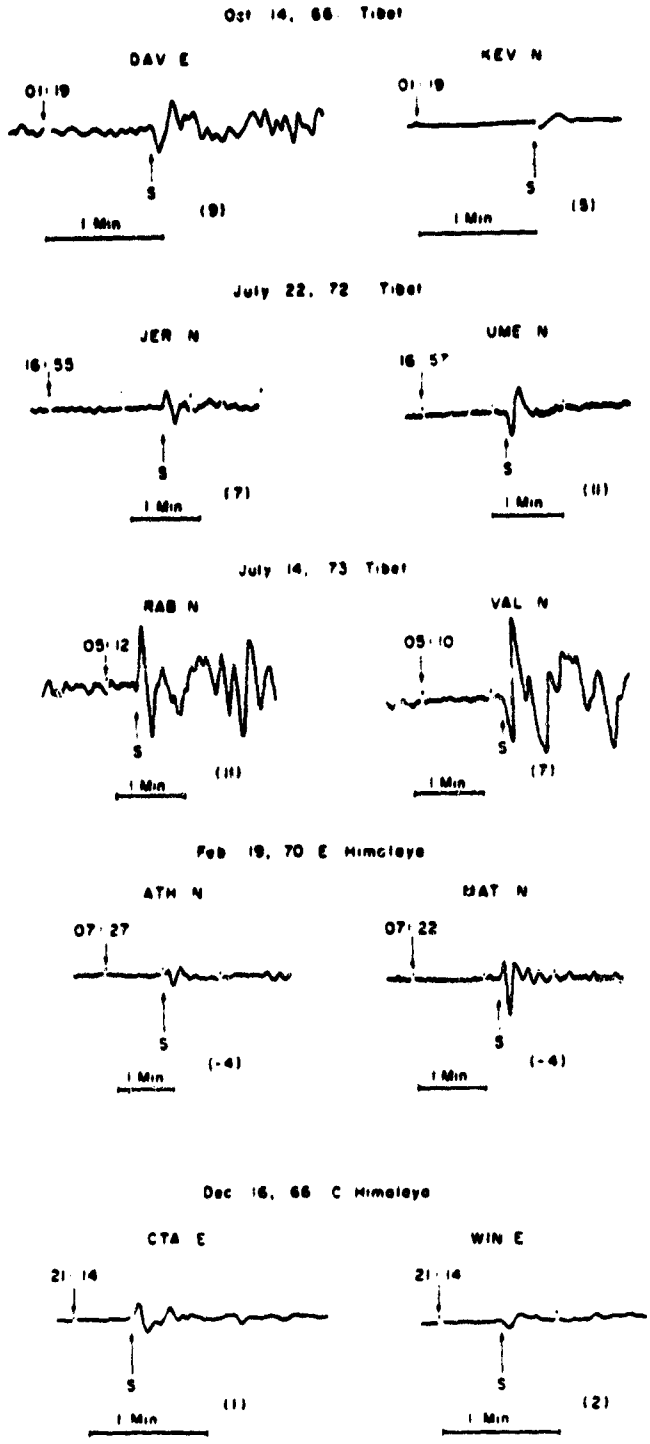
Oct 14, 66 Tibet
DAV E
01:19
S
(9)
1 Min
KEV N
01:19
S
(5)
1 Min
July 22, 72 Tibet
JER N
16:55
S
(7)
1 Min
UME N
16 57
S
(11)
1 Min
July 14, 73 Tibet
RAB N
05:12
S
(11)
1 Min
VAL N
05:10
S
(7)
1 Min
Feb 19, 70 E Himalaya
ATH N
07:27
S
(-4)
1 Min
BAT N
07:22
S
(-4)
1 Min
Dec 16, 66 C Himalaya
CTA E
21:14
S
(1)
1 Min
WIN E
21:14
S
(2)
1 Min

fig. 12

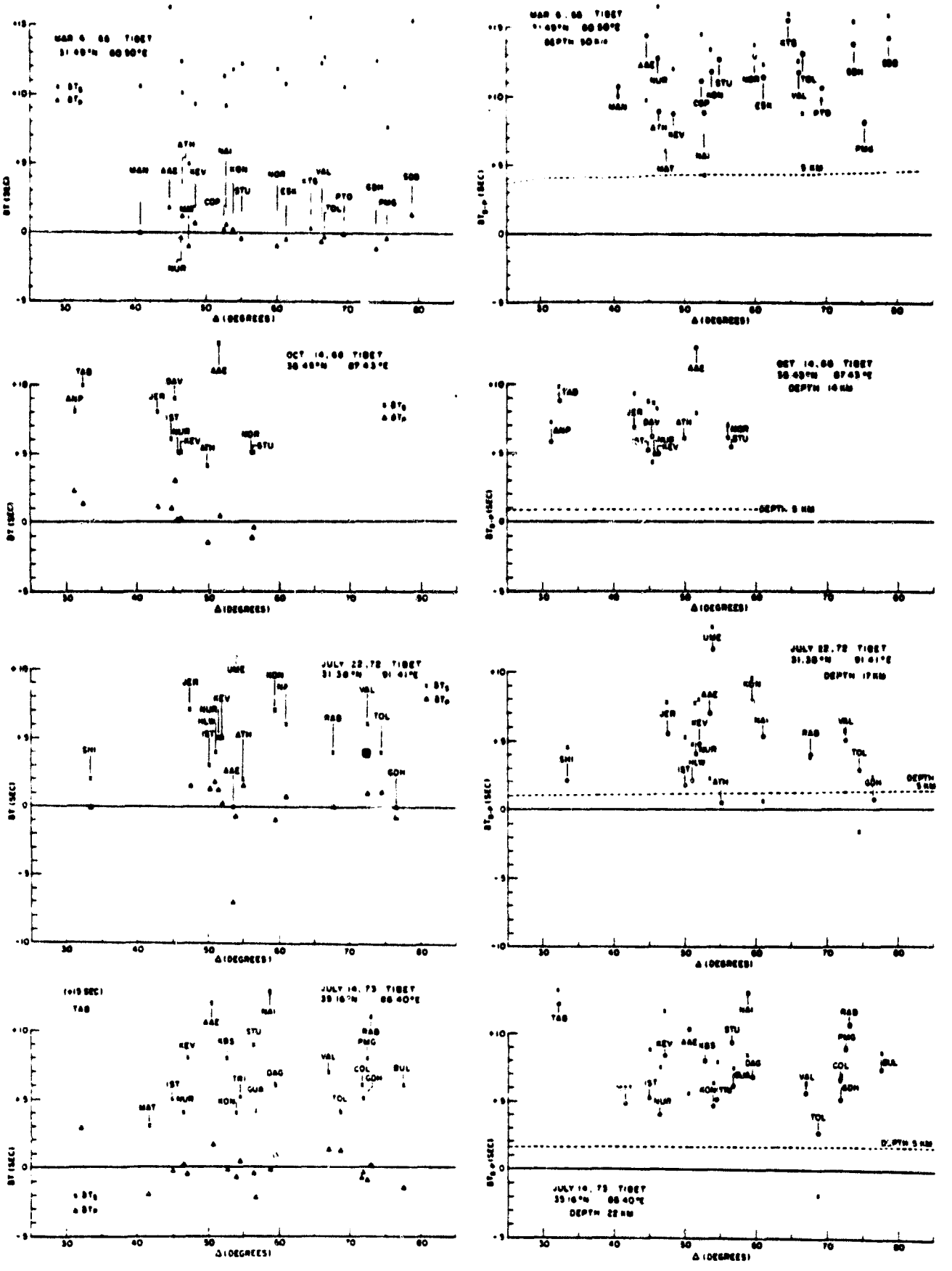

fig. 19

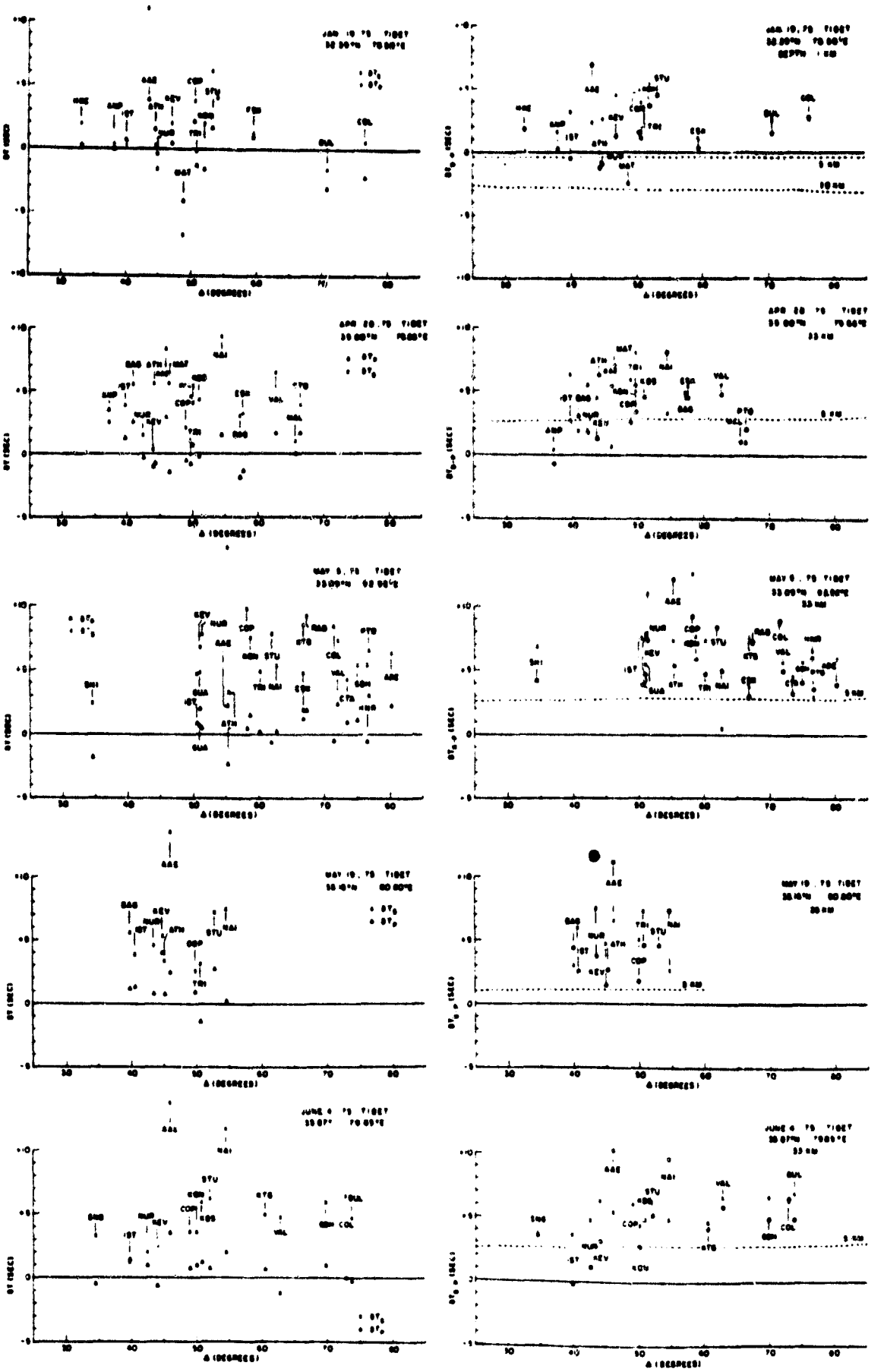

fig 19

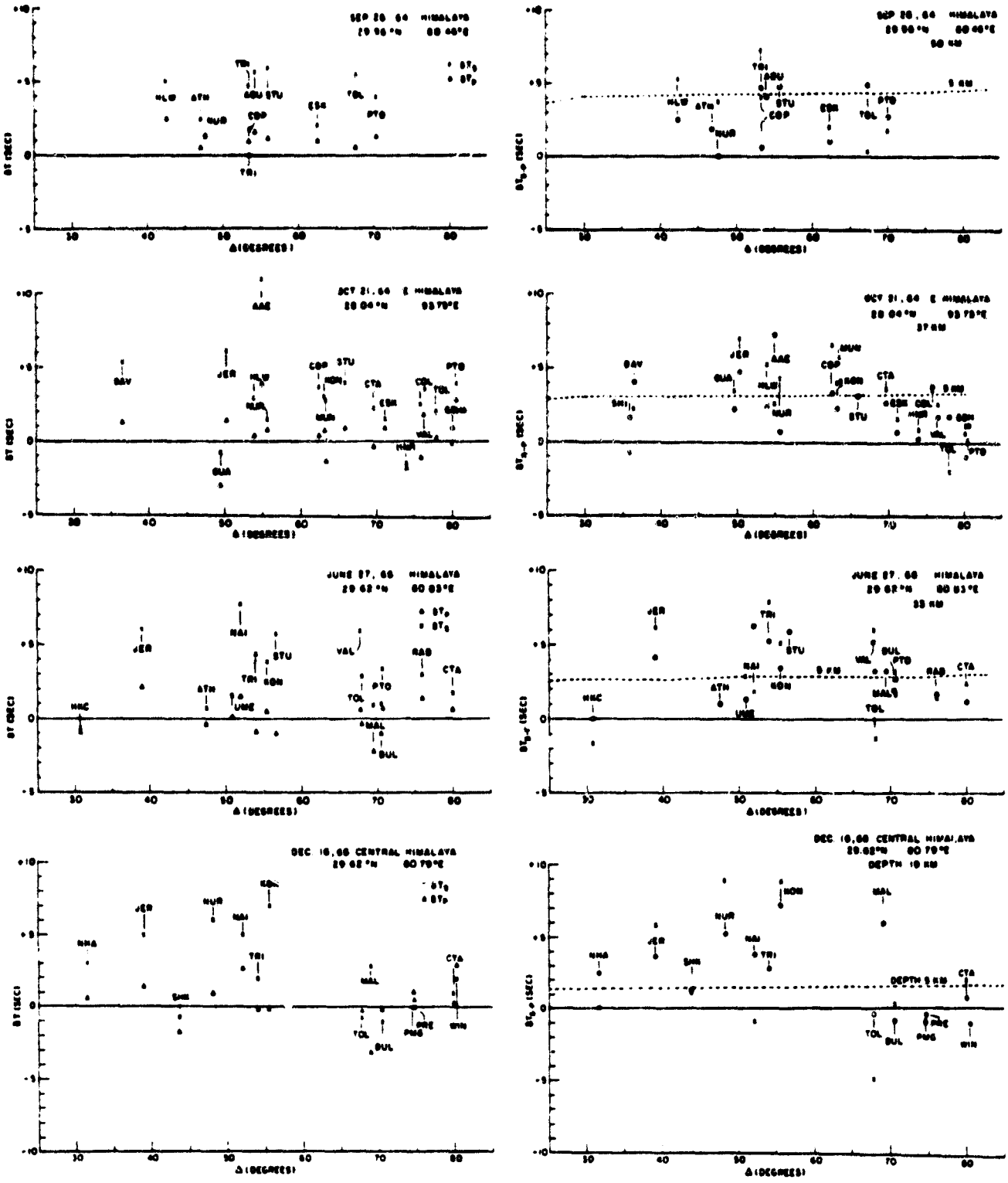
SEP 26, 64 HINDUKUSH
29.96°N 69.46°E
OCT 21, 64 E HINDUKUSH
29.04°N 93.79°E
JUNE 27, 66 HINDUKUSH
29.62°N 69.83°E
DEC 16, 66 CENTRAL HINDUKUSH
29.62°N 69.79°E
DEPTH 10 KM
ΔT (SEC)
Δ (DEGREES)

fig 20

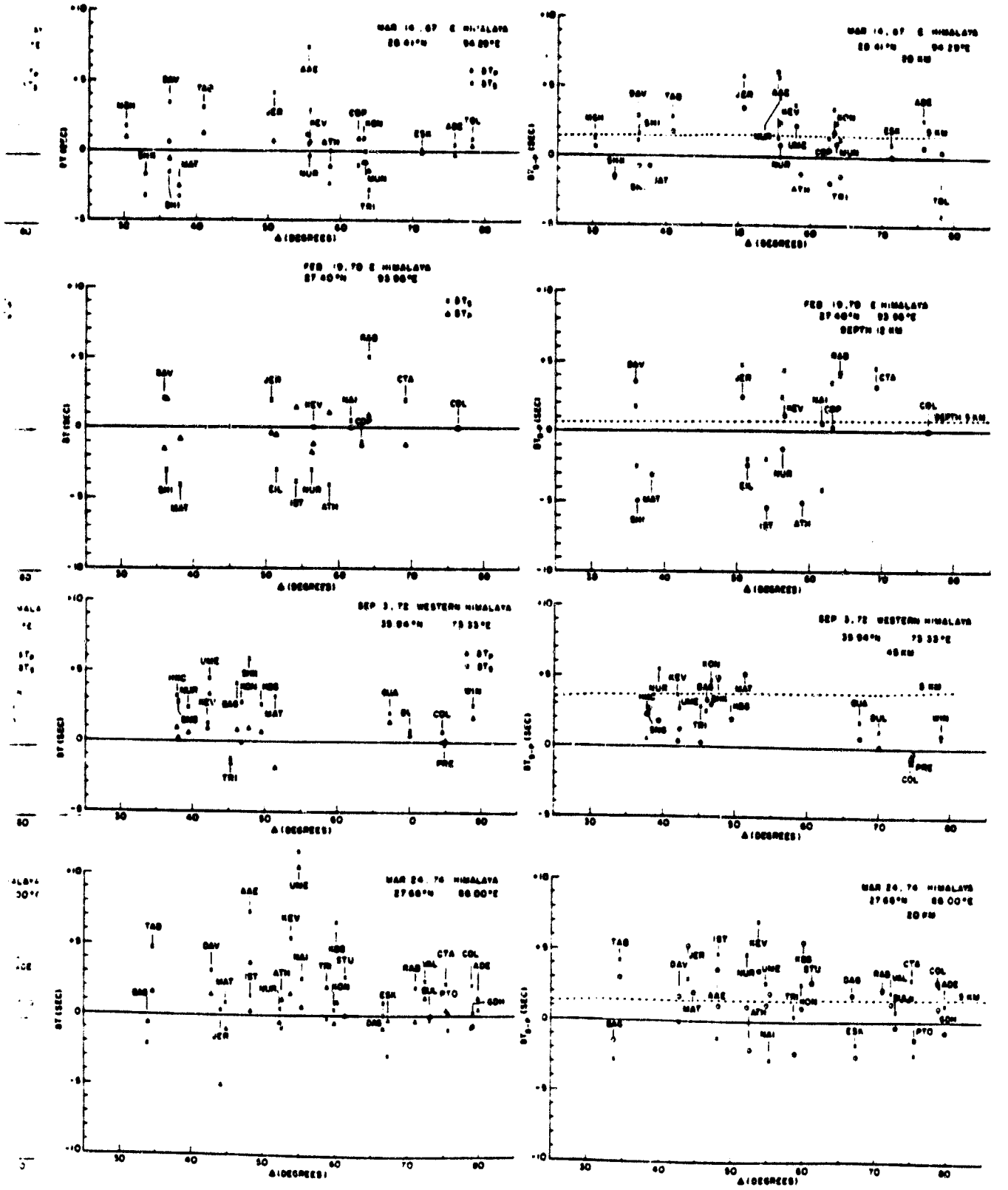

ORIGINAL PAGE IS
OF POOR QUALITY

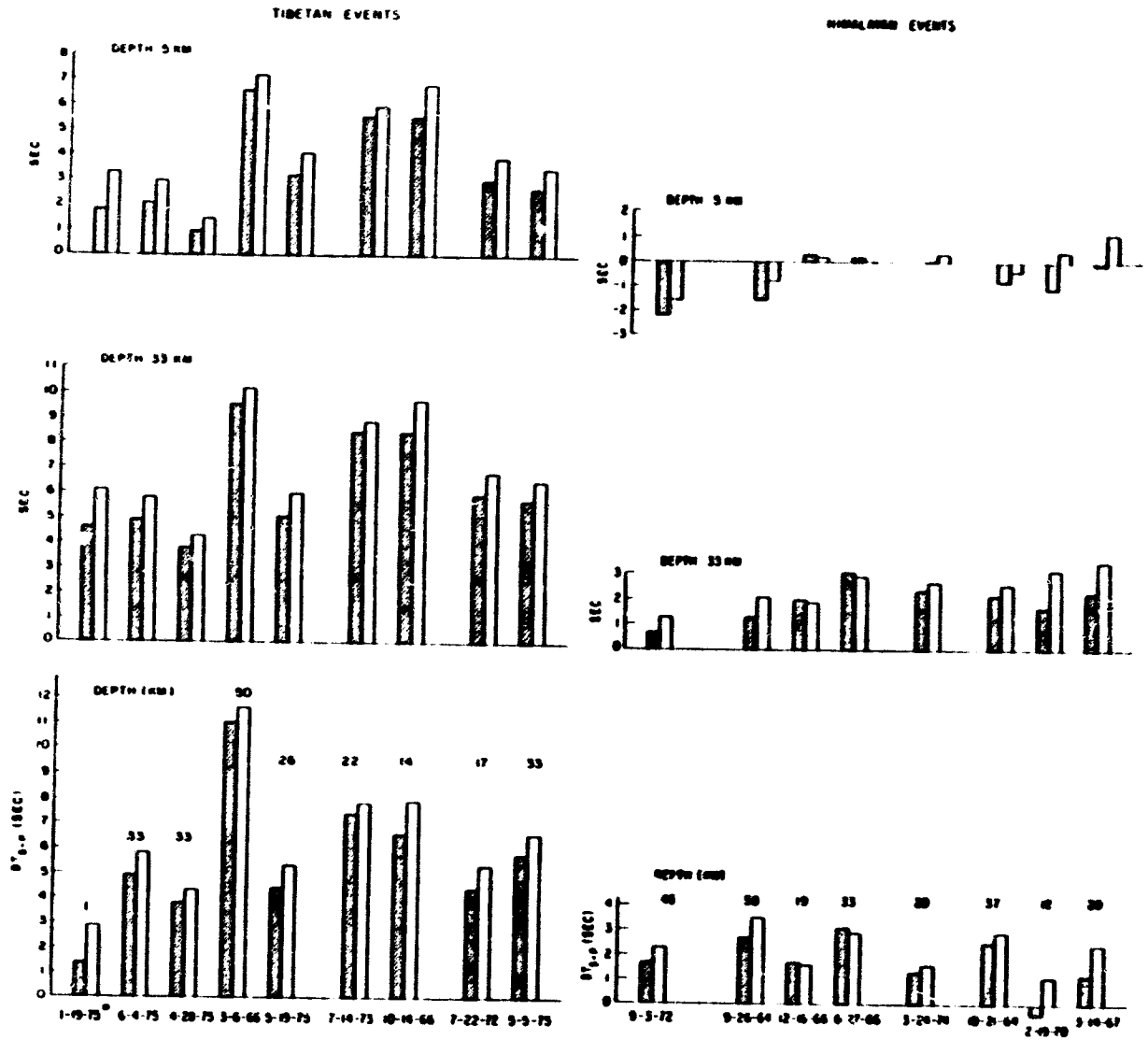
TIBETAN EVENTS
DEPTH 5 KM
SEC
DEPTH 33 KM
DEPTH (KM)
33
33
90
26
22
14
17
33
1-19-73*
6-4-73
6-28-73
8-6-66
9-19-73
7-14-73
10-14-66
7-22-72
9-9-73
9-3-72
9-26-64
3-20-70
2-19-70

fig-21

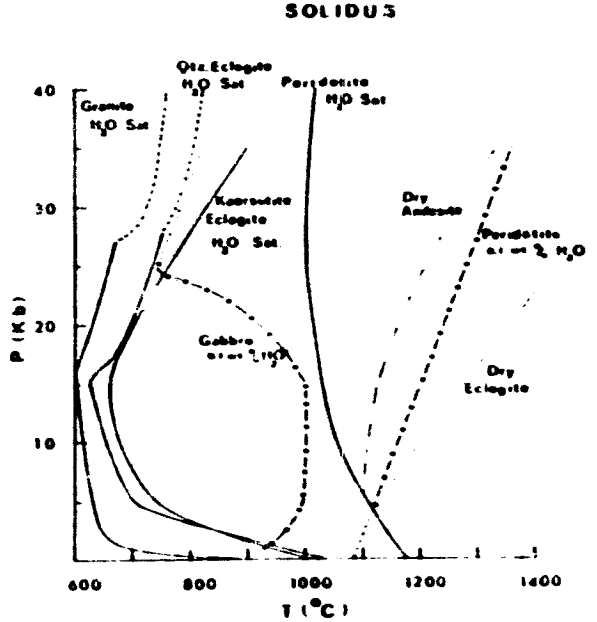
SOLIDUS
Qtz. Eclogite
H_2O Sat
Peridotite
H_2O Sat
Granite
H_2O Sat
Kaersutite
Eclogite
H_2O Sat
Dry
Andesite
Peridotite
Gabbro
Dry
Eclogite
P (Kb)
40
30
20
10
600
800
1000
1200
1400
T (°C)

fig. 22

THE UPPERMOST MANTLE P WAVE VELOCITIES BENEATH TURKEY AND IRAN

Chu-Yung Chen, Wang-Ping Chen, and Peter Molnar

Dept. of Earth and Planetary Sciences, M.I.T., Cambridge, MA 02139

Abstract. The uppermost mantle P wave velocities beneath Turkey and Iran were estimated by applying the conventional travel time-distance relation method to arrival times of well located earthquakes recorded at a few stations. The average uppermost mantle P wave velocity under Turkey is estimated from two stations of the World Wide Standardized Seismograph Network (WWSSN), Istanbul and Tabriz. The data are consistent with a crust of uniform, but poorly determined, thickness and an uppermost mantle P wave velocity of 7.73 ± 0.08 km/s. This velocity is very similar to that for the Aegean Sea and suggests that its structure could be closely related to that beneath Turkey. For Iran, the results calculated from travel times to three WWSSN stations, Meshed, Shiraz and Tabriz, can be explained by a crust dipping toward the south-southeast at about 1° with an uppermost mantle P wave velocity of 8.0 ± 0.1 km/s. If the crustal thickness were 34 km in the north it would reach about 49 km in the south. Based on these uppermost mantle velocities, the temperature at Moho beneath Turkey is probably close to the melting temperature of peridotite but that beneath Iran is probably lower.

Introduction

The mantle velocity and crustal thickness are important constraints in understanding the tectonic evolution of an area. There are no reliable rules for predicting these informations from surface elevation or other geophysical data. The Basin and Range province and Tibet are good examples. Both areas have high surface elevation, active faulting and recent volcanics [e.g., Molnar and Tapponnier, 1978; Priestley and Brune, 1978]. With only surface wave dispersion, the Basin and Range province was once thought to have a thick crust [Ewing and Press, 1959]. Later, detailed refraction and additional surface wave dispersion studies of crustal and upper mantle structure in this area [e.g., Prodehl, 1970; Priestley and Brune, 1978] showed that the crust is thin (≤30 km) and that the uppermost mantle P wave velocity is low (7.8 km/s). Tibet, on the other hand, has a thick crust (70 km) and the uppermost mantle P wave velocity (8.1 ± 0.1 km/s) is almost the same as that of stable shield areas [Chen and Molnar, 1980].

Turkey and Iran lie north of or within the continental collision zone between Africa and Eurasia. The surface features in these two areas are very similar to the Basin and Range province and Tibetan region. They all have active faulting, recent volcanics and high surface elevations. In this study, the uppermost mantle P wave (P_n) velocities under Turkey and Iran are investigated and compared with the two provinces mentioned above. Based on these estimated P_n velocities, we place constraints on the uppermost mantle temperatures beneath Turkey and Iran.

Data Analysis

We examined all the earthquakes that occurred in Turkey and Iran during January 1964 to January 1976 and for which travel times were reported at Istanbul (IST), Tabriz (TAB), Meshed (MSH), and Shiraz (SHI). The locations of the earthquakes used in this study are shown in Fig. 1. The origin times, focal depths, epicentral distances and arrival times were taken from the Bulletin of the International Seismological Centre. The earthquakes were sorted based on the following criteria: (1) we used only events for which more than 25 measurements of P wave arrival times were used in the determination of the earthquake hypocenter and origin time; (2) events with reported standard deviations of the origin times greater than two seconds were excluded; (3) only events with focal depths less than 35 km were included. Initially we considered earthquakes with reported focal depths as large as 60 km, but data scattered very much for those deeper than 35 km. So, only events with focal depth less than 35 km were included; (4) only events with epicentral distances between 4° and 11.5° were included. Within the epicentral distance range of approximately 3° to 12°, the first arrival on the seismogram for a given event is the P_n phase. The exact range depends on the crustal thickness and the P wave velocities in the crust and mantle. Epicentral distances between 3° and 12° were examined for all stations, and almost all the travel time residuals with respect to the mean are negative between 3° and 4°. Also, events occurred in Iran with epicentral distances as large as 14° reported at Tabriz were included and the travel time residuals were all negative for events with distances greater than 11.5°. The events with distances less than 4° or greater than 11.5° were excluded for all the four stations to maintain a single distance range for the entire data set.

After applying these criteria, there were still some events with large residuals (greater than two seconds) at one or more stations. Upon checking the seismograms we found that for most of these cases the arrivals were emergent. The signal to noise ratios are very low and the arrival times could not be determined precisely for many of them. These events were excluded from this study. Some of the reported arrival times were revised after checking the seismograms. Fig. 2 shows an example.

For a particular earthquake i, let T_i be the travel time calculated from the observed arrival

Paper number 9L1498.
0094-8276/80/009L-1498$01.00

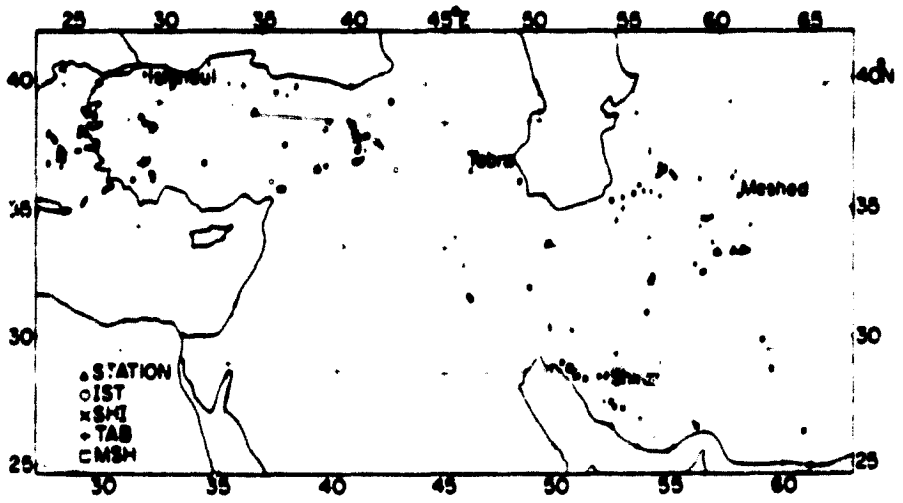

Fig. 1. Map showing epicenters of earthquakes used for estimating the uppermost mantle P wave velocities beneath Turkey and Iran. Circles, crosses, pluses, and squares show earthquakes with arrival times reported at Istanbul, Shiraz, Tabriz, and Meshed, respectively.

TABLE 1. Summary of P_n Velocity, Intercept Time and Crustal Thickness Under Turkey and Iran Estimated From Arrival Times to Different Stations.

Region	Recorded station	Numbers of earthquakes included	Before depth-correction P_n(km/s)	Before depth-correction a_p(sec)	After depth-correction P_n(km/s)	After depth-correction a_p(sec)	crustal thickness
Turkey	IST	37	7.60±0.06	1.3±5.3	7.70±0.04	1.7±3.1	25±32 km
	TAB	23	7.81±0.08	5.8±4.9	7.76±0.06	3.9±3.9	36±36 km
Iran	MSH	39	8.02±0.09	7.4±8.4	8.02±0.07	6.5±6.6	47±48 km
	SHI	50	8.19±0.15	8.7±13.1	8.14±0.10	7.1±8.4	49±55 km
	TAB	62	7.79±0.06	3.6±7.7	7.85±0.05	3.6±6.7	34±49 km

time and the reported origin time obtained by using many stations in a global scale. We define the travel time residual ϵ_i by

$$\epsilon_i = T_i - (\frac{\Delta_i}{V_p} + a_p).$$

The uppermost mantle P wave velocity (V_p) and intercept time (a_p) were calculated by least-square fitting of travel times (T_i) versus distance (Δ_i) and minimizing the sum of the squares of the travel time residuals ($\Sigma\epsilon_i^2$) for earthquakes reported at the particular station.

For comparison, both depth-corrected travel times and travel times without depth corrections were calculated. For the depth-corrected case all of the origin times and therefore the travel times, were normalized to a focal depth of 33 km, which is the mean reported focal depth. To do this, we assumed a crustal P wave velocity of 6.1 km/s and mantle P wave velocity of 8.0 km/s. Different assumptions of the velocity structure will not give large differences in the results. For example, assuming P_n of 7.7 km/s or 8.4 km/s for an earthquake occurring at the earth's surface makes only 0.4 seconds difference in the calculated depth-corrected origin time.

Results

We used 37 earthquakes reported at IST and 23 earthquakes reported at TAB to calculate the average uppermost mantle P wave velocity beneath Turkey. For the cases without a depth-correction, the P_n velocities are estimated to be 7.60 ± 0.06 km/s and 7.81 ± 0.08 km/s from data reported by IST and TAB, respectively (Table 1). For the depth-corrected cases, the P_n velocities are estimated to be 7.70 ± 0.04 km/s and 7.76 ± 0.06 km/s respectively. From Fig. 3 and the calculated standard deviations, we can see that the scatter of the data is reduced by the depth-correction as one may expect theoretically. Figs. 3d and 3e show that if the velocity were forced to be 8.0 km/s, the data should define a line with a slope parallel to the dashed lines. From these figures, we can see that a high P_n velocity will not fit the data well unless there is some distance-dependent systematic error in determining the epicenters, focal depths and origin times.

The large standard deviations in the intercept times (Table 1), make it difficult to estimate the crustal thickness from these values. Since

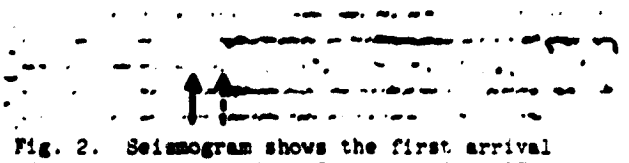

Fig. 2. Seismogram shows the first arrival of an event reported at Istanbul, Aug. 17, 1971 ($04^{hr}29^{min}33.4^{sec}$; 37.07°N, 36.77°E). Dashed arrow indicates the reported reading ($04^{hr}31^{min}21.8^{sec}$), and solid arrow indicates the first arrival ($04^{hr}31^{min}19^{sec}$) that we used.

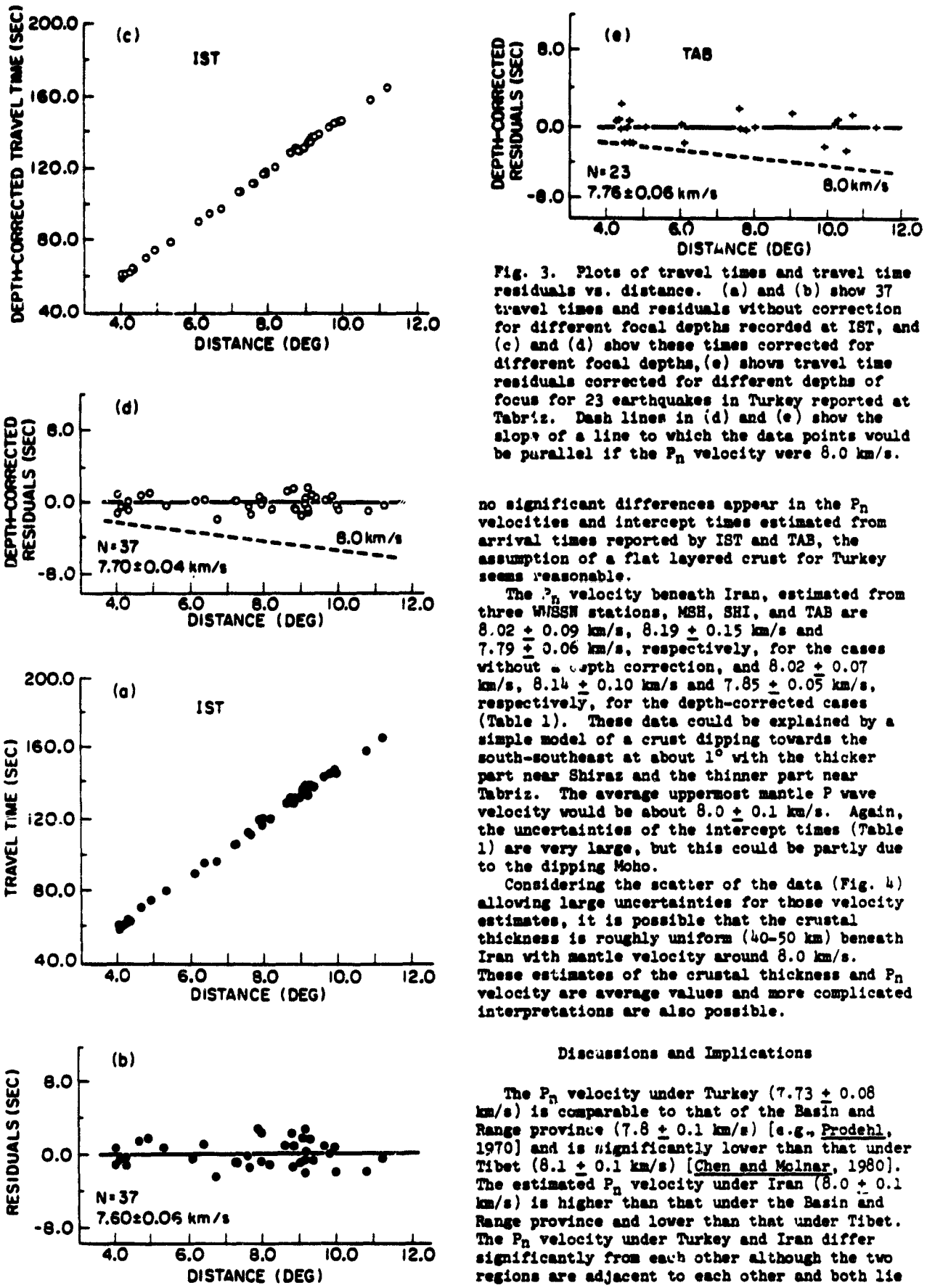

Fig. 3. Plots of travel times and travel time residuals vs. distance. (a) and (b) show 37 travel times and residuals without correction for different focal depths recorded at IST, and (c) and (d) show these times corrected for different focal depths, (e) shows travel time residuals corrected for different depths of focus for 23 earthquakes in Turkey reported at Tabriz. Dash lines in (d) and (e) show the slope of a line to which the data points would be parallel if the P_n velocity were 8.0 km/s.

no significant differences appear in the P_n velocities and intercept times estimated from arrival times reported by IST and TAB, the assumption of a flat layered crust for Turkey seems reasonable.

The P_n velocity beneath Iran, estimated from three WWSSN stations, MSH, SHI, and TAB are 8.02 ± 0.09 km/s, 8.19 ± 0.15 km/s and 7.79 ± 0.06 km/s, respectively, for the cases without a depth correction, and 8.02 ± 0.07 km/s, 8.14 ± 0.10 km/s and 7.85 ± 0.05 km/s, respectively, for the depth-corrected cases (Table 1). These data could be explained by a simple model of a crust dipping towards the south-southeast at about 1° with the thicker part near Shiraz and the thinner part near Tabriz. The average uppermost mantle P wave velocity would be about 8.0 ± 0.1 km/s. Again, the uncertainties of the intercept times (Table 1) are very large, but this could be partly due to the dipping Moho.

Considering the scatter of the data (Fig. 4) allowing large uncertainties for those velocity estimates, it is possible that the crustal thickness is roughly uniform (40-50 km) beneath Iran with mantle velocity around 8.0 km/s. These estimates of the crustal thickness and P_n velocity are average values and more complicated interpretations are also possible.

Discussions and Implications

The P_n velocity under Turkey (7.73 ± 0.08 km/s) is comparable to that of the Basin and Range province (7.8 ± 0.1 km/s) [e.g., Prodehl, 1970] and is significantly lower than that under Tibet (8.1 ± 0.1 km/s) [Chen and Molnar, 1980]. The estimated P_n velocity under Iran (8.0 ± 0.1 km/s) is higher than that under the Basin and Range province and lower than that under Tibet. The P_n velocity under Turkey and Iran differ significantly from each other although the two regions are adjacent to each other and both lie

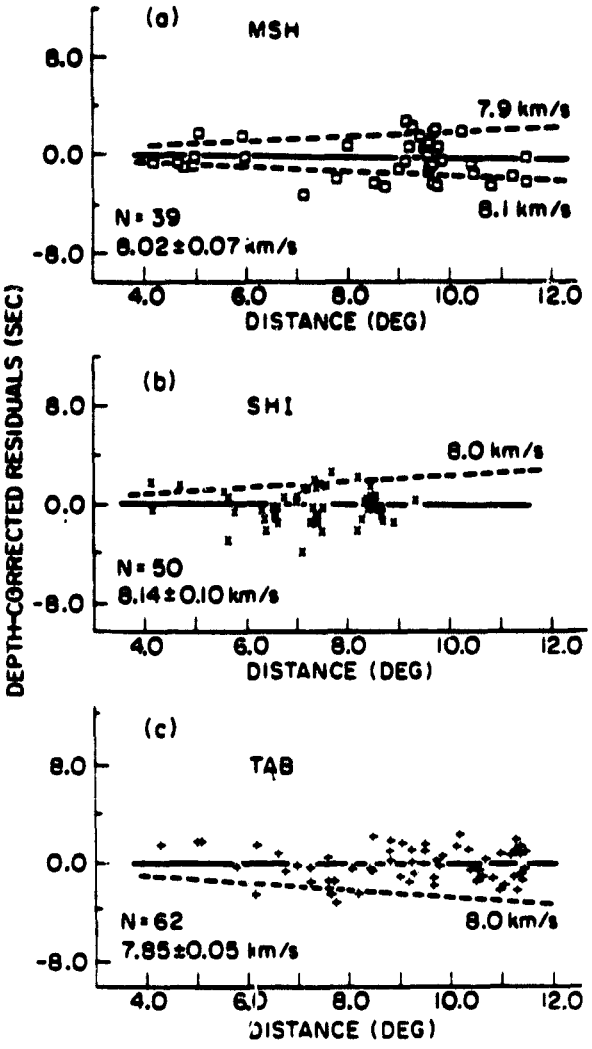

Fig. 4. Plots of travel time residuals corrected for different focal depths vs. distance for earthquakes in Iran reported at Meshed (a), Shiraz (b), and Tabriz (c), respectively. Layout as in Figure 3.

north of or within the continental collision zone extended between Afro-Arabia and Eurasia. The P_n velocity beneath Turkey is very similar to that beneath the Aegean Sea (7.6-7.8 km/s) from deep seismic sounding [Makris, 1978]. This suggests that the mantle structure beneath the Aegean Sea could be closely related to that beneath Turkey [McKenzie, 1978].

With these velocities, we can place rough constraints on the temperatures at the Moho beneath Iran and Turkey. Assuming that the temperature and pressure dependencies of the P wave velocity in the uppermost mantle are similar to those of the olivine, then a pressure decrease of 10 kb or temperature increase of 250°C will reduce the P_n velocity by 0.1 km/s [e.g., Birch, 1969].

The temperature in the uppermost mantle beneath the shield areas estimated from heat flow data [Sclater et al., 1979] is about 400° ± 100°C. Taking this temperature and average shield P_n velocity of 8.1 km/s and average shield crustal thickness of 35 km, with P_n velocity of 8.0 ± 0.1 km/s, the uppermost mantle temperature beneath Iran would be 650° ± 350°C if the crustal thickness were 35 km, or 800° ± 350°C if the crustal thickness were 55 km. With P_n velocity of 7.73 ± 0.08 km/s and crustal thickness of 25-35 km, however, the temperature in the uppermost mantle beneath Turkey would be calculated to be 1400° ± 300°C. This temperature would be high enough to melt peridotite at uppermost mantle pressures. Near the melting temperature, the assumed linear relationship between the P_n velocity and temperature at constant pressure is likely to be invalid [Goetze, 1977]. Indeed, the actual temperature in the uppermost mantle beneath Turkey is surely lower than 1400°C, but probably is above the peridotite solidus. This estimate is consistent with the recent basaltic volcanism in Turkey and implies that the basaltic liquid originates in the uppermost mantle.

Acknowledgements. This research was supported by NASA grant NCC 5-8 (NSG 5260).

References

Birch, F., Density and composition of the upper mantle: First approximation as an olivine layer, in The Earth's Crust and Upper Mantle, P.J. Hart, (ed.), Geophys. Monograph 13, Amer. Geophys. Un., 18-36, 1969.

Chen, W. P. & P. Molnar, Constraints on the seismic wave velocity structure beneath the Tibetan plateau and their tectonic implications, submitted to J. Geophys. Res., 1980.

Ewing, M. and F. Press, Determination of crustal structure from phase velocity of Rayleigh waves, III The United States, Bull. Geol. Soc. Am., 70, 229-244, 1959.

Goetze, C., A brief summary of our present day understanding of the effect of volatiles and partial melt on the mechanical properties of the upper mantle, in High-pressure Research Applications in Geophysics, Academic Press, Inc., 3-23 , 1977.

McKenzie, D., Active tectonics of the Alpine-Himalayan belt: the Aegean Sea and surrounding regions, Geophys. J. Roy. Astr. Soc., 55, 217-254, 1978.

Makris, J., The crust and upper mantle of the Aegean Region from deep seismic soundings, Tectonophysics, 46, 269-284, 1978.

Molnar, P. and P. Tapponnier, Active tectonics of Tibet, J. Geophys. Res., 83, 5361-5375, 1978.

Priestley, K. and J. Brune, Surface waves and the structure of the Great Basin of Nevada and Western Utah, J. Geophys. Res., 83, 2265-2272, 1978.

Prodehl, C., Seismic refraction study of crustal structure in the Western United States, Geol. Soc. Amer. Bull., 81, 2629-2646, 1970.

Sclater, J. G., C. Jaupart, and D. Galson, The heat flow through oceans and continents, submitted to Rev. Geophys. Space Phys., 1979.

(Received September 18, 1979; accepted October 10, 1979.)

Tectonophysics, 60 (1979) 43—60

THE EVOLUTION OF THERMAL STRUCTURES BENEATH A SUBDUCTION ZONE

ALBERT T. HSUI and M. NAFI TOKSÖZ

Department of Earth and Planetary Sciences, Massachusetts Institute of Technology, Cambridge, Mass. 02139 (U.S.A.)

ABSTRACT

Hsui, A.T. and Toksöz, M.N., 1979. The evolution of thermal structures beneath a subduction zone. Tectonophysics, 60: 43—60.

Thermal models of the subducting lithosphere and the surrounding mantle are investigated simultaneously. In the model, slab subduction is treated as a kinematic process. Subduction angle and subduction velocity are prescribed. The mantle is permitted to respond dynamically to subduction. Mantle flow is driven by both mechanical shearing and thermal buoyancy. Finite difference numerical techniques are utilized to model the subduction process. Results indicate that the descending lithosphere and the induced flow in the wedge area dictate the thermal structure beneath plate convergent regions. The temperature of a slab is found to be insensitive to the mantle condition prior to slab subduction. Viscous shear heating effects within the dynamic mantle are found to be important in maintaining a high temperature region immediately beneath the inter-arc basins.

INTRODUCTION

The subduction regions are among the most complex tectonic provinces on Earth. Many processes taking place in these regions have not yet been understood satisfactorily (Uyeda, 1977). The thermal regime of the region is undoubtedly a piece of important information which enable us to better understand many geophysical and geological processes taking place in the converging plate boundaries. The thermal structure of a downgoing slab has been studied by a number of investigators (McKenzie, 1969; Turcotte and Oxburgh, 1969; Minear and Toksöz, 1970a, b; Hasebe et al., 1970; Toksöz et al., 1971, 1973; Turcotte and Schubert, 1971, 1973; Griggs, 1972; Schubert et al., 1975). These models were calculated without taking into account the effects of the dynamic mantle. Using these slab models as boundary conditions, the thermal structure of the surrounding mantle has also been investigated (Andrews and Sleep, 1974; Jones, 1977; Toksöz and Bird, 1977; Toksöz and Hsui, 1978). These two families of models generally ignored the continuous interaction between the slab and the mantle. In this

paper we construct a more realistic model beneath the subduction region by calculating the temperature within a slab and that of the surrounding dynamic mantle simultaneously.

Another problem we investigate is why the temperature above the slab is relatively high. High temperature in the wedge area is inferred by the high surface heat flow measurements (for a good summary, see Watanabe et al., 1977) and the high attenuation of seismic waves (both P and S) in these regions (Oliver and Isacks, 1967; Molnar and Oliver, 1969; Utsu, 1971; Barazangi and Isacks, 1971; Barazangi et al., 1975). Beneath the converging plate boundaries, the mantle is cooled by the subducting oceanic lithosphere. If the subduction rate is 10 cm/yr and the plate thickness is 100 km, a volume of about 10^4 km^3 of cold lithospheric material will be injected into the mantle per million years per km width of the subduction zone. Taking an average temperature difference of about 500°C between the lithosphere and the mantle beneath, it follows that the same volume of the mantle will be replaced by the 500-degree cooler lithospheric material in a million years. Within the same period of time, radiogenic heat production (assuming that heat production is at equilibrium with the surface heat fluxes and the heat sources are uniformly distributed within the mantle) is only able to increase the temperature by about 1°C. Then, what is the mechanism that keeps the wedge region from cooling? This paper looks at this problem in some detail.

MODEL DESCRIPTION

Ideally, it would be desirable to treat the subduction and mantle-convection problem as a closed, continuous and dynamic system with appropriate mantle properties. However, this presents extreme difficulties, both analytically and numerically. In this paper, the thermal structure of the subduction region is studied by modeling a slab subducting *kinematically* into a deformable mantle. In other words, the subduction velocity and the angle of subduction are prescribed. Instead of posing the problem as a continuously evolving system, we calculate the thermal regime at discrete time intervals. The basic approach is very similar in philosophy to that described by Minear and Toksöz (1970a, b) such that we are in essence studying the heating of a discretely descending slab by the dynamic mantle. The slab is moved downward by one grid space at a time. Calculations are then carried out to determine how the slab is heated up by the surrounding mantle within the time interval necessary for the slab to reach that depth. The convection and the thermal regime of the mantle are also determined simultaneously. Our model is an extension of most of the published slab models.

The model consists of a 100 km thick conducting layer (lithosphere) lying on top of a convecting 700 km thick upper mantle. Calculations for our model are separated into two parts. One part is to calculate the thermal structure within the lithosphere and the subducting slab, while the other is to compute the thermal regime within the dynamic mantle that lies beneath

the conducting lithosphere and surrounds the descending slab. The two calculations interact with each other through their common boundaries. When the slab subducts, its temperature is translated to a new position, the mantle is then allowed to respond to this disturbance within the time interval necessary for the slab to travel to its new position. The effects of slab shearing, thermal buoyancy, and adiabatic compression are incorporated in the calculations. Computations of the slab temperatures and the mantle temperatures are self-consistent at each time step through the matching of boundary conditions. An explicit, forward time march, finite difference numerical scheme is used to simulate the thermal consequences of the subduction process. Details of the mathematical formulation, the numerical approximations, and the computational procedures are very similar to those given in Toksöz and Hsui (1978).

Boundary conditions. The boundary conditions are difficult to specify since neither the mantle flow structure nor the nature of the bottom of the mantle convection layer is known with great confidence. However, if the vertical boundaries are sufficiently far away from the subduction region, the effects of the vertical boundary conditions will be small on the thermal structure of the slab and its immediate environment. In our models, the horizontal dimension spans about 2800 km. The location of subduction at the surface is chosen at least 800 km away from either end, which is more than the vertical length scale of the convecting mantle. After the slab has been translated to its new position, the thermomechanical structure of the mantle is calculated assuming the vertical boundaries are shear stress free, mass exchange free, and thermally insulated. At the top of the dynamic mantle, a prescribed velocity equivalent to the slab velocity is imposed on the oceanic side of the slab while a no-slip condition is imposed on the continental side. The outward heat flux from the mantle at this boundary is determined from the thermal structure of the overlying lithosphere. At the bottom, a prescribed inward heat flux is imposed and a no-slip mechanical condition is used. We also calculated models with a shear-stress-free bottom boundary condition. The thermal structures are not very different from those of a no-slip bottom boundary condition. This is in agreement with the conclusions of Hsui (1978) that thermal convection solutions are not sensitive to the mechanical boundary conditions at the bottom. The most difficult boundary condition to choose is probably that at the tip of the slab. In this paper, we choose a no flow condition at this boundary, so that it is consistent with the no mass flux condition imposed on the two vertical boundaries. Mass flow induced by the tip strongly depends on the shape of the tip. Thus the choice of this boundary condition may introduce different effects locally. Richter (1977) studied the effects of tip push and found that it could be significant. However the effects of variable mantle viscosity and different boundary geometries are not investigated. Furthermore, when one introduces a mass flux at the tip of a slab (mass input) one also has to specify the distriburion of outward

mass flux at other boundaries. Different distributions of outward mass flux will affect the solutions in their own way. Therefore, this alternative will also introduce its own uncertainties to the problem. It should be stated that the "tip" problem goes away when the slab penetrates the bottom.

Initial conditions. Since the problem is cast as a transient problem, initial conditions are required to complete the mathematical formulation. Again, neither the mechanical nor the thermal conditions within the mantle prior to slab subduction are known. Therefore, we choose to treat the initial condition as a parameter and study the sensitivity of the thermal regime of a slab and its immediate environment to the initial conditions chosen. Even though very little data exists which can be used to constrain the initial conditions, we assume that the mantle was probably at equilibrium with the heat inputs to the system prior to slab subduction. Therefore, a steady state solution for the dynamic mantle in the absence of a slab is obtained and used as the initial condition for the mantle. Generally, any solution of thermal convection will yield upwelling as well as downgoing currents. In order to study the local effects upon a subducting slab, subduction has been initiated at three different locations: above the upwelling current, above the downgoing current, and above the center of a convection cell. With these three modes of subduction, the regional effects of different initial conditions on slab temperatures can be analyzed.

Heat sources. The mantle not only deforms in response to the mechanical shearing of a descending slab, but motions can also occur within the mantle due to thermal buoyancy generated by internal heat release. Therefore, the specification of heat source strength within the system is necessary. However, the distributions of U, Th, and K heat sources within the Earth are not known in detail. In this paper, the strength of the heat production rate is estimated by assuming that it is at equilibrium with the surface heat flux. The average heat flow values from the ocean floor vary from 50—80 erg/cm^2-s (Sclater et al., 1979). We further assume that the lithosphere and the lower mantle each contribute about 25% of this heat budget while the rest is generated internally within the upper mantle. (i.e., The heat production rate within the lithosphere is about $1.5 \cdot 10^{-6}$ erg/cm^3-s. The heat production rate within the upper mantle is $4.5 \cdot 10^{-7}$ erg/cm^3-s and the heat flux from the lower mantle is about 13.5 erg/cm^2-s.) The choice of heat source distribution does not appear to affect the results very much since the time duration is short for the radiogenic isotopes to generate significant heating. For the same reason, the heat production rate is taken to be constant in time in our calculation.

Viscosity. The relationship between the rate of deformation and the shear stress within the mantle remains an obscure subject mainly because of the absence of relevant laboratory data at the high pressures and low strain rates

appropriate to the mantle conditions. However, numerical experiments (Turcotte et al., 1973; Parmentier et al., 1976) indicate that the thermal structure of a convective system is very sensitive to the choice of a constant or a strongly temperature and pressure dependent viscosity, while relatively insensitive to the assumption of a newtonian or a non-newtonian behavior. Therefore, for mathematical simplicity, our model assumes a newtonian medium with a strongly temperature and pressure dependent viscosity. The viscosity ν is given by: $\nu = A \exp(BT_m/T)$, where T_m is the absolute melting temperature which is taken from the 0.1% hydrous pyrolite mantle model of Ringwood (1975). T is the local absolute temperature. A and B are two constants so adjusted that the resultant viscosities are in agreement with those determined from the study of glacial uplift data (Cathles, 1975; Peltier and Andrews, 1976; Peltier, 1976). In this paper, $A = 1.8 \cdot 10^{16}$ cm^2/s and $B = 9.0$, are used.

Phase boundaries. The upper mantle phase changes (basalt-eclogite, pyrolite-garnet, olivine-spinel, spinel-post spinel, etc.) could affect both the convection and thermal regime by density changes and heats of reaction. The effects of phase transitions on mantle dynamics have been studied by Schubert and Turcotte (1971) and Schubert et al. (1975). Their results indicate that the olivine-spinel phase transition is unlikely to inhibit mantle convection. Whether the spinel to post-spinel phase transition will inhibit mantle convection depends on the composition of the post-spinel phase. Since this transition is near the bottom of the convection zone, it will have little effect on this problem.

Besides the deformable mantle, phase transitions also take place within the descending slab. Their effects on the thermal regime of a subducting lithosphere have been studied by Toksöz et al. (1971). They concluded that the contribution of phase transitions to the heating of the interior of a downgoing slab is small when compared with other heating mechanisms such as conductive and convective heat transport, adiabatic heating and shear-strain heating. Based on the latent heat associated with these phase transitions (Verhoogen, 1965; Akimoto and Fujisawa, 1968; and Ringwood, 1970), the temperature increase due to phase changes within a slab is less than 50°C locally. Therefore, in this study, we neglect the effects of phase transitions.

THERMAL MODELS

The numerical models presented here are obtained using a 57 × 15 (50 km grid spacing) x-z grid system for the convecting mantle and a 10 × 10 km grid system for calculating the temperature within the slab. A test case using a 141 × 36 (20 km grid spacing) grid system for the mantle was carried out. Results are very similar to those obtained using the coarse grid. They differ by no more than 10 percent. Considering the uncertainties on many of the

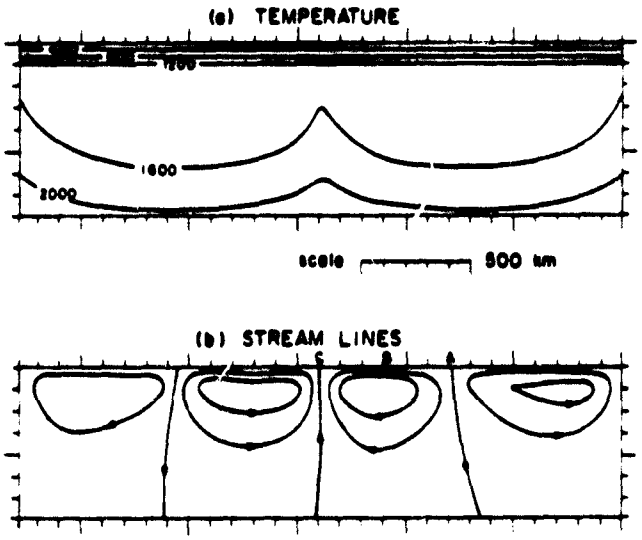

Fig. 1. The initial thermal and mechanical structure of the model calculations presented in this paper. a. Thermal profiles: the solid lines are the isotherms. The temperature in °C is given by the number associated with each isotherm. The shaded area represents the lithosphere. b. The stream lines plot: the maximum absolute stream function $|\psi|_{max}$ = 1.24. Stream lines plotted represent $|\psi|/|\psi|_{max}$ = 1/3, 2/3. Points *A*, *B*, and *C* indicate the locations where slab subduction is initiated.

parameters used in the models, the 50 km mantle grid system is adequate for calculating the gross thermal structure.

Figure 1 shows the initial conditions we used for the models. The diagram on the top is a plot of isotherms (constant temperature lines), while the one at the bottom is a plot of stream lines. In the isotherm plot, the lithosphere (shaded layer) is superimposed on top of the convecting mantle. However, in the stream line plot, the lithosphere has been removed. Points *A*, *B*, and *C* in the stream line plot indicate the locations where the initiation of subduction takes place for the three cases. In all the models, the slab subducts at an angle of 45° counterclockwise with respect to the horizon and at a speed of 8 cm/yr.

The following sequence of figures (Figs. 2—4) shows the thermal evolution history of a subducting slab and its surrounding mantle, for subduction initiating at point *B*. The shaded area represents the lithosphere and the subducting slab. As in Fig. 1, the top diagrams in this sequence are plots of isotherms while the bottom ones are plots of stream lines. Figure 2 shows the thermal and flow structure at 5.0 m.y. after the initiation of subduction. The thermal field has not been disturbed greatly except near the descending slab where the geotherms are being depressed downward. However, the flow field has been altered significantly. It is mainly because mechanical disturbances nor-

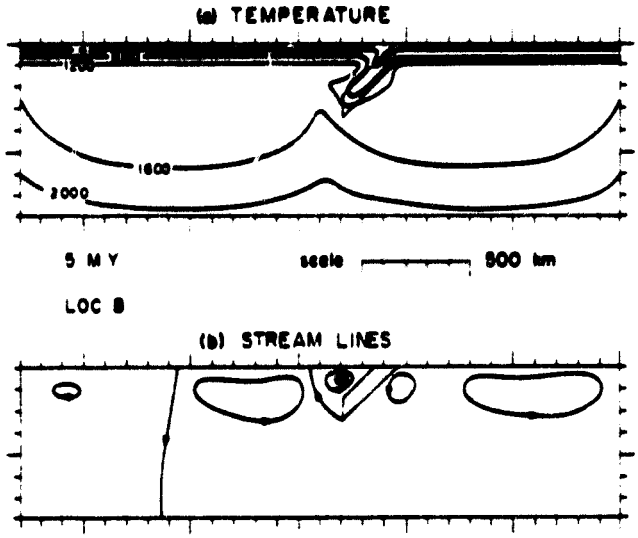

Fig. 2. Thermal-mechanical structure of the subduction zone at 5.0 m.y. after the initiation of slab subduction. $|\psi|_{max}$ = 2.31 and stream lines represent $|\psi|/|\psi|_{max}$ = 1/3, 2/3. Other notations are the same as in Fig. 1.

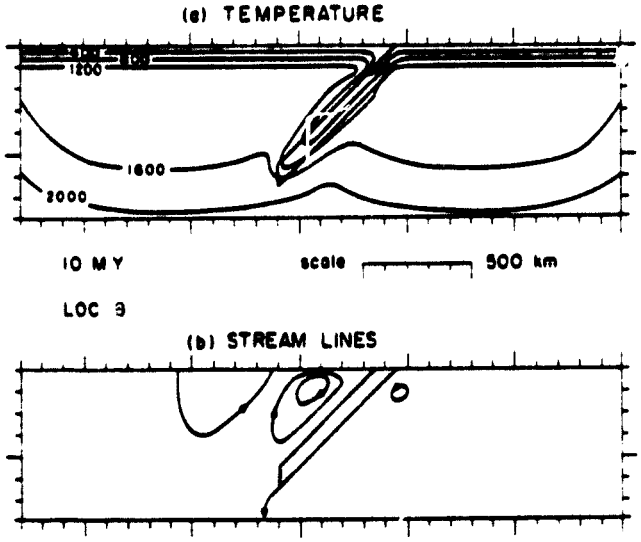

Fig. 3. Thermal-mechanical structure of the subduction zone at 10.0 m.y. after the initiation of slab subduction. $|\psi|_{max}$ = 4.00 and stream lines represent $|\psi|/|\psi|_{max}$ = 1/3, 2/3. Other notations are the same as in Fig. 1.

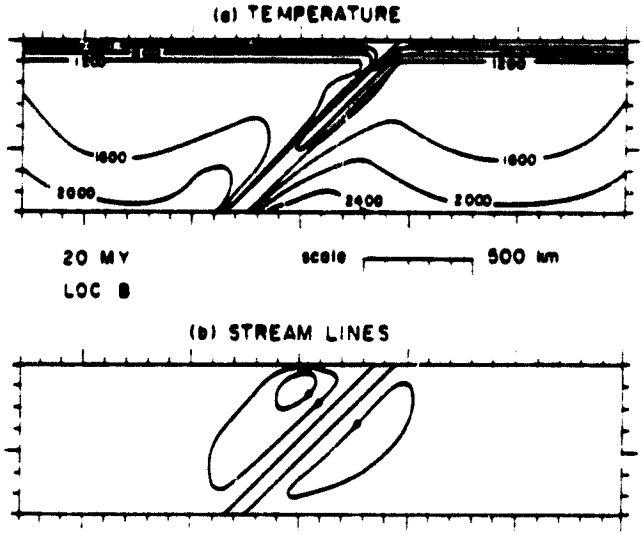

Fig. 4. Thermal-mechanical structure of the subduction zone at 20.0 m.y after the initiation of slab subduction. $|\psi|_{max} = 5.21$ and stream lines represent $|\psi|/|\psi|_{max} = 1/3, 2/3$. Other notations are the same as in Fig. 1.

mally propagate much faster than thermal disturbances. Therefore, the whole region feels the existence of the descending slab and adjusts the flow pattern accordingly even though the slab has penetrated only a small distance into the mantle. As to the thermal structure, the low temperature geotherms are being carried downward into the mantle by the slab. In essence, this demonstrates the cooling of the mantle by the subducting oceanic lithosphere. As the lithosphere subducts, induced convection currents are generated on both sides of the slab. Our models indicate that the induced flow above the slab (on the continental side and within the wedge area) has a higher intensity than that generated on the oceanic side of the slab.

This phenomenon is not observed if the flow is driven only by mechanical shearing (Richter, 1977; Tovish et al., 1978). Flow patterns driven by both mechanical shear and thermal buoyancy have been studied by Torrance et al. (1972). Even though the specific problems they studied are not related to the Earth's mantle, the physical consequences they derived are directly applicable to our study. In their study, Torrance et al. (1972) concluded that buoyancy can significantly change or even dominate the flow driven by shear only, resulting in higher flow velocities. This is in agreement with our results. Due to the combined effects of the large thermal gradient introduced by the descending slab, the strongly temperature dependent viscosity and a small flow cross section, the wedge flow turns out to be a strong current. Our cal-

culation shows that the flow velocity in the wedge can reach as high as two or three times the slab velocity.

At 10 m.y. (Fig. 3), the downgoing oceanic lithosphere has reached a depth of about 550 km. The mantle is cooled on both sides of the slab and the induced flow in the wedge area remains dominant. At 20 m.y. (Fig. 4), the slab has penetrated the bottom of our model. Even though the choice of a bottom at 800 km depth is somewhat arbitrary, comparison between Fig. 4 and Fig. 3 indicates that the thermal structure in the immediate environment of the slab above 300 km appears not to be affected significantly by the presence of this boundary. Since most of the geophysical and geological constraints lie above 300 km depth, the assumption of a bottom at 800 km in our models will not affect very much the near surface results derived from this study.

In the stream line plots of Figs. 1—4, stream functions are plotted at equal spacing for each diagram. Since the maximum absolute stream functions vary from one diagram to the other as indicated in the figure captions, the diminishing of stream lines does not imply the diminishing of the flow velocities. In fact, in all our calculations, flow velocities generally increase in time. Additionally, in our models, mantle viscosity varies from about 10^{19} poise immediately beneath the lithosphere to about 10^{23} poise near the bottom. The viscosity variation takes a very steep gradient near the surface and a relatively shallow gradient away from the asthenosphere. However, the viscosity structure adjacent to the slab is very complicated. It can no longer be expressed in terms of depth only. Since viscosity is directly related to temperature, a complex viscosity structure around a slab is a direct reflection of the complex thermal structure around a descending lithosphere.

Figures 5—7 represent the enlarged view of the isotherm plots presented in the previous evolution sequence (Figs. 2—4). Only regions immediately surrounding the slab are included. Again, the shaded area indicates the lithosphere and the descending slab. These diagrams provide better resolution of the thermal structure in the vicinity of a subducting lithosphere. In general, these diagrams demonstrate the cooling of the mantle as the low temperature isotherms are being carried downward by the descending slab. Since the mantle on both sides of the slab is being cooled by the subducting cold lithosphere, the slab appears thicker thermally except in the region between 100 and 200 km depth. In this region, the cold slab is unable to cool the mantle because a convective current is being induced in such a way that hot mantle material is continuously being pumped towards the vicinity of the slab at this depth. As a result, a bottle neck formation appears in the thermal structure of a slab subduction environment. Because of the coarse grid system used for numerical computation, our models cannot resolve whether this induced flow is able to maintain a temperature sufficiently high in the area immediately adjacent to the slab surface. This is important for the generation of magmas in island-arc volcanoes. Nevertheless, our models demonstrate that the

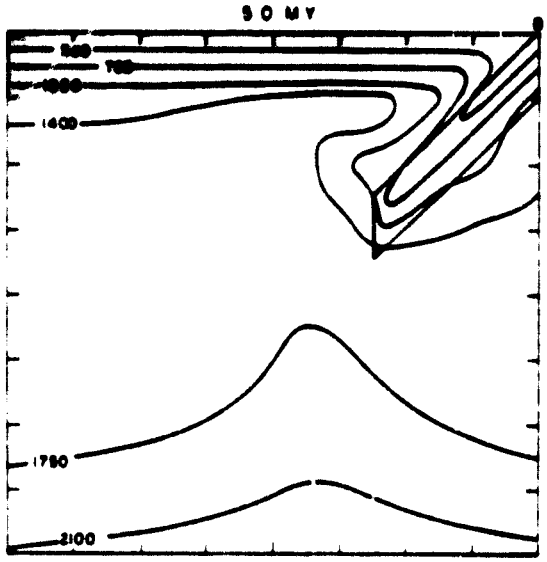

Fig. 5. Enlarged temperature plot of Fig. 2 in the vicinity of a descending slab.

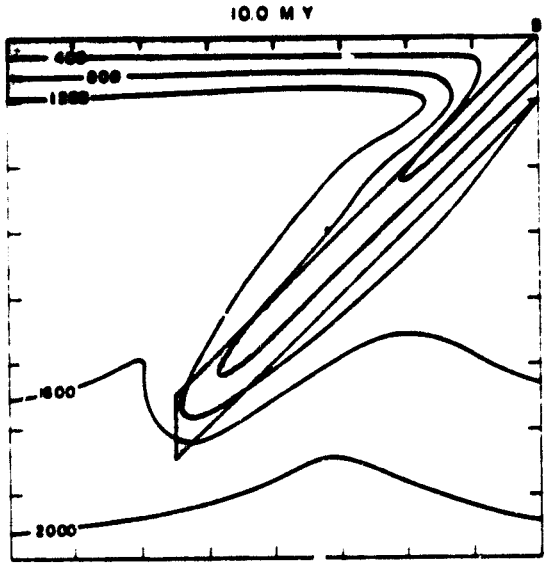

Fig. 6. Enlarged temperature plot of Fig. 3 in the vicinity of a descending slab.

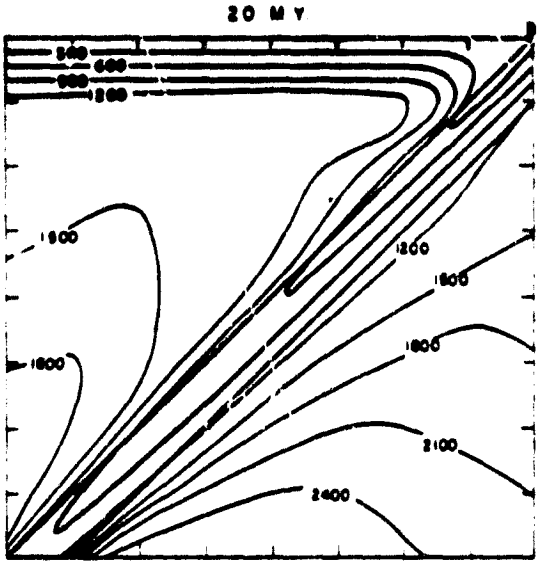

Fig. 7. Enlarged temperature plot of Fig. 4 in the vicinity of a descending slab.

asthenosphere above the slab will not be solidified by the descending cold lithosphere, simply because the induced current will continuously feed hot mantle material into the area.

The numerical results, showing that the temperature at the top of the wedge region remains relatively high, are consistent with the high attenuation of seismic waves and the high surface heat flow of the back arc region (see first section for references). It should be pointed out that all the models presented thus far are constructed with the shear heating effect incorporated not only between the slab and the mantle, but within the mantle flow as well. If the shear heating effect within the mantle flow is not included, the high temperature region at the top of the wedge area no longer exists as shown in Fig. 8. Therefore, viscous shear heating within the mantle flow appears to be important in maintaining a high temperature region beneath the back-arc basins. In fact, viscous shear heating can be as much as 2—3 times higher than the radiogenic heating. Therefore, the requirement of shear heating to maintain a high temperature wedge does not appear too surprising.

In order to see how much our slab temperature model differs from other models, a comparison is made (Fig. 9) between our model taken at 50 m.y. after the initiation of subduction and other published models (McKenzie, 1969; Toksöz et al., 1973; Turcotte and Schubert, 1973). The model by McKenzie (1969) represents the simplest slab model. It is analytic and considers only the effects of subduction and conduction. Therefore, it gives a lower

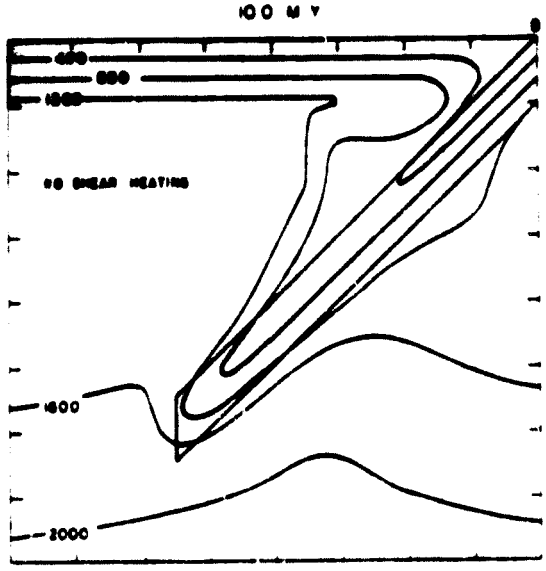

Fig. 8. Same as Fig. 6 except that viscous shear heating has not been incorporated in the model.

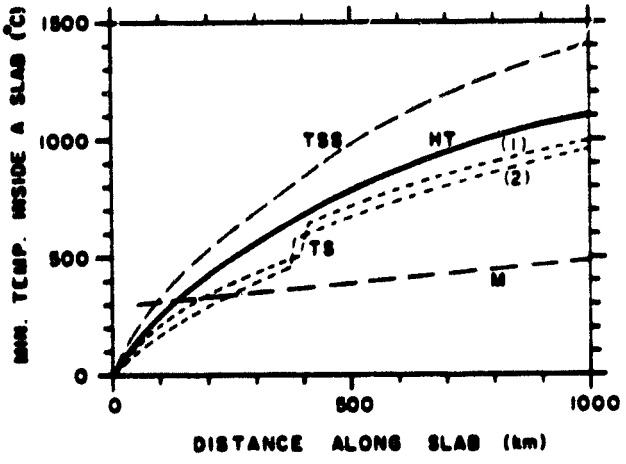

Fig. 9. Comparison of the minimum temperature within a slab as a function of distance along a slab among different slab models. *TSS* is from the model by Toksöz et al. (1973). *HT* is that of this paper. *TS* are those by Turcotte and Schubert (1973). Curve (*1*) is for constant shear stress while curve (*2*) is for constant frictional coefficient. *M* is that by McKenzie (1969).

bound of the thermal regime within a descending slab. Turcotte and Schubert (1973) have also determined the thermal structure within a slab using analytic methods. The effect of phase transition (olivine-spinel) has been incorporated. However, because of the absence of internal heat generation and utilizing a lower temperature at the base of the lithosphere, their models appear to be generally cooler than our models. Using finite-difference numerical techniques, Toksöz et al. (1973) have calculated the thermal structure within a slab using a convective mantle geotherm and including the effects of adiabatic compression, internal heat release, shear heating and phase changes. This model appears warmer than our present model. Since our model has not considered the effect of phase changes and because olivine-spinel phase change is an exothermic process, it can probably explain why our model is somewhat cooler. Meaningful comparison with the slab model of Toksöz et al. (1971) and Minear and Toksöz (1970a, b) cannot be made, however, because these models used conductive mantle geotherms that result in higher mantle temperatures. The present slab model is bracketed by other models as can be seen in Fig. 9, and it represents a good average temperature model for the subducting lithosphere.

OTHER MODELS

As pointed out previously, the condition of the mantle prior to slab subduction is subject to great uncertainty. Whether the thermal structure of the descending oceanic lithosphere and its environment are related to the initial mantle conditions is not immediately apparent. In order to investigate the relationship between the initial mantle conditions and the subsequent thermal evolution of a descending slab, we carried out models for which subduction has been initiated at different locations. Figures 10 and 11 show the thermal structure of a slab and its environment at two different times. In this case, subduction has been initiated at a point where downgoing mantle flow is taking place (point *A* in Fig. 1). Comparing Figs. 10 and 11 to Figs. 5 and 7, respectively, the thermal structures within the slab and within the wedge region are found to be very similar. When subduction is initiated at point *C* (in Fig. 1) where upwelling mantle flow is taking place, results (Figs. 12 and 13), again, are found to be similar to those where subduction is initiated either above a downgoing mantle flow or at the middle of a convection cell. From these results, it is evident that the thermal structure beneath the subduction area is controlled by the descending lithosphere and the resulting induced flow in the wedge area. The subduction process dominates whatever the mantle condition was prior to the descent of the cold oceanic lithosphere.

One of the most prominent features in plate convergent areas is the island arc volcanism. Unfortunately, due to the coarse grid system of the present models, a detailed study of island arc magma generation is not possible. Since both surface topography and gravity in these areas are dominated by

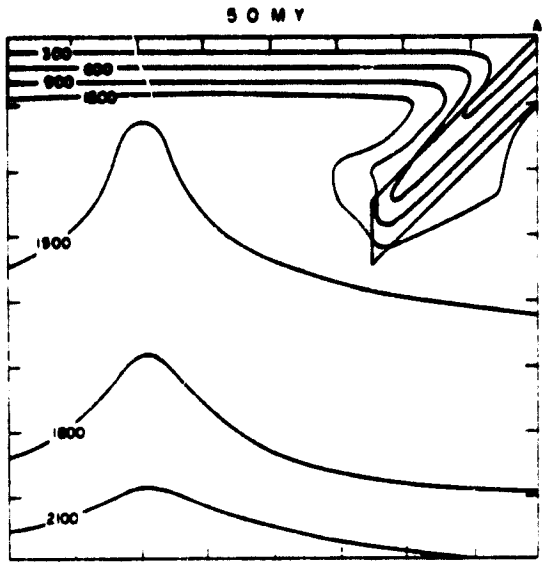

Fig. 10. Same as Fig. 5 except slab subduction is initiated at point *A* in Fig. 1.

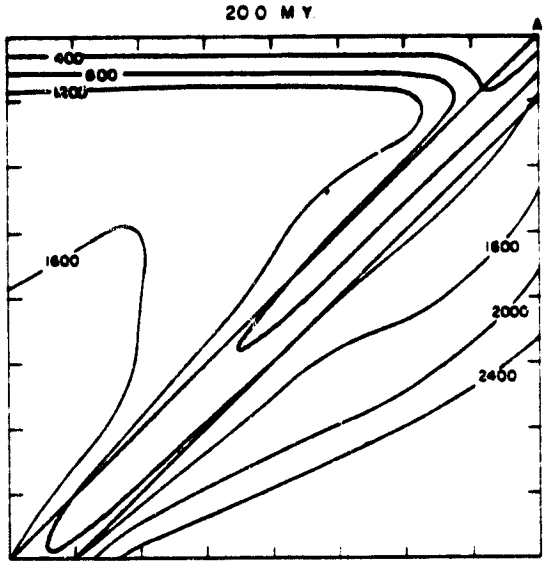

Fig. 11. Same as Fig. 7 except slab subduction is initiated at point *A* in Fig. 1.

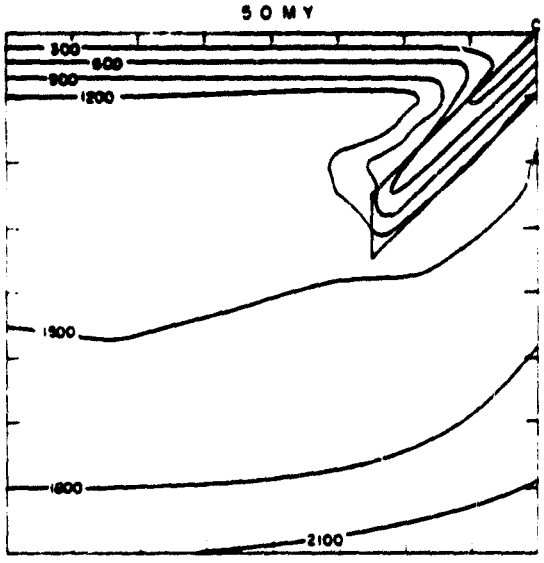

Fig. 12. Same as Fig. 5 except slab subduction is initiated at point *C* in Fig. 1.

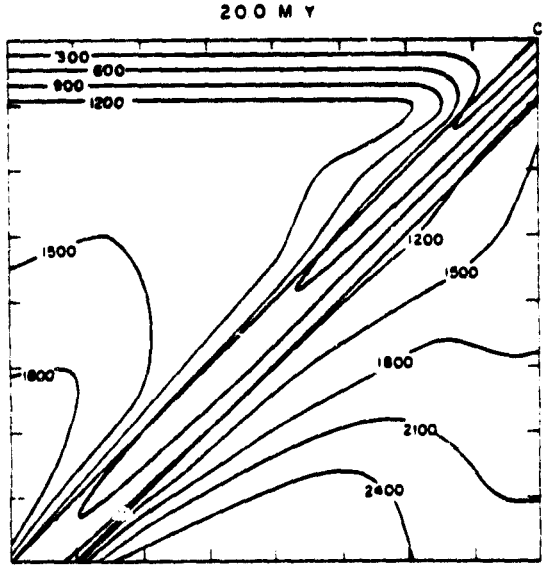

Fig. 13. Same as Fig. 7 except slab subduction is initiated at point *C* in Fig. 1.

island arcs, the failure to create island arc volcanoes prohibits a meaningful presentation of the surface topography and gravity anomalies predicted by the present models. However, the present model is able to confirm that the induced flow in the wedge area is indeed a strong convection flow, as discussed earlier. Even though by itself alone, the induced flow may not be sufficient to initiate back arc spreading (Toksöz and Hsui, 1978), it remains a plausible mechanism nevertheless.

SUMMARY

A thermal regime of a slab subducting into the mantle and its surrounding regions has been calculated taking into account the effect of convection with temperature, pressure dependent viscosity. Results indicate that the subduction process is primarily a cooling process. The cold descending lithosphere and the induced flow are the dominating factors in determining the thermal structure of the region at any given time. The temperature within the slab and in its immediate environment is insensitive to the mantle condition prior to slab subduction. In order to maintain a high temperature region beneath the inter-arc basins, as suggested by the high heat flow and the high attenuation of seismic waves, our model indicates that viscous shear heating within the mantle is probably an important factor. Without this, the wedge area is likely to be cooled rapidly by the descending cold lithosphere. Our model of the thermal structure of a downgoing slab is in good agreement with other slab models and it represents an average of these calculations. Finally, the induced flow within the wedge area is indeed a prominent feature of the subduction process. Its contribution to the mechanism of inter-arc spreading remains viable.

The primary purpose of the present model was to understand the thermal evolution of a slab and its surrounding mantle over a broad region. Because of the coarse grid system used for computational efficiency, detailed features such as magma generation and island arc volcanism cannot be studied. In order to have models which can explain detailed surface features, further work with improved computational techniques that yield finer resolutions must be carried out. In the mean time, the models presented here provide a better general understanding of the subduction process and they represent an advancement towards a fully dynamic and more realistic model of the subduction regions.

ACKNOWLEDGEMENTS

We would like to thank Prof. S. Uyeda and Dr. B. Hager for helpful discussions and suggestions. This research was supported by the National Science Foundation under Grant 76-12471EAR and by NASA under Grant NSG-7081 and Cooperative Agreement NCC5-8.

REFERENCES

Akimoto, S. and Fujisawa, H., 1968. Olivine-spinel solid solution equilibria in the system Mg_2SiO_4-Fe_2SiO_4. J. Geophys. Res., 73: 1467–1479.

Andrews, D.J. and Sleep, N.H., 1974. Numerical modelling of tectonic flow behind island arcs. Geophys. J. R. Astron. Soc., 38: 237–251.

Barazangi, M. and Isacks, B., 1971. Lateral variation of seismic wave attenuation in the upper mantle above the inclined earthquake zone of the Tonga Island Arc: Deep anomaly in the upper mantle. J. Geophys. Res., 76: 8493–8516.

Barazangi, M., Pennington, W. and Isacks, B., 1975. Global study of seismic wave attenuation in the upper mantle behind island arcs using P waves. J. Geophys. Res., 80: 1079–1092.

Cathles, L.M., III, 1975. The Viscosity of the Earth's Mantle. Princeton University Press, Princeton, N.J., pp. 155–196.

Griggs, D.T., 1972. The sinking lithosphere and the focal mechanism of deep earthquakes. In: Eugene C. Robertson (Editor), Nature of the Solid Earth. McGraw-Hill, New York, N.Y., 361–384.

Hasebe, K., Fujii, N. and Uyeda, S., 1970. Thermal processes under island arcs. Tectonophysics, 10: 335–355.

Hsui, A.T., 1978. Numerical simulation of finite amplitude thermal convection with large viscosity variation in axisymmetric spherical geometry: effect of mechanical boundary conditions. Tectonophysics, 50: 147–162.

Jones, G.M., 1977. Numerical model of a subduction zone. EOS, Trans. Am. Geophys. Union, 58: 499.

Lachenbruch, A.H., 1968. Preliminary geothermal model of the Sierra Nevada. J. Geophys. Res., 72: 6977–6989.

McKenzie, D.P., 1969. Speculations on the consequences and causes of plate motions, Geophys. J. R. Astron. Soc., 18: 1–32.

Minear, J.W. and Toksöz, M.N., 1970a. Thermal regime of a downgoing slab and new global tectonics. J. Geophys. Res., 75: 1397–1419.

Minear, J.W. and Toksöz, M.N., 1970b. Thermal regime of a downgoing slab. Tectonophysics, 10: 367–390.

Molnar, P. and Oliver, J., 1969. Lateral variations in attenuation in the upper mantle and discontinuities in the lithosphere. J. Geophys. Res., 74: 2648–2682.

Oliver, J. and Isacks, B., 1967. Deep earthquake zones, anomalous structures in the upper mantle and the lithosphere. J. Geophys. Res., 72: 4259–4275.

Parmentier, E.M., Turcotte, D.L. and Torrance, K.E., 1976. Studies of finite-amplitude non-Newtonian thermal convection with application to convection in the earth's mantle, J. Geophys. Res., 81: 1839–1846.

Peltier, W.R., 1976. Glacial-isostatic adjustment, II. The inverse problem. Geophys. J. R. Astron. Soc., 46: 669–705.

Peltier, W.R. and Andrews, J.T., 1976. Glacial-isostatic adjustment, I, The forward problem. Geophys. J. R. Astron. Soc., 46: 625–668.

Richter, F.M., 1977. On the driving mechanism of plate tectonics. Tectonophysics, 38: 61–88.

Ringwood, A.E., 1970. Phase tranformations and the constitution of the mantle. Phys. Earth Planet. Int., 3: 109–155.

Ringwood, A.E., 1975. Composition and Petrology of the Earth's Mantle. McGraw-Hill, New York, N.Y., pp. 146–156.

Schubert, G. and Turcotte, D.L., 1971. Phase changes and mantle convection. J. Geophys. Res., 76: 1424–1432.

Schubert, G., Yuen, D.A. and Turcotte, D.L., 1975. Role of phase transitions in a dynamic mantle. Geophys. J.R. Astron. Soc., 42: 705–735.

Sclater, J.G., Jaupart, C. and Galson, D., 1979. The heat flow through oceans and continents. Rev. Geophys. Space Phys. in press.
Toksöz, M.N. and Bird, P., 1977. Formation and evolution of marginal basins and continental plateaus. In: M. Talwani and W.C. Pitman III (Editors), Island Arcs, Deep Sea Trenches, and Back-Arc Basins. Maurice Ewing Ser., Vol. 1, Am. Geophys. Union, Washington, D.C., pp. 379–393.
Toksöz, M.N. and Hsui, A.T., 1978. Numerical studies of back-arc convection and the formation of marginal basins. Tectonophysics, 50: 177–196.
Toksöz, M.N., Minear, J.W. and Julian, B.R., (1971). Temperature field and geophysical effects of a downgoing slab. J. Geophys. Res., 76: 1113–1138.
Toksöz, M.N., Sleep, N.H. and Smith, A.T., 1973. Evolution of the downgoing lithosphere and the mechanisms of deep focus earthquakes. Geophys. J.R. Astron. Soc., 35: 285–310.
Torrance, K., Davis, R., Eike, K., Gill, P., Gutman, D., Hsui, A., Lyons, S. and Zien, H., 1972. Cavity flows driven by buoyancy and shear. J. Fluid Mech., 51: 221–231.
Tovish, A., Schubert, G. and Luyendyk, B.P., 1978. Mantle flow pressure and the angle of subduction: non-Newtonian corner flows. J. Geophys. Res., 83: 5892–5898.
Turcotte, D.L. and E.R. Oxburgh (1969) Convection in a mantle with variable physical properties. J. Geophys. Res., 74: 1458–1474.
Turcotte, D.L. and Schubert, G., 1971. Structure of the olivine-spinel phase boundary in the descending lithosphere. J. Geophys. Res., 76: 7980–7987.
Turcotte, D.L. and Schubert, G., 1973. Frictional heating of the descending lithosphere, J. Geophys. Res., 78: 5876–5886.
Turcotte, D.L., Torrance, K.E. and Hsui, A.T., 1973. Convection in the Earth's mantle. In: B.A. Bolt (Editor), Methods of Computational Physics, Vol. 13. Academic Press, New York, N.Y., pp. 431–453.
Utsu, T., 1971. Seismological evidence for anomalous structure of island arcs with special reference to the Japanese region. Rev. Geophys. Space Phys., 9: 839–889.
Uyeda, S., 1977. Some basic problems in the trench-arc back-arc systems. In: M. Talwani and W.C. Pitman III (Editors), Island Arcs, Deep Sea Trenches and Back-Arc Basins. Maurice Ewing Ser., Vol. 1, Am. Geophys. Union, Washington, D.C., pp.1–14.
Verhoogen, J., 1965. Phase changes and convection in the earth's mantle. Trans R. Soc. London, Ser. A, 258: 276–283.
Watanabe, T., Langseth, M. and Anderson, R.N., 1977. Heat flow in back arc basins of the western Pacific. In: M. Talwani and W.C. Pitman III (Editors), Island Arcs, Deep Sea Trenches and Back-Arc Basins. Maurice Ewing Ser., Vol. 1, Am. Geophys. Union, Washington, D.C., pp. 137–161.

Subduction of continental lithosphere: Some constraints and uncertainties

Peter Molnar, Dale Gray
Massachusetts Institute of Technology, Department of Earth and Planetary Sciences
Cambridge, Massachusetts 02139

ABSTRACT

Two effects that contribute to the subduction of continental lithosphere are the negative buoyancy of the relatively cold mantle part of continental lithosphere and the pull of a downgoing slab of oceanic lithosphere on continental lithosphere trailing behind it. The mantle part of the lithosphere could continuously subduct about 10 km of continental crust, if the upper and lower crust could be detached from one another. This estimate, however, could be in error by as much as a factor of three, given the range of plausible values for the requisite parameters. The second effect is more difficult to estimate because of our ignorance of what proportion of the gravitational force acting on the downgoing slab is transmitted to the surface lithosphere. For various assumptions, subducted oceanic lithosphere could be expected to pull a short (tens of kilometres) or long (hundreds of kilometres) length of intact continental crust into the asthenosphere. Although we favor subduction of only a short length of intact continental crust, we cannot prove that a large amount of crust is not subducted. These calculations are for continental margins that meet subduction zones flush. If continental crust can remain intact, peninsulas and microcontinents might be subducted completely.

INTRODUCTION

Because of its low density, continental crust has traditionally been assumed to be too light to be subducted. Even with the recognition of the important role of the lithosphere in subduction, earth scientists have assumed that the large thickness of continental crust provides too much buoyancy to continental lithosphere for it to be subducted (for example, Isacks and others, 1968; McKenzie, 1969). Yet geologic evidence indicates large-scale crustal shortening by thrust faulting in most mountain belts, particularly where continents collide. Consequently, some subduction of continental crust must take place, and in general, geologic evidence places only lower bounds on the amount of thrust displacement and therefore of subduction of lower crust. For instance, Gansser (1966) estimated that the total displacement on the major thrust faults in the Himalayas is at least 300 km, excluding displacement at the Indus suture zone, where thousands of kilometres of oceanic lithosphere probably were subducted. Powell and Conaghan (1973), however, proposed as much as 1,000 km of slip on one of the Himalayan faults, the Main Central thrust. In the Norwegian Caledonides, Gee (1975) inferred at least 500 km of shortening distributed on several faults. These estimates do not necessarily require a large amount of subduction of the entire intact continental crust to depths of hundreds of kilometres in the asthenosphere. In all cases the thrust faults are exposed only within the crust and could be interpreted as detachment surfaces between the upper and lower crust. Nevertheless, a substantial amount of crustal material must be subducted if only to depths of 70 km, to account for the observed shortening.

A basic question is, If the buoyancy of continental crust does inhibit subduction of continental lithosphere, then how much crust can be subducted before convergence is halted? Resolution of this question will probably require further detailed geologic mapping of thrust belts and may require new techniques. At present, however, we can examine limits on how much crust could be subducted given basic assumptions about the physical processes and requisite parameters involved.

Two phenomena contribute to the subduction of continental lithosphere. First, the mantle part of the lithosphere is cold and therefore dense enough that its negative buoyancy would pull the bottom part of the crust down if the top of the crust could be detached from it. Second, the gravitational body force acting on the subducted oceanic lithosphere may also exert force on the leading edge of a continent following the oceanic lithosphere into the subduction zone.

GEOLOGY, v. 7, p. 58-62, JANUARY 1979

GRAVITATIONAL STABILITY OF CONTINENTAL LITHOSPHERE

Oceanic lithosphere plunges into the asthenosphere because it is gravitationally unstable. It is colder and therefore more dense than the asthenosphere would be if brought adiabatically to the same depth (pressure). Although the crust is lighter than the mantle and buoys the lithosphere up, evidently oceanic crust is too thin to prevent subduction. The effects of these two buoyancy forces can be expressed simply as the difference between two terms, one for the buoyancy of the crust and the other for the negative buoyancy of the mantle part of the lithosphere (Fig. 1; McKenzie, 1969). For the crust, the buoyancy force per unit area inhibiting subduction is $(\rho_m - \rho_c)gh$, where ρ_m and ρ_c are the densities of the mantle and crust, g is gravitational acceleration, and h is the thickness of the crust. For the mantle part of the lithosphere, the difference in the density between material with temperature $T(z)$, and that with temperature $T_a(z)$, following the adiabatic gradient, is simply $\rho_m\alpha\,[T(z) - T_a(z)]$, where α is the coefficient of thermal expansion and z is the depth.

The temperature in the asthenosphere presumably closely follows the adiabatic gradient (≈0.5°/km). Because of the small amount of radioactivity in the mantle, the geotherm in the lithosphere is essentially linear (Fig. 1). If the base of the lithosphere is defined by a particular isotherm, T_a, then in oceanic lithosphere,

$$T(z) \cong \frac{T_a}{a}\,z, \tag{1}$$

where a is the thickness of the lithosphere. As the temperature in only the mantle part of the lithosphere is important, a more precise description of the temperature profile across it is

$$T(z) = (T_a - T_c)\,\frac{z - h}{z - a} + T_c, \tag{2}$$

where T_c is the temperature at the base of the crust and h is the depth of the Moho (Fig. 1). For continental lithosphere, equation 2 is slightly better than equation 1, because radioactivity in the continental crust makes an important contribution to the geotherm. The approximation of the geotherm in the mantle as two essentially straight lines—one due to conduction through the lithosphere and the other as an adiabat maintained by convection—is, of course, a simplification. More realistic geotherms, discussed by Parsons and McKenzie (1978), however, are not warranted here.

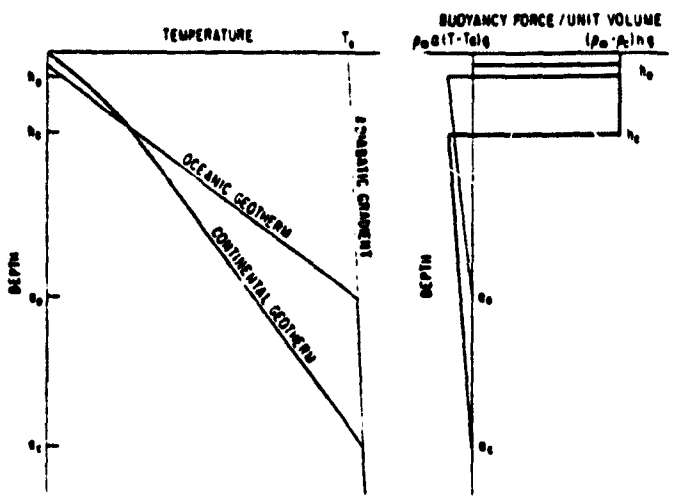

Figure 1. Geotherms and gravitational body forces. In lithosphere, heat is presumably conducted, and temperature gradient is essentially linear. Beneath lithosphere in asthenosphere, heat is convected, and gradient is adiabatic. Because lithosphere is colder than asthenosphere, it is more dense, and a body force due to gravity acts on it. This negative buoyancy force is opposed by buoyancy of crust, which is less dense than mantle. Integral over depth of curves on right, for oceanic and continental lithosphere, gives force per unit area acting on lithosphere.

The negative buoyancy force per unit area due to the low temperature of the lithosphere is $\rho_m\alpha g\int_h^a [T_a(z) - T(z)]dz$. This can be written directly by recalling the formula for a triangle (see Fig. 1): $\frac{1}{2}\rho_m\alpha g\,[T_a(h) - T(h)]\,(a - h)$. Because the adiabatic gradient is so small, $T_a(z)$ is nearly constant, so that $T_a(h) \cong T_a(a)$ = temperature of the asthenosphere.

For an instability to exist, the mantle part of the lithosphere must be heavier than the crust, or

$$(\rho_m - \rho_c)gh - \tfrac{1}{2}\rho_m\alpha g\,[T_a(a) - T(h)]\,(a - h) < 0. \tag{3}$$

Reasonable values for the various parameters are

$\rho_m - \rho_c = 3.35 - 2.8 = 0.55 \pm 0.1$ g/cm³
$\rho_m = 3.35 \pm 0.05$ g/cm³
$\alpha = 3 \pm 1 \times 10^{-5}$ °C⁻¹
$T_a = 1200 \pm 150$ °C
$T(h_c) = 500 \pm 100$ °C (for continents)
$a - h_c = 150 \pm 50$ km (for continents)
$a - h_o = 100$ km (for old ocean floor)

For oceanic lithosphere, where $h_o \ll a = 100$ km, $T(h_o) \cong 0$ °C, and $\rho_c = 2.9$ g/cm³, and instability exists when

$$h_o < \frac{\rho_m\alpha\,[T_a(a) - T(h_o)]\,(a - h_o)}{2(\rho_m - \rho_o)} < 13.4\text{ km}.$$

This condition is easily fulfilled in oceanic regions.

Expression 3 allows an estimate of what fraction of the lower continental crust, h_s, would be unstable if the upper part could be detached from it. Using the values given above, $h_s < 10$ km, approximately 30% of the crust. This estimate is very uncertain, however. Note that if we choose the extreme values given above, $h_s < 2$ km or $h_s < 29$ km. In the former case, a small fraction of the crust would be carried down, whereas in the latter nearly the entire continental lithosphere would be unstable! These extreme estimates arise from a conspiracy of extreme values for each of the parameters given above, and therefore both estimates are unlikely to apply in general. The calculations do show, however, that we cannot eliminate the possibility of subducting a large fraction of continental crust, if it could be detached from the upper part.

GRAVITATIONAL FORCE ACTING ON DOWNGOING SLAB OF OCEANIC LITHOSPHERE

If a continental mass is part of an oceanic plate being consumed at a subduction zone, gravitational body forces acting on the excess mass in the slab might be able to pull continental crust into the asthenosphere (see Fig. 2). Given plausible parameters that govern the various forces, we can place an upper bound on what length (d) of continental crust could be subducted. There are basically two questions here: What is the gravitational force acting on the slab? How much of it actually pulls on the part

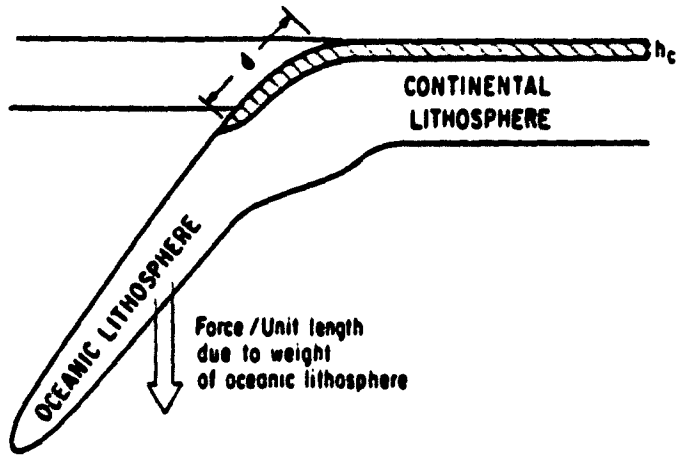

Figure 2. Gravitational force acting on oceanic lithosphere and pulling continental lithosphere into asthenosphere. Force is opposed by buoyancy of continental crust of length *d*.

of the lithosphere at the surface? Given our inability to answer the latter question, the uncertainty in the estimate of the amount of continental crust that can be subducted is very large. Nevertheless, we present the results for an assortment of assumptions and then state our prejudices about them.

The gravitational body force (per unit length of subduction zone) acting on the slab is due to the temperature of the slab being lower than that of the surrounding asthenosphere, and it can be estimated from calculations of the temperature in the slab, which depends primarily upon the subduction rate and the plate thickness (for example, McKenzie, 1969). Numerical calculations show that radioactivity in the oceanic crust and mantle does not contribute much to the temperature in the slab (Minear and Toksöz, 1970). The role of frictional heating remains controversial, but since we seek an upper bound on the amount of crust subducted, here we ignore its contributions both as a heat source and as a retarding force. Once a convergence stops, friction ceases to be either a heat source or a retarding force. We discuss phase changes below. The principal source that heats the slab is conduction from the surrounding asthenosphere (McKenzie, 1969; Minear and Toksöz, 1970).

McKenzie (1969) derived an analytic solution for the temperature in the slab and calculated the gravitational force acting on the slab due to its excess mass. This calculation is given in the Appendix 1, but it is extended to include different finite depths of penetration of the slab, and it is evaluated using more reasonable parameters for the plate thickness and surrounding temperatures than McKenzie used. From equation A5 and the parameters in the appendix, we obtain forces (per unit length along the arc) of 1.8×10^{16} dyne/cm for a slab extending to a depth of 350 km (that is, 500 km long and dipping at 45°) and of 3.2×10^{16} dyne/cm for a slab extending to a depth of 700 km (that is, 1,000 km long and dipping at 45°). For comparison, we note that Fitch (1977) integrated the force per unit length calculated by Schubert and others (1975) and obtained a maximum stress of 3.2 kb acting on a plate 100 km thick extending to 700 km depth, corresponding to a force per unit length of 3.2×10^{16} dyne/cm. A crude estimate of the excess mass calculated by Toksöz and others (1973) yields a similar value.

The principal sources of error in all of these calculations are the values of the thermal expansion, α, and the thicknesses of the plate, a_0 (because the force per unit length is proportional to a_0^2). Because of the uncertainties in the parameters inserted into these formulas, the resulting calculations could be in error by as much as a factor of two.

Another possible force is the excess mass in the slab due to the possible occurrence of the olivine-spinel phase change at a shallower depth in the slab than in the surrounding asthenosphere (for example, Richter, 1973; Schubert and others, 1975). Fitch (1977) integrated Schubert and others' calculation to obtain an additional force of 1.9×10^{16} dyne/km. There is a contrary suggestion, however, that the reaction is inhibited by its kinetics. In the cold central part of the slab the reaction would be so slow that this part of the slab would penetrate well below the equilibrium depth before the reaction would occur (Sung and Burns, 1976a, 1976b). In this case, it would not add a force pulling the slab down; instead, it would oppose subduction (Sung and Burns, 1976a, 1976b).

It is clear the the uncertainty in the gravitational body force acting on a downgoing slab is large. In addition, there are few data constraining how much of this force is transmitted to the surficial part of the lithosphere. Some excess mass in the slab will be supported by stress in the surrounding asthenosphere. For instance, the fault-plane solutions of deep earthquakes suggest that the excess mass of downgoing slabs below about 350 km does not pull the shallow part down (Isacks and Molnar, 1969, 1971). Perhaps the force acting only on the part shallower than 350 km pulls the surficial lithosphere. In fact, the possibility exists that the downgoing slabs do not exert a substantial force on the surface lithosphere. Kanamori (1971) suggested that at least some slabs break off at the trench and sink freely into the asthenosphere. As the rate that the lithsphere sinks into the asthenosphere is comparable to the rate at which it would sink into a fluid with the viscosity of the asthenosphere, Richter (1977) inferred a small force exerted by the slab on the rest of the plate. Richter and McKenzie (1978) suggested that the downgoing slab exerts a maximum stress of only 100 bar on the remaining surficial lithosphere. For a plate 100 km thick, this leads to a force per unit length of 10^{15} dyne/cm. Like the others, this estimate is surely uncertain by a factor of two of more.

Thus, the force per unit length can be very different depending upon the assumptions made and can be summarized as follows:

- $F = 1.0 \times 10^{17}$ dyne/cm: little direct force applied by the sinking slab to the surface plate
- $F = 1.8 \times 10^{16}$ dyne/cm: pull from a slab to a depth of 350 km
- $F = 3.2 \times 10^{16}$ dyne/cm: pull from a slab to a depth of 700 km
- $F = 5.1 \times 10^{16}$ dyne/cm: pull from a slab to a depth of 700 km with excess mass in an elevated olivine-spinel phase change

The variation in the values underscores our uncertainty in the processes occurring.

LENGTH OF CONTINENTAL CRUST SUBDUCTED

The pull of the slab is counteracted by the buoyancy of the light continental crust. This force per unit length is (ρ_m

$- \rho_c) g h_c d$, where d is the length of the continental crust that is subducted (Fig. 2). The mantle part of the continental lithosphere will contribute to the subduction by pulling down a fraction of the crust, h_s. The heavy oceanic slab is therefore resisted by $(\rho_m - \rho_c) g (h_c - h_s) d$. Subduction of continental lithosphere should cease when the force pulling it down is balanced by buoyancy of the continental crust. We seek a value of

$$d = \frac{F}{(\rho_m - \rho_c) g (h_c - h_s)},$$

the length of the continent subducted. Using $(\rho_m - \rho_c) = 0.55$ g/cm³, $g = 10^3$ cm/s², and $(h_c - h_s) = 35 - 10 = 25$ km, we obtain for $F = 1.0 \times 10^{15}$ dyne/cm: $d = 7$ km; $F = 1.8 \times 10^{16}$ dyne/cm: $d = 131$ km; $F = 3.2 \times 10^{16}$ dyne/cm: $d = 237$ km; and $F = 5.1 \times 10^{16}$ dyne/cm: $d = 298$ km. Note that an error of 0.1 g/cm³ in $(\rho_m - \rho_c)$ contributes a 19% error in the length of the crust subducted. Recall also that the uncertainty in h_s calculated in the previous section would nearly allow steady-state subduction of continental lithosphere. If $h_s = 20$ km instead of 10 km, the amount of crust to be subducted would be about 40% greater than that calculated above. As in the previous calculation, the 33% uncertainty of α in the parameters listed above leads to another 33% uncertainty in d. Each of these estimates for the amount of continental crust subducted is therefore uncertain by at least a factor of two, but notice that the uncertainty due to our ignorance of the processes involved leads to a much larger uncertainty in d.

These calculations are all based on the implicit assumption that the continent meets the subduction zone flush and that throughout the length of the subduction zone there is continental material. Such a situation is highly unlikely, for surely peninsulas will meet the subduction zone first. Moreover, continental fragments need not have the same width as the length of the subduction zone. The buoyancy of a long peninsula or of a small continental fragment, such as the Seychelles Islands, is surely negligible compared with the negative buoyance of the oceanic lithosphere, subduction of them ought to be complete. In the case of a continent half as long as the subduction zone, the amount of continent that could be subducted should be twice the values given above.

We think that except for such cases, however, only very short lengths ($d \sim 50$ km) of *intact* continental crust can be subducted. The gravity anomalies across island arcs (Kogan, 1975; Watts and Talwani, 1975) do not show evidence for the excess mass of the elevated olivine-spinel phase change. Because the fault-plane solutions of earthquakes below 350 km imply a resistance to the sinking of the slab, this lower part probably does not exert a pull on upper parts. Therefore, the shortest length (131 km) seems the most plausible of the three largest values given above.

Beyond this, the evidence that large events beneath the trenches seem to rupture through the entire lithosphere (Abe, 1972; Kanamori, 1971; Stewart, 1978) and the theoretical arguments of Richter (1977) and Richter and McKenzie (1978) suggest that only a small fraction of the negative buoyancy of the sinking slab is transferred directly to the surface. Moreover, the outer topographic rises seaward of deep-sea trenches do not seem to require large forces or moments that would be applied by the weight of the downgoing slab. Using laboratory data to constrain the strength of the lithosphere, C. Goetze and B. Evans (in prep.) have concluded that a bending moment per unit length of about 10^{25} dyne could cause a flexure of the lithosphere and thereby account for the observed topography. If this moment were caused by the negative buoyancy force per unit length of the downgoing slab, applied 100 km landward of the trench axis, a force per unit length of 10^{15} dyne/cm would be adequate. A much larger force could deflect the oceanic lithosphere much more than is observed. If this logic is correct, then only a short length of intact continental crust would be subducted.

Subduction of a short length of intact crust is not necessarily incompatible with the large crustal shortening observed in orogenic belts. The geologic evidence implies detachment of the upper and lower crust along shallow-dipping thrust faults. If the upper crust can be detached, the negative buoyancy of the mantle part of continental lithosphere is likely to be large enough to sustain subduction of it and the lower crust. Moreover, if the crust has a low melting temperature, it might melt before penetrating deep into the asthenosphere and thereby further reduce the resistance to subduction.

A DIGRESSION ON PRECAMBRIAN BLUESCHISTS

Blueschists are most common in Mesozoic and Cenozoic terranes; there seem to be no Precambrian examples (de Roever, 1956; Ernst, 1972). Greater heat generation and higher geothermal gradients in Precambrian time are thought to have prevented the high-pressure–low-temperature stability field for blueschists at that time (de Roever, 1956; Ernst, 1972). Another possibility is that Precambrian lithosphere was too thin and too buoyant to be able to pull cold crustal material down to the depths required for formation of blueschists.

SUMMARY AND CONCLUSIONS

Two factors contribute to subduction of continental lithosphere: the negative buoyancy of the mantle part of the lithosphere and the force exerted on the surface lithosphere by a downgoing slab of oceanic lithosphere. If there were a mechanism for detaching the upper crust from the lithosphere, the negative buoyancy of the mantle part would make it and the lower crust gravitationally unstable. The mantle lithosphere could subduct about 10 km of crust with it, but this estimate of 10 km is very uncertain and could be nearly three times larger if the values of the requisite parameters conspired. Gravity acting on the excess mass of a downgoing slab of lithosphere exerts a downward force on the surficial lithosphere. This force should be able to pull some continental lithosphere into the asthenosphere. If the crust remains intact, peninsulas and microcontinents might be subducted completely. The greatest uncertainty in the calculation of this force arises not in estimating the excess mass but in deciding how much of its gravitational body force is transmitted to the surface. If all of the force were transmitted, then hundreds of kilometres of continent could be subducted, as noted also by Bird and others (1975). If only a small fraction were transmitted, then only a negligible length of intact continental crust could be subducted. Although we think that the latter is the case, at present we cannot demonstrate it conclusively. If a substantial amount of continental crust can be subducted, this clearly will cause pronounced chemical heterogeneity of the mantle and will profoundly affect the crustal evolution of subduction zones such as in Tibet.

APPENDIX I. GRAVITATIONAL BODY FORCE ACTING ON THE DOWNGOING SLAB

If the oceanic lithosphere has an approximately linear temperature gradient ($\frac{\partial T}{\partial z} = -\frac{T_o}{a}$, where T_o = temperature in the asthenosphere and a = thickness of the lithosphere), then the temperature difference between the downgoing slab and the surrounding asthenosphere is given by (McKenzie, 1969)

$$\Delta T(x, z) = 2T_o \sum_{n=1}^{\infty} \frac{(-1)^{n+1}}{n\pi} \exp\left[\left(R - \sqrt{R^2 + n^2\pi^2}\right)\frac{x}{a}\right] \sin n\pi \frac{z}{a}, \quad \text{(A1)}$$

where x and z define an orthogonal coordinate system with x the distance downdip along the slab, z the distance into the slab measured from its base, and $R = \frac{\rho C_p v a}{2k}$, where ρ = density, C_p = heat capacity, v = rate of subduction, and k = thermal conductivity. $T(x, z)$ does not include adiabatic heating, but we use only the difference between the temperatures in the slab and in the asthenosphere, for which the adiabatic effect can be neglected (McKenzie, 1970). Thus, material in the slab is heavier than that in the asthenosphere by

$$\Delta\rho = \rho\alpha\Delta T = 2\rho\alpha T_o \sum_{n=1}^{\infty} \frac{(-1)^{n+1}}{n\pi} \exp\left[\left(R - \sqrt{R^2 + n^2\pi^2}\right)\frac{x}{a}\right] \sin n\pi \frac{z}{a}. \quad \text{(A2)}$$

The force per unit length along the arc due to the excess mass of the slab is

$$F = \sin\phi \int_0^a dz \int_0^{x_o} \Delta\rho\, g\, dx, \quad \text{(A3)}$$

where ϕ is the dip of the slab and x_o is the length along the slab of interest. Integrating equation A3 with A2, we get

$$F = \frac{4g\alpha\rho T_o a^2 \sin\phi}{\pi^3} \sum_{l=0}^{\infty} \frac{1 - \exp\left[\left(R - \sqrt{R^2 + (2l+1)^2\pi^2}\right)\frac{x_o}{a}\right]}{(2l+1)^2\left(\sqrt{R^2 + (2l+1)^2\pi^2} - R\right)}. \quad \text{(A4)}$$

Using the values $\rho = 3.35$ g cm^{-3}, $C_p = 0.28$ cal °C^{-1} g^{-1}, $v = 10$ cm yr^{-1}, $k = 7.5 \times 10^{-3}$ cal cm^{-1} s^{-1} °C^{-1}, and $a = 100$ km, we obtain $R \cong 200$. Because $R \gg \pi$ and only the terms with $l \lesssim 5$ turn out to be important, we may use

$$\sqrt{R^2 + (2l+1)^2\pi^2} - R \cong \frac{(2l+1)^2\pi^2}{2R}.$$

Then equation A4 becomes

$$F = 8g\alpha\rho T_o a^2 R \sin\phi \sum_{l=0}^{\infty} \frac{1 - \exp\left[\frac{-(2l+1)^2\pi^2 x_o}{2Ra}\right]}{(2l+1)^4\pi^4}.$$

As

$$\sum_{l=0}^{\infty} \frac{1}{(2l+1)^4} = \frac{\pi^4}{4!},$$

we have

$$F = \frac{g\alpha\rho T_o a^2 R \sin\phi}{12}\left(1 - 96 \sum_{l=0}^{m} \frac{\exp\left[-\frac{(2l+1)^2\pi^2 x_o}{2Ra}\right]}{(2l+1)^4\pi^4}\right). \quad \text{(A5)}$$

This derivation was given by McKenzie (1969), but he let $x_o = \infty$, so that the sum in equation A5 vanishes. The number, m, of terms used in sum depends upon the depth of penetration of the slab, but for $x_o > a$, fewer than five terms are adequate, and for $x_o \geq 5a$, only the first term is important. For $x_o = 5a$ or $10a$, the factor in parentheses is 0.13 or 0.23, respectively. With $g = 10^3$ cm/s^2, $T_o = 1,200$ °C, $a = 100$ km, and $\phi = 45°$, $F = 1.8 \times 10^{16}$ dyne cm and 3.2×10^{16} dyne/cm for these cases.

REFERENCES CITED

Abe, K., 1973, Lithospheric normal faulting beneath the Aleutian Trench: Physics of the Earth and Planetary Interiors, v. 8, p. 190–198.

Bird, P., Toksoz, M. N., and Sleep, N. H., 1975, Thermal and mechanical models of continent-continent convergent zones: Journal of Geophysical Research, v. 80, p. 4405–4416.

de Roever, W. P., 1956, Some differences between post-Paleozoic and older regional metamorphism: Geologie en Mijnbouw (new ser.), v. 18e, p. 123–127.

Ernst, W. G., 1972, Occurrence and mineralogic evolution of blueschist belts with time: American Journal of Science, v. 272, p. 657–668.

Fitch, T. J., 1977, *In situ* P-wave velocities in deep earthquake zones of the SW Pacific: Evidence for a phase boundary between the upper and lower mantle, *in* Talwani, M., and Pitman, W. C., III, eds., Island arcs, deep sea trenches and back-arc basins: Washington, D.C., American Geophysical Union, p. 133–136.

Gansser, A., 1966, The Indian Ocean and the Himalayas: A geologic interpretation: Ecologae Geologicae Helvetiae, v. 59, p. 831–848.

Gee, D. G., 1975, A tectonic model for the central part of the Scandinavian Caledonides: American Journal of Science, v. 275-A, p. 468–515.

Isacks, B., and Molnar, P., 1969, Mantle earthquake mechanisms and the sinking of the lithosphere: Nature, v. 223, p. 1121–1124.

———1971, Distribution of stresses in the descending lithosphere from a global survey of focal mechanism solutions of mantle earthquakes: Reviews of Geophysics, v. 9, p. 103–174.

Isacks, B. L., Oliver, J., and Sykes, L. R., 1968, Seismology and the new global tectonics: Journal of Geophysical Research, v. 73, p. 5855–5900.

Kanamori, H., 1971, Seismological evidence for a lithospheric normal faulting—The Sanriku earthquake of 1933: Physics of the Earth and Planetary Interiors, v. 4, p. 289–300.

Kogan, M. G., 1975, Gravity field of the Kuril-Kamchatka arc and its relation to the thermal regime of the lithosphere: Journal of Geophysical Research, v. 80, p. 1381–1390.

McKenzie, D. P., 1969, Speculations on the consequences and causes of plate motion: Royal Astronomical Society Geophysical Journal, v. 18, p. 1–18.

———1970, Temperature and potential temperature beneath island arcs: Tectonophysics, v. 10, p. 357–366.

Minear, J. W., and Toksoz, M. N., 1970, Thermal regime of a downgoing slab and new global tectonics: Journal of Geophysical Research, v. 75, p. 1397–1419.

Parsons, B., and McKenzie, D., 1978, Mantle convection and the thermal structure of the plates: Journal of Geophysical Research, v. 83, p. 4485–4496.

Powell, C. M., and Conaghan, P. J., 1973, Plate tectonics and the Himalayas: Earth and Planetary Science Letters, v. 20, p. 1–20.

Richter, F. M., 1973, Finite amplitude convection through a phase boundary: Royal Astronomical Society Geophysical Journal, v. 35, p. 265–276.

———1977, On the driving mechanism of plate tectonics: Tectonophysics, v. 35, p. 61–88.

Richter, F. M., and McKenzie, D. P., 1978, Simple plate models of mantle convection: Journal of Geophysical Research (in press).

Schubert, G., Yuen, D. A., and Turcotte, D. L., 1975, Role of phase transition in a dynamic mantle: Royal Astronomical Society Geophysical Journal, v. 42, p. 705–735.

Stewart, G. S., 1978, Implication for plate tectonics of the Aug. 19, 1977 Indonesian decoupling normal fault earthquake: EOS (American Geophysical Union Transactions), v. 59, p. 326.

Sung, C. M., and Burns, R. G., 1976a, Kinetics of high-pressure phase transformations: Implications to the evolution of the olivine-spinel transition in the downgoing slab of lithosphere and its consequences on the dynamics of the mantle: Tectonophysics, v. 31, p. 1–32.

———1976b, Kinetics of the olivine-spinel transition: Implication to deep focus earthquake genesis: Earth and Planetary Science Letters, v. 32, p. 165–170.

Toksoz, M. N., Sleep, N. H., and Smith, A. T., 1973, Evolution of the downgoing lithosphere and mechanisms of deep focus earthquakes: Royal Astronomical Society Geophysical Journal, v. 35, p. 285–310.

Watts, A. B., and Talwani, M., 1975, Gravity effect of downgoing lithospheric slabs beneath island arcs: Geological Society of America Bulletin, v. 86, p. 1–4.

ACKNOWLEDGMENTS

Reviewed by B. C. Burchfiel and F. M. Richter. Supported by National Science Foundation Grant 77-23017EAR and by National Aeronautics and Space Administration Grant NSG5260.

MANUSCRIPT RECEIVED AUGUST 14, 1978

MANUSCRIPT ACCEPTED OCTOBER 31, 1978

23

SOME CONSTRAINTS ON THE SHEAR WAVE VELOCITY STRUCTURE UNDER THE TIBETAN PLATEAU

W.P. Chen
P. Molnar (both at: Department of Earth and Planetary Sciences
Massachusetts Institute of Technology, Cambridge, Mass. 02139.

We have combined the observations of surface wave dispersion across the Tibetan plateau and the differential travel time residuals between P and S waves for earthquakes in Tibet to place bounds on the possible shear wave velocity structure beneath Tibet. The P wave velocity structure is relatively unconstrained and was assumed to be the same as Dziewonski's velocity model S2 for the shield regions except for the inclusion of a possibly thick crust. Surface wave dispersion data suggest a range of possible crustal thickness from 55 km to 70 km or even 85 km with upper mantle shear wave velocities of 4.4 km/sec, 4.7 km/sec, and 4.8 km/sec respectively. The travel time residuals indicate the shear wave velocity beneath Tibet is, on the average, 5 to 6% less than that beneath shields, assuming that all the differences in velocity structure between Tibet and shields were confined to the upper 240 km. If the shield model S2 is adjusted to have the same crustal thickness as the Tibetan models, the Tibetan models will have average shear wave velocities 4 to 5% less than that of S2 in the depth range of 100 km to 240 km. This corresponds to an average shear wave velocity of about 4.3 km/sec in this depth range, and might be an indication of elevated termperature. If

a strong low-Q structure exists under Tibet, then because of velocity dispersion, the average velocities should be even lower.

(Presented at the Fall Annual Meetings of the American Geophysical Union, December, 1978.)

SUBDUCTION INDUCED CONVECTION AND ISLAND-ARC CONVECTION

Albert T. Hsui
M. Nafi Toksöz (both at: Department of Earth and Planetary Sciences, Massachusetts Institute of Technology, Cambridge, MA 02139
Bruce D. Marsh (Dpeartment of Earth and Planetary Sciences, Johns Hopkins University, Baltimore, MD 21218)

Subduction of lithospheric slabs induces convection in the overlying asthenosphere. This convection strongly influences the thermal regime of the subduction region, and has implications to the formation of back-arc basins and island-arc volcanism. In this study, we carry out a detailed calculation on the thermal structure of the wedge area between the subducting slab and the overlying lithosphere, utilizing a finite difference numerical technique. Results indicate that the area above the descending lithosphere will generally be of higher temperatures if a low viscosity asthenosphere exists. This is mainly because the low viscosity asthenosphere will deform in response to the shear stresses applied at the boundary by the descending lithosphere. As a result, and induced convective current is established above the slab. This current will steadily feed the wedge corner with warmer material from the deeper interior. The 'cooling effect' of the cold slab can only penetrate to a certain skin depth which is related to the subduction speed. One the other hand, at the absence of convection, the wedge area will continuously be cooled by the descending lithosphere. Therefore, from

the thermal point of view alone, it is apparent that island arc volcanism is more likely to take place if there exists, above the subducting lithosphere, a low viscosity region where convective currents can be induced. This is consistent with the conclusions derived from seismic observations.

(Presented at the Fall Annual Meetings of the American Geophysical Union, December, 1978.)